"*Whether you think you can or think you can't—you're right*." **Henry Ford**

Rapid Screening and Optimization of Adsorbents by Combining Molecular Simulation With Rapid Experimental Methods

by

Masoud Haeri Nejad

MSc in Chemical Engineering, KTH, Royal Institute of Technology, Stockholm, Sweden 2012

A Dissertation Submitted in Partial Fulfillment
of the Requirements for the Degree of

Doctor of Philosophy

in the Graduate Academic Unit of Chemical Engineering

Supervisor: Mladen Eić, Ph.D., Chemical Engineering

Examining Board: Brian Lowry, Ph.D., Chemical Engineering
Huining Xiao, Ph.D., Chemical Engineering
Barry Blight, Ph.D., Chemistry

External Examiner: Robert Marriott, Ph.D., Chemistry, University of Calgary

This dissertation is accepted by the
Dean of Graduate Studies

THE UNIVERSITY OF NEW BRUNSWICK

October 2024

ABSTRACT

Adsorption has proved to be an efficient means for removal of pollutants from the atmosphere. In addition to traditional adsorbents, such as silica gel, activated carbon and zeolites, new adsorbents have been introduced which include the metal-organic frameworks (MOF's). The number of MOF structures is enormous and therefore ranking them for any specific application requires time-saving approaches.

In this work, a novel approach dubbed "rapid screening" was introduced. It consists of (1) molecular simulation for prediction of adsorption isotherms followed by (2) the rapid experimental technique of the zero-length-column chromatography (ZLC) for isotherm confirmation. This approach was applied to the example case of screening and modifying metal-organic frameworks (MOFs) adsorbents to remove wasted inhalation anesthetic agents (IAA).

IAA adsorption isotherms for three MOFs were predicted using molecular simulation (MS). For successful simulation of these large, branched, and polar adsorbates, an all-atom force field was also developed which accounted for the flexibility of the adsorbate IAA molecules. Using Continuous Fractional Component Monte Carlo (CFCMC) algorithms proved crucial to speed up the simulations. Predictions from MS results were subsequently verified by performing experimental adsorption measurements using traditional methods followed by the faster ZLC technique, with necessary modifications for vapors. ZLC was

shown to be able to replace the traditional volumetric or gravimetric adsorption methods with acceptable accuracy.

Next, the utility of rapid screening approach was verified for structural modification of a promising adsorbent for enhancing its IAA removal capability. Several structural modifications, including grafting, anion exchange and functionalization of benzene rings were proposed to the alter the pristine structure. New procedures were developed to create of new crystal information files(CIFs) for the modified structures to replace the CIF for the pristine structure as input to molecular simulations. The MS- predicted a two-fold of IAA adsorption capacity for MIL-101-Cr@NH_3 ($X=F^-$, OH^-) compared with the unmodified structure. Experimental syntheses and rapid ZLC measurements confirmed this prediction.

This approach, presented as proof of concept, is applicable to a larger number of materials by procuring or performing syntheses only of those structures that molecular-simulation screening has selected as the most promising adsorbent.

DEDICATION

This dissertation is dedicated to my parents, my brother, and my sister.

ACKNOWLEDGEMENTS

My sincere thanks go to my supervisor Professor Dr. Mladen Eić for his support, dedication, and insight and for entrusting me with conducting this research. I am very grateful and privileged to have been able to work under his supervision.

I would also like to thank the support and help of the following people: Dr. Xue 'Snowy' Han for helping me with my early ZLC experimental setup. Dr. Kyle Rogers for his useful advice regarding the maintenance of mass spectrometry instrumentation. Carl Murdock for procurement of the pieces of equipment and spare parts which we needed for successful completion of the experimental section. Sandra Riley for her regular inspection of our laboratories, for her thoughtful advice on safety matters and her later role as store manager with the procurement of supplies and sending the faulty equipment for repair and with helping me to organize the laboratory. Adon Briggs for building a setup of ZLC experiment, Jason Gorham for maintenance and repair of our vacuum pumps at Chemical Engineering Workshop, Michael Morton, Bruce Miller and Dayton Coburn at electrical engineering workshop and Mr. Vince Boardman at Mechanical Engineering Workshop for helping with troubleshooting and maintenance our equipment. Martin Hann at ITS hardware for computer hardware support. Dr. Daniel Hagmeyer, Dr. Garret Taggart, Dr. Serkan Göpinkar and Dr. Joji Sonoda from Belsorp, Katie Mackie and Calvin Debique and Luke Wilkinson from Hiden Isochema, Anna Medekova from Ametek and Janie Du from Stanford Research Systems for helping me with tuning, maintenance and troubleshooting our volumetric, gravimetric adsorption systems as well as the mass spectrometers. Karen Annett and Sylvia Demerson are highly appreciated for helping with administrative issues

and computer maintenance and troubleshooting. Matt Hannaberg, Vincent Marioniti and Darren Johnston from Scion Instruments are thanked for help with maintenance of TCD FID detectors on our gas chromatograph. I appreciate the effort and support of my diligent research assistants, Kalian Hiew, MScChemEng and Menghan “Monica” Liu, BScChemEng. Finally, I would like to extend my sincerest gratitude to my parents and siblings for their selfless, unconditional, and incessant support throughout my entire life.

Table of Contents

List of Tables

List of Figures

List of Abbreviations

AC: Activated Carbon

BET: Brauner-Emmett-Teller

CIF: Crystal Information File

CMS: Carbon Molecular Sieve

CUS: Coordinatively Unsaturated Site

DF: Desflurane

DRIFT-IR: Diffuse-Reflectance Fourier-Transform Infra-Red Spectroscopy

DSC: Differential Scanning Calorimetry

FF: Force-field

FID: Flame-Ionization Detector

GC: Gas Chromatograph

GCMC: Grand-Canonical Monte-Carlo

GWP: Global-Warming Potential

IAA: Inhalation Anesthetic Agent

LJ: Lennard-Jones

MD: Molecular Dynamics

MOF: Metal-Organic Framework

MS: Mass Spectrometer

PSD: Pore-Size Distribution

PXRD: Powder X-Ray Diffractometry

RGA: Residual Gas Analyzer

SEM: Scanning Electron Microscope

SF: Sevoflurane

SVP: Saturation Vapor Pressure

TCD: Thermal Conductivity Detector

TGA: Thermogravimetric Analyzer

VLE: Vapor-Liquid Equilibria

VLCC: Vapor-Liquid Coexistence Curve

ZLC: Zero-Length Column Chromatography

Chapter 1. Introduction

1.1. Background

Adsorption has been well-established as an energy-efficient method for removal and recovery of atmospheric pollutants. It is also used for separation of gas mixtures. In this role, the separation competes with gas membrane technology[1]. For instance, this technique can be used to remove Inhalation Anesthetic Agents (IAA's), which can be present in the operating room of hospitals either through leaks from the vaporizer systems that are used for administering IAA's or from the exhalation of patients. As only about 5% of anesthetics are used by patients most of it is exhausted through hospitals' exhaust vents. The most decisive factor in the design of an efficient adsorption setup is the choice of the adsorbent material. A promising material is expected to have high uptake (adsorption) capacity towards the target species to be removed and high selectivity against the rest of the gas mixture components.

Several studies have been published suggesting promising adsorbent materials for IAA removal including activated carbons [2][3], zeolites [1][3]–[5][10], metal-organic frameworks (MOFs) [7]–[9], and aerogels [3]. It should be noted that very little attention has been paid so far to the use of MOFs as potential adsorbent materials for the removal of IAA. This is, despite the fact that MOFs promise much higher utility than other adsorbent materials due to their much higher specific surface area and their diversity in pore-sizes and functional groups, which can be achieved by using a variety of inorganic and organic

precursors. Both direct synthesis and post-synthetic modification (functionalization) have been tried[10].

More than 280,000 MOF structures have been synthesized or hypothetically predicted up to this point of time [11][12]. Considering the prospects of their structural modification, the number of possible MOFs is virtually unlimited. This statistic already signals the challenging task of picking the most suitable MOF adsorbent material for any given separation application (including the case studied in this thesis for IAA removal from hospital vent gases). Certainly, synthesizing so many structures and running characterization tests cannot be an option. This brings us to the question of whether it is possible to model both the IAA adsorbates and the MOF adsorbents theoretically and to run simulations to predict their adsorption properties, e.g., isotherms. And then use a rapid screening technique to experimentally measure the adsorption isotherms only for the most promising candidates.

Although molecular modeling and simulation based on computational chemistry have been around for quite some time now [13], historically, they were not widely used for adsorption modeling. Some plausible reasons are related to the need to develop transferable force fields, which has not been developed until recently. Another challenge is attributed to the lack of crystallinity in some traditional adsorbents, such as activated carbon, which consequently did not lend themselves readily to molecular simulations [14]. Even for the crystalline zeolites, molecular simulations were not so attractive due to the limited diversity

of their structures. But then, there are the MOFs. The high crystallinity and vast structural diversity of MOFs led to a surge in interest in molecular modeling of adsorption[15].

The advantage of molecular simulation algorithms such as Monte Carlo (MC) and Molecular Dynamics (MD) is that they can predict physical properties of a given structure before performing experimental characterization[13]. They can be accurate enough to predict a molecule's properties in the absence of experimental data[16]. Furthermore, they can help propose structural modifications before synthesizing the modified structure first. As an example, recent CO_2 adsorption studies on MIL-100-Fe and MIL-100-Cr [17] using Grand Canonical Monte Carlo (GCMC) method helped elucidate the contribution of different types of atoms in the structures, the heat of adsorption and a better understanding of CO_2 adsorption mechanism. Molecular simulation can also make valid predictions of the physical properties of the adsorbate molecules, such as their vapor-liquid coexistence curves (VLCC)[16].

For the case of IAA adsorption, our literature review revealed no published articles on using molecular simulation to predict the physical properties of IAA, such as their critical properties and mass densities. Furthermore, no simulated adsorption isotherms were reported and even experimental data for physical properties of IAA are scarce [4].

1.2. Thesis Objectives

The purpose of this project is to model IAA molecules sevoflurane and desflurane and simulate their adsorption isotherms on selected candidate MOFs using the Grand-Canonical Monte Carlo. The MOFs were tested using common characterization techniques

such as Nitrogen 77K physisorption, XRD, TGA/DSC, FTIR, and SEM. The adsorption isotherms of sevoflurane and desflurane were also experimentally measured at different temperatures, first using the conventional volumetric/manometric technique to validate accuracy of simulation results as well as the novel zero-length-column chromatography (ZLC) method as a proposed rapid-screening experimental technique.

Once the agreement between the simulation and experiment is validated and an adsorption mechanism is suggested, the most promising MOF candidate were selected before proceeding to the modification stage. Several modifications to selected pristine structure were suggested followed by simulating their corresponding adsorption isotherms. Moreover, physical samples of modified MOFs were also prepared and characterized. Based on the results from molecular simulation and experiment, we made a ranking of the new structures and select the modified MOF with superior performance than the pristine material. By assessing this 'rapid-screening' approach, it is expected that in practice only the most favorable modifications predicted by simulation would be synthesized and then their experimental adsorption isotherms measured using the fast ZLC technique.

1.3. Thesis Layout

In Chapter 2, the background information about theory and practice of adsorption, some classes of adsorbents and the different techniques for textural characterization of adsorbents is presented. In Chapter 3, MOFs are discussed including their synthesis, post-modification, and stability. Chapter 4 briefly discusses the inhalation anesthetic agents and their administration methods in hospitals. Chapter 5 presents the basics of molecular simulation with focus on the procedure introduced in this work for the simulation of

adsorption isotherm of IAA. Chapter 6, which has been already published as a peer-reviewed research paper[18], covers the first part of this thesis and consists of a combined experimental and simulated approach which is treating the adsorption isotherms of sevoflurane and desflurane on three selected MOF structures. It also formulates the selection of the most promising adsorbent material out of the three MOFs. In Chapter 7, post-synthetic modification of MOFs is presented. Chapter 8, which is also submitted for publication, uses the findings reported in Chapters 6 and 7, assess the effect of four modifications on adsorption capacity of the original MOF (MIL-101-Cr) by using molecular simulation. This chapter also ranks the new adsorbents and presents a superior adsorbent material derived from the pristine structure. Chapter 9 reviews and compares traditional isotherm techniques with ZLC. ZLC is further discussed in greater details in Chapter 9 as a fast experimental technique for measurement of adsorption isotherms of the original samples and their enhanced modification(s). Example cases of permanent gases of carbon dioxide, methane, and ethylene on LTA type zeolites 4A and 5A and FAU type zeolite 13X are presented. This is followed by isotherms of sevoflurane and desflurane on MOF structures treated in the same chapter. Chapter 10 summarizes the results from Chapters 6 to 9 before providing recommendations for future work on the topic.

Chapter 2. Adsorption, adsorbent materials, characterization techniques

In this chapter, some of the most common classes of adsorbents for gas storage and separation are reviewed, followed by common techniques for the texture characterization of adsorbents.

2.1. Gas adsorption

Solids are intrinsically amenable to adsorb ambient gases. This phenomenon is mostly attributed to the thermodynamic instability of the surface of the solid. The potential energy function describing the interaction between the gaseous sorbate and the solid sorbent can be summarized by Equation 2.1[19].

$$\phi_{\text{adsorbate}-\text{adsobent}} = \phi_D + \phi_R + \phi_{Ind} + \phi_{F\mu} + \phi_{\dot{F}\mu} \qquad (2.1)$$

Where the five terms on the RHS of the equation represent dispersion(ϕ_D), repulsion(ϕ_R), field *vs* induced dipole(ϕ_{Ind}), field *vs* point dipole$\left(\phi_{F\mu}\right)$ and gradient of field *vs* quadrupole$\left(\phi_{\dot{F}\mu}\right)$ interaction potentials, respectively.

Unlike the first two terms $\phi_D + \phi_R$ that are common to all adsorption processes and are often referred to Van der Waals type interaction, the remaining terms appear when electrostatic interactions between polar surfaces and/or polar gases exist. In fact, the electrostatic forces can become the dominant contributors for the latter case. The

importance of these contributions when introducing different types of adsorbents will be discussed in the proceeding sections.

2.2. Adsorbents

Three of the most frequently used porous solid materials for gas and vapor adsorption include zeolites, activated carbon, and carbon molecular sieves (CMS). Most recently, metal-organic frameworks (MOFs) have been introduced. This dissertation mainly deals with results for adsorption of IAA vapors on MOFs but some data for the adsorption of smaller permanent gases on zeolites will also be presented in a later chapter.

2.2.1. Zeolites

Zeolites are very useful adsorbents which are basically made up of alkali- or alkali-earth-aluminosilicates[20]. They are grouped into several framework types. Each type of framework can be described as a combination of smaller substructures known as secondary building units (SBU)[21]. The SBUs are in turn composed of TO_4 (T = Si, Al) tetrahedra interconnected through 3D channels and 2D windows made up of rings formed by oxygen atoms. Zeolites are intrinsically microporous but it is possible to make them into hierarchical porous structures by introducing templates during synthesis[22]. It is common to replace some of the Si atoms within the structure with Al atoms. As the valence of Al is lower (+3) than Si (+4), this substitution makes the overall charge of the new structure negative. This negative charge is neutralized by extra-framework cations involved in the synthesis reaction or introduced by means of ion-exchange. Examples of these cations are Ca^{++}, Na^{+}, and K^{+}. The different sizes of these ions affect the pore size of the zeolite which

functions as a molecular sieve. Also, because of the presence of Al as a Lewis base site the Si/Al ratio is usually reported.

Databases of zeolite structures have been compiled where each structure type is identified by a three letter code[23]. Some of the well-known zeolite types used for gas adsorption includes the LTA (Linde types 3A, 4A, and 5A), FAU (Linde types 10X and 13X) and MFI (ZMS-25). As of 2024, 253 types of zeolite structures have been identified**.** Some examples of zeolite structures are included in Figure 2.1S in Appendix A[24]. Tables 2.1S, 2.2S, and 2.3S in Appendix A compare these two types of zeolites in terms of their structural specifications and cation distribution [20].

Zeolites are generally hydrophilic, with the exception of silica-rich zeolites such as silicalite and MFI type of zeolites, which are hydrophobic structures, and as such are considered good adsorbents for hydrophobic molecules, such as hydrocarbons [23]. Nevertheless, due to the presence of cations in zeolites, primarily in hydrophilic ones, such as LTA, faujasite and mordenites, the electrostatic interactions become more important for polar adsorbates. Cations in zeolites are loosely connected to the anionic surface of the zeolite, and as a result, interactions due to permanent dipoles and/or quadrupoles become the major contributor to adsorption of polar adsorbates on zeolites.

One can, completely or partially, replace the cations in the zeolite by using ion exchange techniques. As different cations possess different ionic charges and radii, their preference

to position on different types of sites available inside the zeolite framework varies. See Tables 2.1S, 2.2S, and 2.3S in Appendix A**.**

2.2.2. Activated Carbons and Carbon Molecular Sieves

Charcoal can be activated if it is treated with acids, strong bases, or salts. Activated carbons have surface functional groups mainly composed of oxygen. They have much higher specific surfaces areas (500-3,000 m^2/g) compared to the parent charcoal (0.2-5 m^2/g) [25]. Methane and hydrogen storage, air purification and water purification are among the applications of activated carbons. [26]**.** They are produced in various shapes including powder, granular, extruded and bead forms[27].

Synthesis of activated usually comprises of three steps, raw material treatment, carbonization, and activation. The conditions of the steps are summarized in Table 2.4S in Appendix A.

Adsorption properties of activated carbon are unique in three ways: Firstly, it does not need strict moisture removal during regeneration. Secondly, it has large accessible internal surface area and lastly, its heat of adsorption is relatively low because of the dominance of van der Waals interactions. This dominance explains lower energy requirement of activated carbon to be regenerated.

To make AC suitable for adsorption of polar gases, such as water vapor, oxidation of the surface can help at low p/p_0. For higher p/p_0, the pore volume is the determining factor.

Adsorption of water vapor on activated carbon involves attachment of the first water molecules on the adsorbent surface followed by cluster formation, pore-filling, and finally, capillary condensation inside the micropore.

Carbon molecular sieves (CMS) belong to the group of microporous materials characterized by high adsorption capacity and high selectivity towards gases[28]. The synthesis methods of these adsorbents are mostly patented, but it is thought to consist of coal or nutshells being oxidized before being shaped into granules by bindered pelletization, followed by carbonization and finally coating of hydrocarbon cracking products under inert atmosphere.

CMS possess pore sizes comparable to the effective diameter of small molecules. They are used for the separation of nitrogen from air and H_2/ He purification as an example. The pore mouths (and not the whole pore walls) are either enlarged or narrowed for H_2/ He purification and air separation applications, respectively.

2.2.3. Metal-organic frameworks

Metal-organic frameworks (MOFs) are novel materials that are a hybrid of inorganic and organic substances[29]. They can be used as sensors[18], catalysts[31], for drug delivery[32], for water harvesting[33], and as adsorbents[34]. The advantage of these adsorbents over zeolites and carbons, is their higher accessible specific surface areas, and tunable pore apertures[35]. Moreover, the functionality of the organic linker is adjustable. Many MOFs possess architectural flexibility and are thermally and physically stable[36].

Over 280,000 of such compounds have been either synthesized or hypothetically predicted[37][38]. Compared to zeolites where the metallic part is limited to silicon and aluminum, MOFs can be synthesized from many metallic elements in the Periodic Table[14]. The diversity of the organic part is even more remarkable for the MOFs. Whereas for zeolites it is limited to O^{2-} bridges, for MOFs one can choose organic linkers of various lengths with or without benzene rings. The benzene rings can in turn be functionalized, [39]. As their introduction, several paths for direct and post-synthetic modification of MOFs have been developed. These methods include hydrothermal, solvothermal, microwave and others[40]. More information on MOFs is presented in Chapter 3 of this thesis.

2.3. Physicochemical characterization of adsorbents

Important features of a solid adsorbent include its specific surface area, mean pore size, pore size distribution, total pore volume, degree of crystallinity, crystal size, functional groups on the surface, and its chemical composition. Tests like Brauner-Emmet-Teller isotherm modelling (BET) [41] are performed to obtain important textural data, such as specific surface area, pore size diameter and pore size distribution. Some of the most common characterization techniques for adsorbents are summarized in the following subsections.

2.3.1. BET test/Pore-Size-Distribution

BET tests are performed by measuring nitrogen adsorption isotherms at its saturation temperature of 77K. The cryo-temperature is provided and maintained by using a Dewar jar filled with liquid nitrogen. After pre-treatment of the sample which is a combination of

heating and high-vacuum degassing, nitrogen is introduced into the manifold. When the manifold reaches a pre-specified pressure, the main inlets and all the outlets are closed. Next, the inlet valve connecting the manifold to the sample holder is opened and kept in this position until the sample cell and manifold reach the same pressure. Following this quick step, the sample inlet is closed again and the pressure inside the closed sample cell is monitored until the pressure fluctuations become sufficiently low to meet a predefined equilibrium criterion. Now, the system moves to the next higher (during adsorption) or lower (during desorption) step value . After the adsorption and desorption scans are completed, BET plots are prepared to determine specific surface area, mean pore diameter and total pore volume. It is also possible to prepare pore-size distribution curves by fitting the isotherm data with a suitable model such as BJH, SF, HK, or DA. These models are based on microporosity or mesoporosity of the sample and therefore should be chosen as the case might be. An interesting feature of the nitrogen adsorption isotherm at 77K, known as hysteresis, occurs when the adsorption and desorption curves do not fully overlap [42]. Hysteresis provides valuable insight into adsorption mechanism and the porosity of the adsorbent. International Union of Pure and Applied Chemistry (IUPAC) [43] has published a classification of adsorbents into six types based on the shape of the nitrogen physisorption at 77K curve for the adsorbent, where the existence of hysteresis is a decisive factor.

2.3.2. TGA/DSC

Thermal gravimetric analyzer (TGA)[44][45] and differential scanning calorimetry (DSC)[46] are useful tools for characterizing adsorbent material. TGA allows us to estimate the amount of residual moisture inside the pores. It also provides information

about the strength of the bonds and overall thermal stability of the material before the structure totally collapses. Figure 2.2S in Appendix A shows the instrument used in our laboratory. It is equipped with two pans: one for the sample and the other for blank or another sample. The pans are connected to the arms of a microbalance which monitors the weight as well as a thermocouple that records the temperature. The DSC function of the instrument gives us the option to simultaneously assess the nature of weight change of the sample, due to either exothermal or endothermal process. The instrument allows different gases including helium, nitrogen, or oxygen to flow over the sample during heating or isothermal steps. If the outlet of the TGA is fed into the inlet of a mass spectrometer or an FT-IR instrument, one can get *in situ* information about the nature of the volatile components leaving the sample, too.

2.3.3. FTIR

Fourier-Transform Infrared Spectroscopy (FT-IR)[47] is a tool for characterization of adsorbents from their composition and especially the nature of functional groups on its surface. Figure 2.3S in Appendix A shows the instrument that is used in our laboratory. It is equipped with different types of sample holder for off-line or in-situ analysis of powder-shaped samples. In one configuration, the sample holder cells consist of a blank and a sample cell. The blank can be left empty or filled with finely ground KBr. The sample is a dilute solid mixture of KBr, and the sample blended and ground into a very fine powder. KBr is often preheated to remove residual moisture. The blank and the sample are exposed in series to the laser radiation and the reflected radiation is picked up by a detector connected to data analysis system. As a single scan is too noisy, we performed around 50

scans which are averaged into a smooth, noiseless spectrum. The sample spectrum is further corrected for background and smoothed.

2.3.4. XRD (Single Crystal / Powder)

X-ray diffraction (XRD) is an established and very useful technique that can be used to get a wealth of information about the adsorbent structure, including its degree of crystallinity, relative position of atoms within the structure, crystal size and lattice parameters [48]. XRD can be performed on single crystals or powder. The plot represents signal intensity in arbitrary units vs the angle of rotation of the goniometer consists of peaks. The plot provides information to allow distinction between intense sharp peaks indicating high degree of crystallinity vs low-intensity broad peaks that indicate amorphous phases. A shift in the peak position or appearance of a new peak or splitting peak is an indication of structural modification or coexistence of more than one crystal phase[49]. Although powder XRD results are more commonly reported, single-crystal data has proved to provide deeper insight especially in order to create the CIF files of the structure. For the latter, the crystals need to be large enough, e.g., usually in the micrometer range[50].

2.3.5. SEM/TEM

Scanning Electron Microscopy (SEM) and Transmittance Electron Microscopy (TEM) are powerful tools for physical characterization of adsorbents. They produce images of various resolution normally in the micrometer range. If equipped with Field Emission (FE) source, nanoparticles can also be discerned. Unlike SEM, which is based on reflection and scattering, TEM needs samples thin enough so that the electron rays can pass through. Both techniques are based on bombardment of the sample with electrons emitted from an

electron gun. For SEM the surface of the sample needs to be conductive. If not, it is coated with a layer of carbon first during sample preparation. If equipped with EDS detector chemical analysis and mapping of the sample surface is also possible during scanning. Figure 2.4S in Appendix C shows our SEM instrument used for some of the figures reported in this thesis.

Chapter 3. Metal-Organic Frameworks

Metal-organic frameworks ,also known as porous coordination polymers, are a relatively new type of porous structure[51][52] that have found application for adsorption applications such as gas storage[53], gas purification and bulk separation. They consist of inorganic metal clusters and organic hydrocarbon bridges aka linkers. The metal-clusters also referred to as nodes can adapt to various topologies[54]. The first successful synthesis of MOFs was performed by Yaghi in mid-1990's [55] once he realized that the metal nodes aka the secondary building units (SBU) need to consist of at least two metals[55]. Otherwise, the porous structure will collapse during activation (removal of the solvents inside the pores)[55].. Ever since, the structure has gained huge interest and thousands of MOFs have been synthesized in the lab[56] or designed hypothetically. Databases such as CSD and ARC-MOF[12] contain ready to use CIFs for these crystalline structures. The main reasons for popularity of MOFs are their tunability and ease of design in comparison to the less versatile zeolites and hard to model amorphous solids such as activated carbons. Some examples of common MOF structures are included in Section I of Appendix B.

3.1. Classification of MOFs

MOFs have been expanding rapidly ever since they were introduced in the 1990s. Several research groups have been involved in developing different classes of MOFs. This section examines classification of MOFs based on their component units[57] .

3.1.1. Isoreticular MOFs (IRMOF)

IRMOFS are microporous crystals with high porosity composed of octahedral $[Zn_4O]^{6+}$ clusters as inorganic secondary building units (SBUs) and organic carboxylic acids as organic ligand precursors.

They have been reported for adsorption of volatile organic compounds[58].

3.1.2. Porous Coordination Networks (PCN)

PCNs are products of coordination reactions between metal ions and porphyrin-like organic ligands. The matrix possesses Lewis acidity and it has a special topology of hole-cage-hole[57]. PCN-57, PCN-222, and PCN-250 are some of the more known examples of this family. They have been reported to be used for selective separation of alkanes from alkenes[59].

3.1.3. Zeolitic Imidazolate Frameworks (ZIF)

ZIFs are synthesized through coordination reaction of imidazole ligands of Zn(II) or Co(II) aluminosilicate networks. The resulting network has metal-imidazole-metal angles of 145° which is identical to the Si-O-Si angle in zeolites. ZIFs are therefore named after their zeolite-like topology. Over 100 ZIF structures have been reported as of 2010. Most ZIFs have high chemical and thermal stability. They have been used in CO_2 capture applications[60] and for gas separation adsorption[61], among other uses[62]. ZIFs have also been turned into glassy form which is an organic-inorganic type of glass next to the traditional inorganic, organic, and metal types[63].

3.1.4. Porous Coordination Polymers (PCP)

PCPs are synthesized through the reaction of transition metals with carboxylic acids or pyridines[64][65]. Their internal bonding types allow them to be transformed into various structures such as linear, T-shaped, plane triangular, tetra- and octahedron[66]. PCPs have been reported for successful natural gas purification applications[67].

3.1.5. University of Oslo MOFs (UiO MOF)

UiO MOFs were first synthesized through a reaction between a dicarboxylic acid and $Zr_6(\mu_3\text{-}O)(\mu_3\text{-}OH)$ metal cluster as UiO-66. It is composed of four octahedral cages (1.1 nm) and eight tetrahedral cages (0.89 nm) with triangular windows to help flow in and out of the cages[68]. UiO-66 has been reported to be used for adsorption of water[69], SiO_2[70] and toluene[71]. Other well-known members of this family of MOFs include UiO-67 and UiO-68[57]. They differ in cage size due to different choice of organic ligand for synthesis[72].

3.1.6. Coordination-Pillared Layer MOFs (CPL-MOF)

CPLs are 3D structures composed of 2D molecular layers formed as a reaction between Cu(II) and bipyridine family of ligands supported by other types of ligands such as …… serving as pillars[57]. The flexibility of the pillar molecules makes them amenable to rotation at elevated pressures and allowing for abrupt adsorption rates. CPL-n structures with n=1 to 7 have been synthesized. Most of them can be synthesized at room temperature[73].

3.1.7. Materials of Institute Lavoisier MOFs (MIL-MOF)

MIL-MOFs are one of the most popular class of MOFs due to their high thermal and chemical stability as well as high water resistance. These structures are formed by the reaction of transition metals Al, Fe, Cr, V and Ti with the dicarboxylic acid, terephthalic acid, or the tricarboxylic acid, trimesic acid. The resulting structure has a very high specific surface area and is composed of microporous and mesoporous cages[74]–[77]. Flexible structures such as MIL-53 have also been reported[78]. Two of the structures in this group MIL-100-Al and MIL-101-Cr were considered in this dissertation. See Chapters 6 and 8.One of the interesting aspects of these MOFs is the existence of unsaturated Lewis acid sites also known as coordinated unsaturated sites (CUS) . See section 3.2.1. for a discussion of CUS.

3.1.8. Other MOFs

There are examples of MOFs developed in other research groups. Some of them include DUT[79], HKUST[80] MOFs developed by Dresen University of Technology and Hong Kong University of Science and Technology, respectively.

3.2. Structural Characteristics of MOFs

MOFs possess unique characteristics that makes them distinct from other types of porous materials such as zeolites and carbons. The fact that they are made of SBUs with strong covalent bonds in combination with the use of directional organic ligands makes their final crystal very critical and, in that respect, it is critical in the directional design of the resulting topology of the MOF. Some of the most important structural characteristics of MOFs include (1) having highly-ordered pores, (2) diversity and tunability of the framework, and

(3) formation of coordination unsaturated sites (CUS). This last characteristic is discussed in some detail in the subsection below.

3.2.1. Coordination Unsaturated Sites (CUS)

CUS's are metal or metal-cluster sites that are not coordinated to an organic ligand during the synthesis of certain MOFs [80]. The reason could be short reaction times, a ligand mismatch or simply due to the metal charge. These uncoordinated sites have strong reactivity and as a result can function as powerful Lewis acid sites. For example, they can interact with water molecules, where an acidic M-OH_2 is developed. The presence of CUS and their utility is discussed further mentioned in Chapters 5 and 6 of this work.

3.3. Synthesis and characterization of MOFs

MOFs have been synthesized in a variety of methods[81]. Apart from the more traditional solvothermal, hydrothermal, room-temperature solvent/water based, diffusion, i*n-situ* linker and high-throughput synthesis methods[82], alternative methods such as microwave-assisted solvothermal[49][83], sonochemical[84], mechanochemical[85][86], electrochemical[87] and Continuous-flow[88] synthesis techniques have been reported in the literature. It is also important to keep in mind that like any other reaction, there are competing kinetically faster routes that can lead to creation of several phases to the intended structure phase. Therefore, choosing the optimum species of the metal precursor, ligand precursor, use of capping as well as modulators[89][90] is crucial. At the end, it is important to run relevant characterization tests to verify the success of the synthesis and it high yield. These characterization can include but not limited to BET tests, PSD (pore-size distribution), NMR analysis of the filtrate, FTIR, XRD, TGA/DSC, CHNS elemental

analysis, and SEM/TEM. Synthesis details of the MOFs discussed in this thesis are described in Section II of Appendix B.

3.3.1. Important factors influencing synthesis of MOFs

In addition to the choice of organic salts and organic ligands, other factors such as the pH, temperature and molar ratio of the reacting agents can decisively affect the final structure and the yield of the desired structure[91]. Some of these factors were encountered in the course of the preparation of the materials in this dissertation and have been described in the relevant sections.

3.4. Stability of MOFs

It is important for MOFs to be resistant to ambient air moisture, e.g., during storage or at the working conditions[92]. Factors affecting the stability of MOFs can be categorized into two classes, thermodynamic and dynamic. Thermodynamic stability of materials refers to the transition state or intermediate structure generated during the synthesis reactions. Examples of thermodynamic factors include bonding strength, pKa, and charge density. Dynamic factors comprise ligand stiffness, length of connecting agent, skeleton interpenetration, coordination number of SBU, hydrophobicity and connectivity between ligand and metal SBU.

The stability of a MOF due to the strength of metal coordination bonding with ligand matters, is mainly governed by Pearson's Hard and Soft Acids and Bases principle (HSAB) where hard acids (defined to possess low polarizability of the electron clouds because of small radius and high charge density) are attracted to hard bases and soft acids (defined to

possess high polarizability of the electron clouds because of larger radius and lower charge density) are attracted to soft bases. Many of the ligands used as linkers for MOF synthesis are multifunctional (multidentate) carboxylates containing oxygen atoms which are hard and are attracted to the hard tri- and four-valent metal ions. On the other hand, the soft di-valent metal ions such as $Cu^{2+,}$ and Zn^{2+} are best attracted to soft ligands e.g. ligand containing sulfur. That is why MOFs such as MOF-5 are relatively unstable as they are the result of a soft-hard metal-ligand pair synthesis[93].

Chapter 4. Inhalation Anesthetic Agents

4.1. Inhalation anesthetic agents and history

Inhalation anesthetic agents, also known as volatile anesthetics or inhaled anesthetics, comprise a class of substances that have recently gained increasing popularity over intravenous and gaseous anesthetics [94]. The most popular members of this family include halogenated ethers, such as sevoflurane and desflurane [95]. See also Figure 6.1 in Chapter 6 for a visual representation of their molecular structures. Sevoflurane is widely used for induction of pediatric general anesthesia. due to its relatively more pleasant odor and being less irritant to the breathing system [94]. Some of the physical characteristics of the two most popular inhalation anesthetics are listed in Table 4.1.

The exact mechanism by which IAA is still open to debate. Basically, IAA work within the central nervous system by enhancing signals to chloride and potassium channels while depressing neurotransmission pathways. Sevoflurane, and desflurane both decrease systemic vascular resistance resulting in decreased systemic blood pressure[96].

Table 4.1 Physical characteristics and clinical data of the two anesthetic gases

	Sevoflurane	**Desflurane**
Trade Names	Ultane	Suprane
Normal boiling point (°C)	58.5	22.8
Odor and color	sweet and colorless	clear, colorless, mildly pungent
Freezing point (°C)	below -78	below -78
State at room temperature	liquid	liquid
Molar mass (g/mol)	200.056	168.038
Chemical formula	$C_4H_3F_7O$	$C_3H_2F_6O$
CAS number	28523-86-6	57041-67-5
Critical molecular diameter (nm) [97]	71	53
Dipole moment (D) [97]	2.33	1.74
Polarizability volume (10^{-24} cm^3)	9.3	7.4

4.2. Vaporizers

Vaporizers are employed to create the desirable concentration of the anesthetic agent before being inhaled by the patient [96]. However, as the patient's body cannot metabolize most of the inhaled amount, a great deal of the administered dose of IAA is wasted during exhalation [4]. Adding leakage from the vaporizer into consideration, the IAA wastage can be significant and can pose a serious health risk to the non-patient staff of hospitals. Moreover, being relatively expensive and having significant global warming potential, simply venting them into the atmosphere is not recommended neither from environmental nor economic standpoint. The economic gains of reclaiming the wasted IAA is evaluated by Ang [95].

Vaporizers are differently designed depending on the type of IAA and their physical properties, including normal boiling point. For example, for sevoflurane (n.b.p. = 58.5°C) a Plenum type of vaporizer is used but for desflurane which has near-ambient or lower boiling point (n.b.p. = 22.5°C) a different vaporizer is employed. Vaporizers are used as an integrated part of "anesthetic machine". A picture of an anesthetic machine equipped with a sevoflurane vaporizer is shown in Figure 4.1[98].

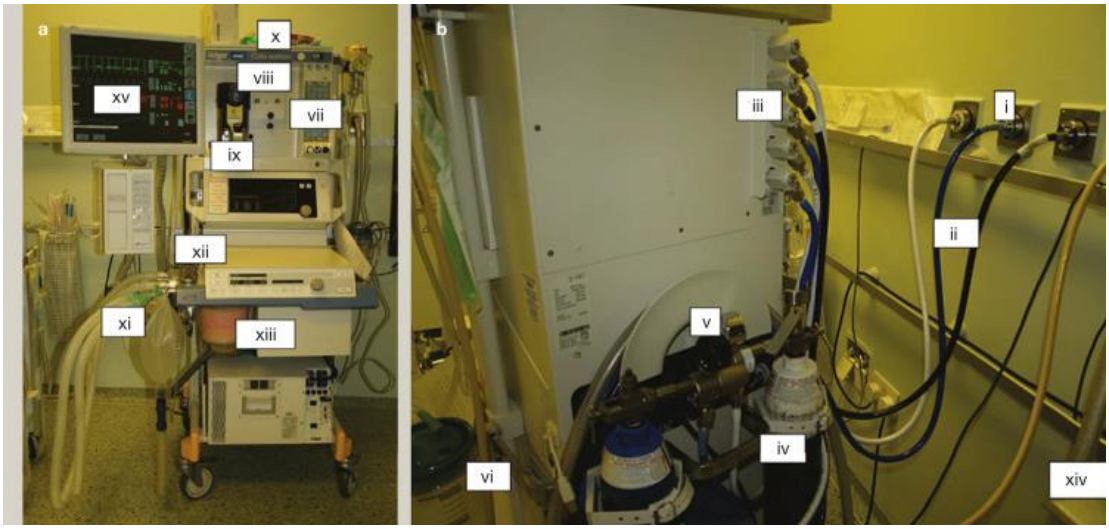

Figure 4.1 The back (a) and the front (b) of the anesthetic machine is shown. The following are identified: (i) piped medical gases and vacuum supply, with Schrader probes inserted into the Schrader terminal outlet or the walls; (ii) color coded pipes; (iii) non-interchangeable screw thread; (iv) gas cylinders (oxygen on the right and nitrous oxide on the left) mounted on the back of the machine; (v) Bourdon pressure gauges; (vi) suction apparatus, connected to the hospital vacuum supply by the yellow tubing near (ii); (vii) rotameters; (viii) back bar with empty vaporizer housing just below legend; (ix) sevoflurane vaporizer in position(x) emergency oxygen flush; (xi) circle system (attached via the common gas outlet which is not visible); (xii) adjustable pressure limiting valve; (xiii) carbon dioxide absorber; (xiv) scavenging tubing; (xv) patient monitoring system. [98]

Chapter 5. Molecular Simulation and Modeling

5.1. Introduction

Molecular simulation uses statistical mechanics to bridge between experiment and theory. In this method, ensembles are defined to model an array of microstates sharing the same macroscopic state such as pressure, temperature, volume, and total energy. For a typical molecular simulation, the following components need to be provided: 1) A description of the molecular system 2) a potential function describing the intramolecular and intermolecular interaction between like and unlike atoms. This function, which is traditionally known as forcefield, can have simple or complicated forms. It is usually composed of bonded terms (bond, bend, torsion) and non-bonded terms (Van der Waals dispersion and electrostatic, Coulombic forces). Simulations are carried out for known ensembles that depend on the property being sought for. As an example, microcanonical ensemble (NVE) refers to constant number of particles (N), constant volume (V), and constant total energy (E). NVE ensemble is used to calculate the resulting temperature. Also, it is important to decide which algorithm to use. Two well-known algorithms which perform molecular simulation include molecular dynamics (MD) and Monte Carlo (MC). Although both algorithms are at one point capable of simulating equilibrium and kinetic properties of matter, Monte Carlo[99] is mostly used for simulating equilibrium properties whereas Molecular Dynamics is often used for simulating kinetic, time-related phenomena, such as the diffusivity coefficients. More details about these two algorithms will be presented in Section 5.4.

5.2. Force field

Force fields are essential in molecular simulations in order to describe ground state energy for adsorbate molecules, adsorbent structure ,adsorbent-adsorbate as well as adsorbate-adsorbate interactions[100]. Examples of some generic force fields are TraPPE[99], UFF[101], and DREIDING[102].

The molecular potential energy can be described as a Taylor expansion of bonded and nonbonded terms and the cross terms. Such an expression, traditionally referred to as a force field, is thought to capture all chemical entities as well as physical properties. Examples of chemical entities are atoms, angles, and bonds. Examples of physical properties are equilibrium structures and vibrational spectra[13]. The bonded potential terms include such terms as bond-stretching, Urey-Bradley, bending, Wilson- inversion-bend, torsion, and improper torsion potentials. The nonbonded terms includes van der Waals, tail corrections and electrostatics. The cross terms result from interaction amongst different entities including bond-bond, bond-bend, bend-bend, bond-torsion, and bend-torsion potentials[13].

5.3. Crystal Information Files (CIF)

A crystal information file (CIF) is an essential part of any molecular simulation of adsorption. The file is obtained by running a single-crystal XRD (SC-XRD) measurement. It gives data about the relative positions of atoms within the structure, the bond angles, the size of the unit cell, the symmetry group of the crystal and sometimes the partial charges of the atoms.

To run a simulation involving a modified structure of an adsorbent, the CIF needs to be modified accordingly. Although cases of manual modification have been reported in the literature, it is more convenient to use recently developed software codes such as PoreModeMat.jl[103], MOFUN[104] and ToBaCCo[105] to generate or modify CIFs.

A lot of CIF files in databases are normally reported as cubic crystals with P1 symmetry [106]. For huge structures, it is more convenient to reduce their size to the *primitive* unit cell. Software such as Materials Studio [101] have offered the capability to convert a cubic CIF to a primitive CIF. The primitive CIF is often not cubic. For example, for MIL101Cr, the primitive CIF has triclinic symmetry[107].

5.4. Simulation Algorithms

In this section, the Molecular Dynamics and Monte Carlo algorithms introduced in section 5.1 are described in more detail.

5.4.1. Molecular Dynamics

Molecular Dynamics is a deterministic algorithm for solving a physical trajectory determined from initial position and initial velocity as input using Newton's Second Law of Motion for a many-body three-dimensional system[108]. Atoms are placed in a 'simulation box' with periodic boundary conditions. It is a way to approximate an infinite system- infinitely 'repeat' the small simulation box. Figure 5.1 summarizes the flow chart of a molecular dynamics simulation.

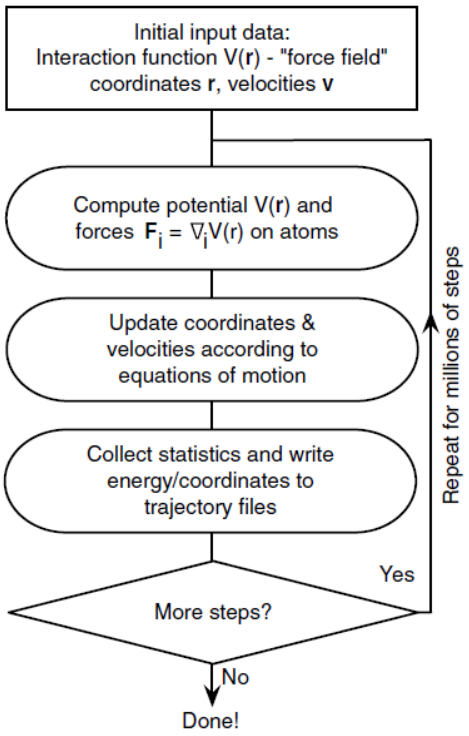

Figure 5.1 Molecular Dynamics Algorithm. At each step, calculated quantities are saved to an energy file. Temperature, kinetic energy, potential energy, pressure, volume etc. After the simulation, can view these changing over time and use them to calculate/output other properties such as density Source: Lindahl E. (2015) Molecular Dynamics Simulations. In: Kukol A. (eds.) Molecular Modeling of Proteins. Methods in Molecular Biology (Methods and Protocols), vol 1215. Humana Press, New York, NY. https://doi.org/10.1007/978-1-4939-1465-4_1

5.4.2. Monte Carlo

Molecular Dynamics method described above is based on Newton's Second Law of Motion in physics. As often said, it has a deterministic nature where each existing state can accurately predict the next state along a calculation trajectory. In contrast, Monte Carlo methods have a stochastic nature as they deal with probabilities. A random perturbation (called a *trial move*) in the existing state is performed to *tentatively* create a new state. Acceptance or rejection of this new state depends on the *configurational* energy of this new state compared to the existing one. If the trial move has led to a lower energy of the state,

it is instantly accepted. Acceptance of a new state resulting in higher energy depends on an additional criterion as follows. An algorithm known as a *random-number generator* creates a number say, a , where $0<a<1$. Then, the value of the Boltzmann probability function corresponding to the energy change is calculated to be say, b. If $b < a$, the new state can still be accepted, and rejected otherwise. The accepted new state will be stored as together with other accepted states from previous trial moves and forms a set known as an *ensemble*. An ensemble average is taken at the end which determines the value of the sought-for property. This process known as sampling has had several modifications starting from Markov chains to more sophisticated solutions resulting in better and faster routes to finding a global minimum in the energy. Figure 5.2 summarizes a cycle in Monte Carlo.

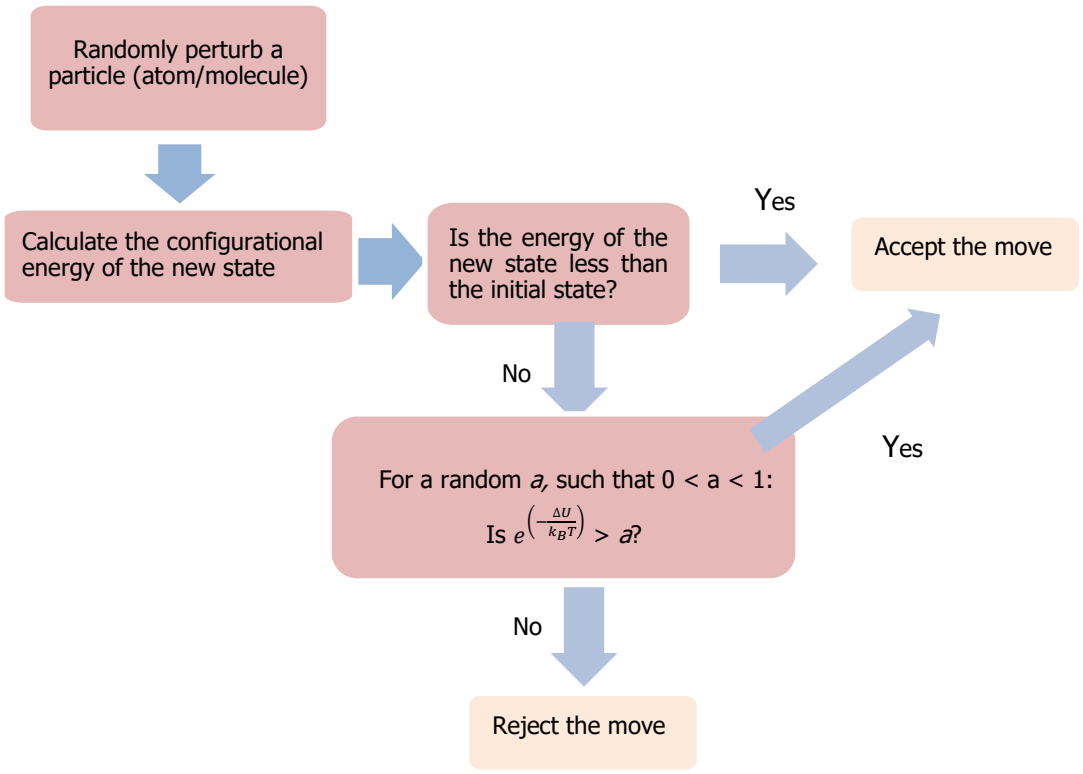

Figure 5.2. Atom movement is random; translation, rotation, etc. is accepted or rejected based on a calculated probability (Boltzmann's distribution) [109]

5.4.3. Molecular Dynamics *vs* Monte Carlo

Molecular Dynamics is the method of choice for many simulations involving either equilibrium or kinetic phenomena. However, there are cases where use of Monte Carlo is the preferred choice (or the only viable option) due to some limitations of MD[13]. For example, there are cases where non-physical trial moves are needed to achieve faster equilibration of the system. Examples of such cases include Gibbs Ensemble (GE) and Grand-Canonical Ensemble (GC) simulations. These two class of simulations are needed for VLE calculations and for gas/vapor adsorption isotherm predictions, respectively. These simulations involve *unreal* moves such as exchange of particles between a simulation box and particle reservoir (as in GC) or moving a particle between two boxes representing the two phases (as in GE). But MD algorithm is solely based on *physical* (happening in the physical world) trial moves and therefore cannot be employed for simulations involving GE and GC ensembles.

5.4.4. Advanced Monte Carlo sampling methods

Conventional (Metropolis) GCMC and GEMC work best only for small molecules. As the size of the molecules increase and chains or branches are formed, the probability of random trial moves decrease significantly and as result the simulation becomes excessively prolonged. This shortcoming has led to invention of alternative (more advanced) MC sampling techniques such as Configuration Biased MC (CBMC) sampling and Configuration Fractioned Component MC(CFCMC) as discussed below.

5.4.4.1.Biased Monte-Carlo schemes (Configurational Bias MC)

An example of systems that employ such scheme are polar molecules, hydrogen-bond forming molecules, and chain molecules. Such molecules need to be at the appropriate orientation. Finding the right orientation randomly is highly unlikely especially if the idea is to generate one that produces a Boltzmann-type distribution[13]. The main feature of CBMC sampling schemes is that they are no longer completely random in nature. Rather, they are biased in a way to increase acceptance probability of the trial move. Such a sampling scheme consists of an algorithm that bears great resemblance to the one introduced by Rosenbluth and Rosenbluth [110], but with the added advantage that follows Boltzmann distribution [111]. The algorithm separates the potential energy of interactions into orientation-dependent and non-orientation dependent terms. Consequently, a function known as Rosenbluth factor [112] is calculated using the non-orientation dependent term of the potential energy of the interaction. The ratio of the Rosenbluth weight for the new conformation vs the old conformation before the trial move determines the acceptance rule. The Rosenbluth scheme can involve growth of a segment of the molecule. Retracing the entire chain, leads to the determination of the Rosenbluth factor which by definition is the product of individual Rosenbluth weights [13].

5.4.4.2.Continuos Fractional Component Monte Carlo (CFCMC)

Continuos Fractional-component Monte Carlo [113][114][115] is another advanced MC sampling technique devised to help speed up MC simulations involving insertion and deletion trial moves [116]. At high pressures where densities increase, moving particles between the two phases becomes all more difficult. The solution has been to define a

parameter λ and $0 \leq \lambda \leq 1$. A value of zero corresponds to complete deletion whereas λ = 1 means full presence of the particle in either "box" or phase. This way one has defined a staged insertion-deletion move between phases[116].

5.5. Applications

Two of the applications of Monte Carlo simulations include VLE prediction[117] and gas adsorption[118]. The simulation uses Gibbs Ensemble[119] for the former and Grand-Canonical Ensemble[120] for the latter, respectively.

5.5.1. VLE prediction

Vapor-Liquid Equilibria can be predicted using molecular simulations. The most common method is called Gibbs-Ensemble Monte-Carlo where two boxes are defined: one for the liquid phase and the other for the vapor phase. The purpose is to find the situation where chemical potentials of both boxes converge to an identical value. Throughout the simulation, the pressure and temperature are kept constant and identical, but the size of the boxes will change resulting in a bigger box corresponding to lower mass density of the vapor phase and the other smaller box corresponding to the higher mass density of the liquid phase. The resulting simulation can help find the pressure, temperature, and density at the critical point. These data are crucial for use with equations of state such as Peng-Robinson EOS[121] to convert pressure to fugacity.

The GEMC described above can be hard to converge for large molecules or at low temperatures where moving a molecule from the vapor box into the much denser liquid

phase can prove cumbersome. To address such cases, alternative algorithms such as CFCMC as discussed in section 2.4.1.2. have been introduced[122].

5.5.2. Adsorption isotherms

Another example of molecular simulation involving Monte Carlo technique is for gas/vapor adsorption. Like the case of VLE prediction, the "unphysical" trial moves involve the transfer of particles between one box representing the particle reservoir and the other one representing the adsorbent solid phase. The ensemble is called grand canonical where chemical potential, volume and temperature are constant, and the simulation solves for the final density of the adsorbate on the adsorbent phase. The input data needed to run the simulation include: 1) description of the adsorbate 2) the CIF of the adsorbent 3) forcefield and forcefield mixing rules. These inputs generate the simulation input file**,** which is a summary of the simulation algorithm method used, the number of initiation/equilibration and production runs, the cut-off lengths, choice of truncation and tail correction method, the name of the adsorbate(s) , the choice of forcefield, and the name of the adsorbent.

5.6. Simulation software suites

To perform the molecular simulations, several commercial proprietary software packages as well as some house-built academic codes have been developed. Most of the codes especially the academic ones run on Linux operating system (OS) but there are also some for-Windows OS versions. RASPA[123], Cassandra [124] and MCCCS Towhee [125] are three of such suites capable of performing MC simulation. RASPA can also perform MD.

The additional advantage of RASPA is that it can account for the flexibility of adsorbate molecule bonds, as well as the flexibility of the MOF structure.

Other software is used for visualizing the simulation results, modify adsorbent structures or predict data needed for simulation input files. Examples include zeo++[126], Avogadro[127], VESTA[128], iRASPA[129], PoreModeMat.jl[103], and MOFUN[104].

5.7. High-Performance Computing

Often the personal computers do not possess sufficient speed and storage capacity to perform big and long molecular simulations. To this can be added that some software run solely on operating systems (OS) other than Windows, e.g. Linux, which is a lightweight and free OS. To address these limitations, consortiums of academic supercomputer clusters have joint forces into forming a national grid of computer nodes, thus sharing their resources. In Canada, the Compute Canada (now Allians Canada) can be accessed through membership mediated by the principal investigators and getting remotely connected using such software as MobaXterm to upload the input files and download the resulting output files. A well-defined queuing algorithm helps prioritize tasks submitted based on the number and size of nodes needed as well as the frequency of usage by the client. This way, a fair chance is given to all clients using the facility.

5.8. Development of the input files for the simulation of adsorption of IAA molecules

For simulation of adsorption of small molecules, use of the less complicated Monte Carlo sampling trial moves is often sufficient. However, for the larger and sometimes branched

molecules of IAA using only simple trials is not working and cannot produce results comparable to experiment, and/or as fast as for smaller molecules. In this section, the measures taken to provide acceptable results in outlined for the simulation of sevoflurane, an IAA, on the MOF MIL-101-Cr at 298K. After establishing the usefulness of the approach, the method was further applied to other IAA adsorbates and MOF adsorbents as described in Chapters 6 and 8.

5.8.1. Use of block files

As shown in Figure 5.3, the isotherm is overestimating the adsorption amount at higher partial pressures (above 0.2 of the relative pressure) while showing no uptake at lower concentration (below 0.2) One reason could be that the inaccessible pores have not been taken into consideration and therefore accessible surface area has been overestimated. Locating these inaccessible locations can be performed using zeo++ software which takes the adsorbate size and adsorbent pore size into account and saves the locations of these in accessible pores in an output file known as a "block file". It has been reported [130] for zeolites that block files can be used to correct the effect of overestimating the available surface area. Using the zeo++ software, a block file was defined for sevoflurane adsorption on MIL-101-Cr. For large adsorbates inside MOF, the conventional MC simulation becomes too slow at lowest and highest p/p_0. In other words, the red curve for simulation indicates that the (0-0.2) has not reached equilibrium yet. To solve this issue CFCMC (section 5.4.4.1) was used. The effect was further discussed in Section 5.8.3. below. Other measures were also taken as described in subsections 5.8.2. to improve the original

isotherm which finally produced the corrected isotherm as explained in Section 5.8.3 and shown in Figure 5.4.

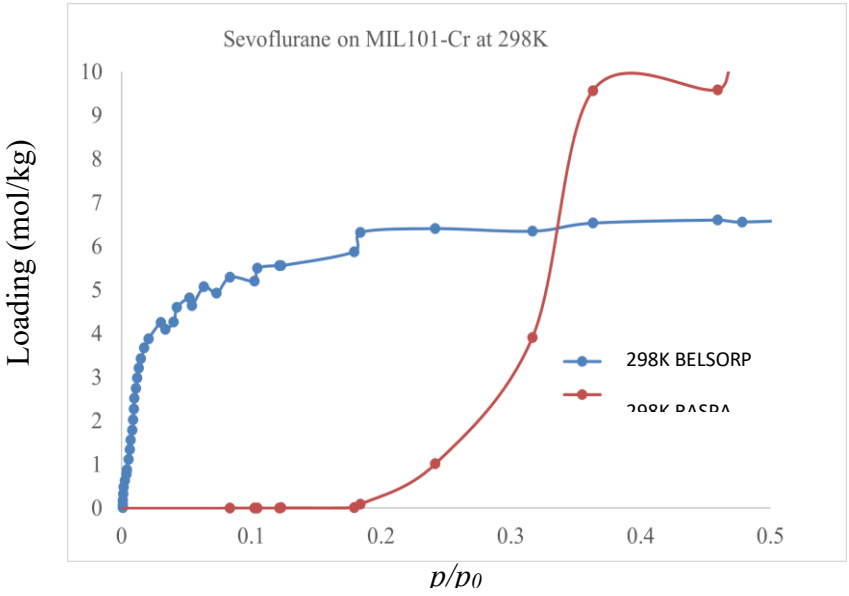

Figure 5.3 Original simulation isotherm (in red) vs. experimental isotherm (in blue)

5.8.2.Continuous Fractional-Component Monte Carlo (CFCMC)

Conventional MC works best for adsorption simulation of small adsorbate molecules in the medium range of relative pressures. For larger adsorbate sizes and/or for very dilute or concentrated amounts of adsorbates, the progress speed of simulation is adversely affected. This condition can be expected for the simulation of sevoflurane which is both relatively large (0.71 nm) and is administered in diluted amounts (1v% or p/p_0=0.04) during anesthetizing of the patient. As introduced in Section 5.4.4.2. Continuous Fractional-Component Monte Carlo (CFCMC) has been invented to tackle this issue by breaking up the molecule to smaller fragments and moving the fragments separately. The choice of the

fractions of the molecules should be decided by the user in advance. For the case of sevoflurane, five segments were identified. The configurations of these fragments were subsequently included in the sevoflurane definition file as shown in Section V of Appendix C. Moreover, use of CFCMC was indicated in the input file for RASPA as presented in Table 6.9S in Appendix C. The trial move attributed to CFCMC was given a weight of 70% of the total number of trial moves. This is indicated as a trial move ratio of 0.1, 0.1,0.1, 0.7 in the input file for RASPA (See Table 6.9S in Appendix C). As observed during simulation, implementation of this technique helped significantly speed up the isotherm simulation of sevoflurane in RASPA. The combined effect of using CBMC and CFCMC in improving the original isotherm is summarized in Section 5.8.3.

5.8.3.Sevoflurane isotherms on MIL-101-Cr

GCMC algorithm in RASPA suite was used to run the isotherm for adsorption of sevoflurane on MIL-101-Cr at 298K. The results are shown in Figure 5.4. When compared to Figure 5.3. a clear improvement is visible as verified by the results from volumetric adsorption instrument (BELSORP) at the same temperature.

The reason why the simulation is working better this time can be attributed to the use of block files as described in section 5.8.1. which (1) prevent overestimation of the accessible surface area inside the adsorbent as well as CFCMC sampling (2) providing correct adsorbate orientation and (3) speeded up the simulation progress, respectively. The positive effect of CFCMC was especially significant in the 0 -0.2 range of p/p_0.

Sevoflurane can produce unfavourable Type 5 isotherm as shown for MOF-177-Zn due to self-clustering of adsorbates [131]. Nevertheless, for MOFs which possess CUS, such as MIL-101-Cr, it becomes Type 4 if the pressure increased until saturation with a hysteresis loop at the high-pressure range. The shoulders will be visible due to the presence of two distinctive mesopore cages of 2.9 and 3.4 nm in diameter, respectively; even though, for low ranges of pressure, see Figure 5.4, the isotherm can look like a Type I isotherm.

The isotherms for sevoflurane on MIL-100-Al and MOF-177-Zn were also generated in Chapter 6, sections 6.3.3 and 6.3.4. as presented in that chapter. The approach was further applied to modified structures of MIL-101-Cr ,too, as described in Chapters 8.

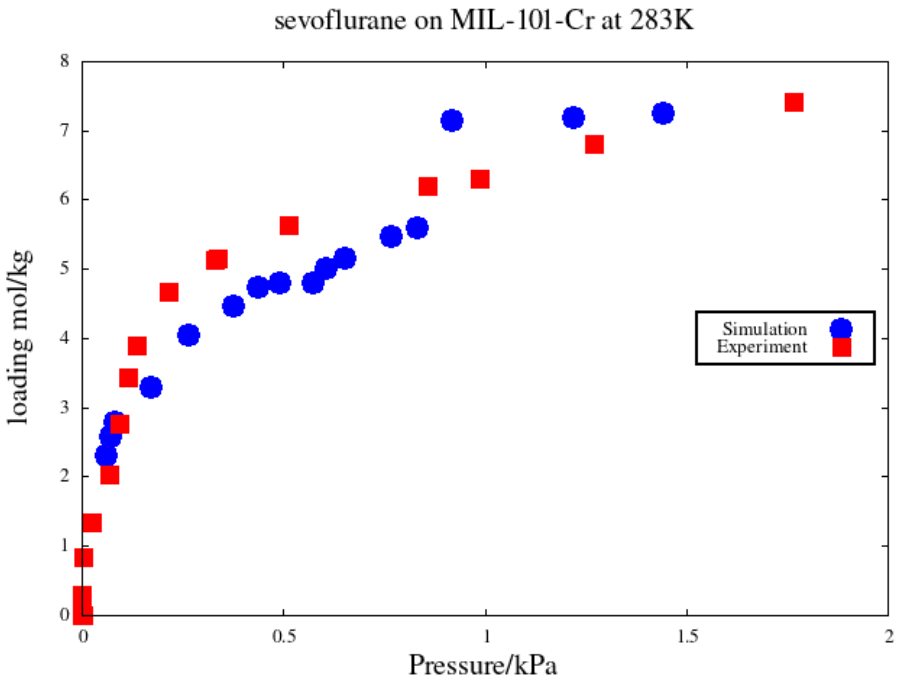

Figure 5.4 Improved isotherm of sevoflurane on MIL-101-Cr at 298K after implementation of the new approach

Chapter 6. Use of molecular simulation for evaluating adsorption equilibrium of inhalation anesthetic agents on metal-organic frameworks

Masoud Haeri-Nejad[1], *Mladen Eic*[1*]

[1]*Department of Chemical Engineering, University of New Brunswick, Fredericton, NB, Canada*

Chapter 6 has been already published as a research paper in the Canadian Journal of Chemical Engineering April 2024, pages 1646-1657

Abstract

Metal-organic frameworks (MOFs) were studied as alternatives to zeolites and activated carbon for adsorptive removal of wasted inhalation anesthetic agents (IAA). Monte Carlo simulation was used to predict equilibrium adsorption isotherms of IAA on selected MOFs. Rather than generic forcefields, the all-atom FF parameters published by Arcario were used for IAA modeling. Continuous Fractional Component Monte Carlo (CFCMC) proved crucial for speedy simulation of large molecules. We found that allocating 70% probability to the CFlambdaSwap move gave optimum fits between simulation and experiment. The simulations provided us with an insight into the adsorption mechanisms of IAA in these structures. Heats of adsorption, BET surface area and total pore volume were deduced to be the crucial parameters for low, medium, and high range of relative pressures in the isotherm. Therefore, the chromium atoms in MIL-101-Cr are

better adsorbers of IAA than MIL-100-Al at lower pressures despite the similarities in terms of the type of linkers, and topology. Our simulation results corroborated with the earlier published studies on self-association behavior of sevoflurane molecules based on the experimental isotherms reported for MOF-177-Zn. Finally, the high polarity of IAA is thought to explain good low-pressure simulation/experiment data agreement for the MOFs possessing coordinated unsaturated sites (CUS) despite using generic DREIDING forcefield for the framework atoms. Our in-house parsing code helped realize that the GCMC simulation speed is not the same for all pressure points. It demonstrates that simulation at higher pressures becomes slower. The reason is that as the density of the adsorbate molecules inside the framework increases, Monte Carlo sampling becomes statistically less successful.

Key words: *molecular simulation, Grand-Canonical Monte-Carlo, GCMC, adsorption isotherms, inhalation anesthetic agents, sevoflurane, desflurane, metal-organic frameworks, adsorbate self-association, Monte Carlo trial moves.*

6.1. Introduction

Inhalation anesthetic agents, also known as volatile anesthetics and inhaled anesthetics, comprise a class of substances that have recently gained increasing popularity over intravenous and gaseous anesthetics [94]. The most popular members of this family include sevoflurane and desflurane [95]. In particular, sevoflurane is widely used for induction of pediatric general anesthesia due to its relatively more pleasant odor and being

less irritant to the breathing system [94]. The structures of the two compounds are shown in Figure 6.1.

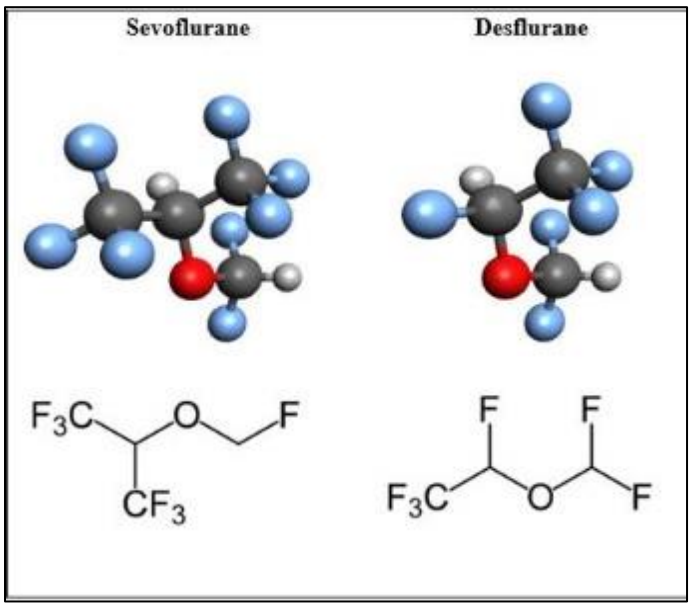

Figure 6.1 Molecular structures of inhalation vapor anesthetics

Some of the physical characteristics of the two most popular inhalation anesthetic vapors are listed in Table 6.1. Clinical data are also summarized in Table 6.1S in Section IV of Supplementary Information.

Table 6.1 Physical characteristics and clinical data of the two anesthetic gases

	Sevoflurane	**Desflurane**
Trade Names	Ultane	Suprane
Normal boiling point (°C)	58.5	22.8
Odor and color	sweet and colorless (cloudy)	clear, colorless, mildly pungent
Freezing point	below -78 °C	below -78 °C
State at room temperature	liquid	liquid
Molar mass (g/mol)	200.056	168.038
Chemical formula	$C_4H_3F_7O$	$C_3H_2F_6O$
CAS number	28523-86-6	57041-67-5
Critical molecular diameter [97]	7.1 Å	5.3 Å
Dipole moment [97]	2.33 D	1.74 D
Polarizability volume, (10^{-24} cm^3)	9.3	7.4

Vaporizers are employed to create the desirable concentration of the anesthetic agent before being inhaled by the patient [96]. However, as the patient's body cannot metabolize most of the inhaled amount, a great deal of the administered dose of IAA is wasted during exhalation [4]. Adding leakage from the vaporizer, the IAA wastage can be significant and can pose a serious health risk to the non-patient staff of hospitals. Moreover, being relatively expensive and having significant global warming potential, simply venting them into the atmosphere is not recommended. The economic gain of reclaiming the wasted IAA is evaluated by Ang [95].

Adsorption has already been recognized as a useful recovery method for atmospheric pollutants and several studies have been published suggesting adsorbents for IAA removal including activated carbon [2][3], zeolites [1][3] [4] [5][10], MOFs [7][8][9], and aerogels [3].

As adsorbents, MOFs are especially interesting as they have much higher surface areas and their pore sizes are more tunable. With up to 90,000 MOF already synthesized so far and hundreds of thousands more hypothetical structures predicted [11], the challenging task of making a selection of the most suitable candidate is only feasible through molecular simulation. The advantage of classical molecular simulations such as Monte Carlo and Molecular Dynamics is that they can predict physical properties of a given structure before performing experimental characterization. They can also help with proposing structural modifications before synthesizing the modified structure first. As an example, recent CO_2 adsorption studies on MIL-100-Fe and MIL-100-Cr [17] using GCMC helped elucidate the contribution of different types of atoms in the structures, the heat of adsorption and a better understanding of CO_2 adsorption mechanism. Molecular simulation can also make valid predictions of the adsorbate properties.

Our literature search reveals that very little has been done using molecular simulation to predict the physical properties of inhalation anesthetic agents such as their critical properties and mass densities and/or their adsorption isotherms where even experimental values are scarce [4].

In this study, three MOF structures MIL-101-Cr, MIL-100-Al, and MOF-177-Zn were investigated for their equilibrium adsorption capacity towards inhalation anesthetic agents, sevoflurane (SF), and desflurane (DF). For MOF-177-Zn we published experimental data [132] which have only included SF adsorbate. As we did not have access to the adsorbent sample used therein, no DF measurement could be performed. Nevertheless, MOF-177-Zn is an interesting case for the fact that unlike MIL-101-Cr and MIL-100-Al, it has no CUS in its metal cluster.

MIL-101-Cr has been extensively studied for its applications for various purposes including water adsorption [133] and air separation [134]. Each chromium atom in this MOF is coordinately connected to three ligand molecules including two water molecules and an anion. The nature of the anion depends on the choice of the modulators during synthesis. If HF is used, the anion can be a mixture of F^- and OH^- in varied proportions. MIL-101-Cr is known for mesoporous cages, high stability (even in boiling water) and durability towards successive adsorption/desorption cycles [76]. If sufficient thermal energy is applied, the coordinated water ligands surrounding the Cr atoms can be removed leading to two open-metal sites (OMS), also known as coordinatively unsaturated sites (CUS).

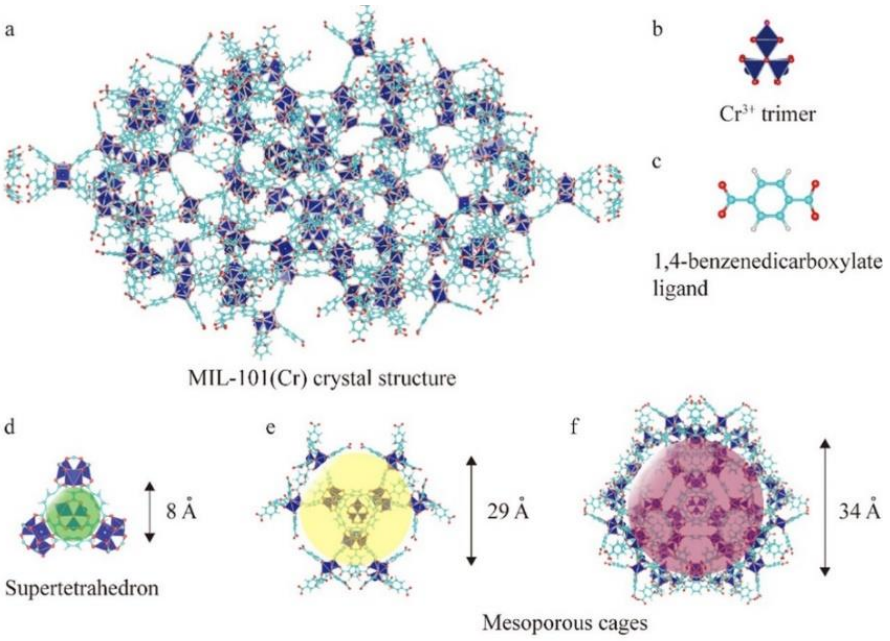

Figure 6.2 (a) 3D structure (b) Metal trimer (c) ligand linker (d) supertetrahedron (8 Å) (e) medium cage (f) large cage (34 Å), courtesy of [135]

MIL-100-Al has the formula of $Al_3X\ (H_2O)_2\ O[C_6H_3(CO_2)_2.\ nH_2O$, (X= F^-, OH). It is very similar to MIL-101-Cr in topology. The difference is the choice of the organic linker precursor as shown in Figure 6.3. It has been reported that it can produce a maximum of one CUS [136].

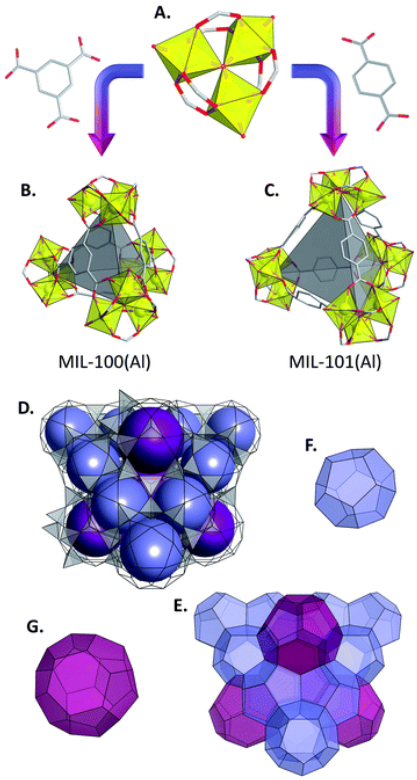

Figure 6.3 Molecular structure of MIL-100(Al) and MIL-101(Al) [77]

MOF-177-Zn is a structure consisting of a $[Zn_4O_6]^{6+}$ cluster and 1,3,5-benzenetribenzoate (BTB) ligand linkers [132]. This structure is almost unimodal in terms of pore size distribution (10Å and 11Å) and does not have open-metal sites unlike the former two structures mentioned above [22] (see Figure 6.4).

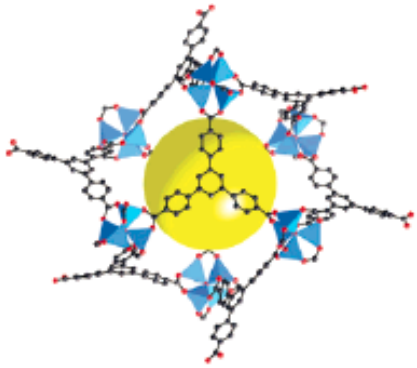

Figure 6.4 Molecular structure of MOF-177(Zn) [137]

6.2. Materials and Methodology

6.2.1. Experiment

Sevoflurane (98%) and desflurane (95%) were obtained from Blue-Zone Technologies Ltd. (Toronto, ON, Canada).

MIL-101-Cr (X=F, OH) was obtained from the following sources:

a) Crystal powder synthesized at the University of Naples Federico II, Italy [6] . Henceforth referred to as Cr-MOF-1

b) Crystal powder synthesized at the University of Naples Federico II, Italy. Henceforth referred to as Cr-MOF-2. The synthesis procedure for Cr-MOF-2 is the same as Cr-MOF-1. The only difference lies in the linker precursor, terephthalic acid, which in this case is preliminarily obtained from the depolymerization of PET, with the purpose of making the final product cheaper and more environmentally friendly. We characterized the two compounds separately and found them to be identical. The results are summarized in Section I of Supplementary Information

MIL-100-Al was prepared and characterized at Materials Center of Technical University of Dresden, Germany using a new low-temperature method, leading to spherical agglomerates of nanocrystals [2]. Analytical data for this MOF is included in Section I of Supplementary Material.

Commercial MOF-177-Zn was purchased from Aldrich by Dr. Caputo's research group at the University of Naples Federico II Italy. Experimental sevoflurane isotherm at three

distinct temperatures were also performed in Italy and their results were published in a separate study [132].

Textural properties of Cr-MOFs were determined from N_2 physisorption at 77K performed using our BELSORP-max instrument (BEL Japan, Inc.). The specific surface area, the total pore volume, and the pore size distribution were evaluated using the data analysis software BELMaster V6.1.0.4. The samples were pretreated by degassing at 423K for 10 hours. Powder X-ray diffraction (PXRD) patterns for MIL-101-Cr samples were obtained using a Bruker D8 Advance spectrometer with a 2.2 kW Cu X-ray tube source, maintained at an operating current of 40 kV and 25 mA. Samples were scanned in the range of 5-80^o 2θ. A step size of 0.02^o and a step time of 1.0 sec were used during the measurements. TGA/DSC measurements were performed using our SDT-Q600 (TA Instruments, USA). The samples were heated from room temperature to 600 °C at a ramp rate of 5 °C/min while being purged with nitrogen at a flow rate of 100 ml/min. A Perkin Spectrum 100 FT-IR spectroscope with Diffuse Reflectance sample holder (DRIFTS) was used to record the middle-IR spectra for Cr-MOF-1 crushed and Cr-MOF-2 powder.

For MIL-100-Al and MOF-177 we used the characterization data provided by our collaborator researchers who had performed the syntheses. The results are summarized in Section I of Supplementary Information.

6.2.2. Molecular simulations

For adsorption simulation, the adsorbent, adsorbate, and their interaction were modeled. For giant MOF structures such as MIL-101 and MIL-100, ab-initio modeling of the

structure was not possible until fairly recently [138]. Instead, crystal information files are usually prepared from XRD measurements. We used the CIF files available in published literature. MIL-101-Cr-primitive CIF used in this paper was first published in [24] and included in RASPA archive of structures. The CIF for MIL-100-Al was taken from [23], and we later calculated the partial atom charges using the charge equilibration method implemented in RASPA. CIF for MOF-177 was also taken from RASPA archive which is part of the software package.

IAA molecules were modeled using the forcefield reported by Arcario et al. [139] and the critical properties and saturated vapor pressure values were calculated. Table 6.5S in the Supplementary Information lists the saturated vapor pressure values from the model next to the experimental values [96].

A code was written in MATLAB to generate the input files and folders of all set points for a given simulation at once (See Supplementary Information). Linux-based codes were also prepared to parse sample simulation progress as well as generate whole isotherms in real time on demand (see Section 3 of the Supplementary Information).

RASPA v2.037 software package [123] was used to run Grand-Canonical Monte Carlo (GCMC) simulation to generate adsorption isotherms. Non-bonding interactions were modelled using the Lennard-Jones (LJ) and Coulomb potentials:

$$U_{ij}(r_{ij}) = 4\varepsilon_{ij}\left[\left(\frac{\sigma_{ij}}{r_{ij}}\right)^{12} - \left(\frac{\sigma_{ij}}{r_{ij}}\right)^{6}\right] + \frac{1}{4\pi\varepsilon_0}\frac{q_i q_j}{r_{ij}} \quad (1)$$

$$\sigma_{ij} = \frac{\sigma_i + \sigma_j}{2} \qquad \varepsilon_{ij} = \sqrt{\varepsilon_i \varepsilon_j}$$

(2)

Where i and j are indices of the interacting atoms, r_{ij} is the distance between atoms i and j, ε and σ are the LJ parameters, ε_0 is the vacuum permittivity, and q is the partial charge. For MIL-101-Cr atoms, LJ parameters were taken from the values reported by Dubbeldam [37]. For IAA Forcefield LJ parameters and partial charges by Arcario were used. LJ parameters between unlike atoms are calculated using the Lorentz-Berthelot mixing rules and LJ potentials. The cut-off beyond 12.0 Å are shifted to zero without tail-correction. To account for the Coulombic interactions, partial atomic charges are calculated using charge equilibration method [140] in electrostatic interactions with a relative precision of 10^{-5}. All MOF frameworks were assumed to be rigid, but the flexibility of the adsorbate molecules was considered using available forcefields in RASPA. All three dimensions of the simulation supercell are greater than twice the cut-off distance of 12.0 Å to make sure the minimum image convention is satisfied. The adsorbate description files are included in Section VI of Supplementary Information.

The GCMC simulations for isotherm pressure points were run simultaneously and consisted of 50,000 equilibration cycles followed by 1,000,000 production cycles using translation, rotation, swap (insertion or deletion with equal probabilities), and CFSwapLambda trial moves with probabilities of 0.1, 0.1, 0.1, and 0.7, respectively. The choice and relative amount of the moves were based on the fact that the adsorbate molecules are relatively large. To avoid getting stuck in the pores, we made use of

Continuous Fractional Component Monte Carlo [141] (CFCMC). The Peng-Robinson equation of state is the default EOS utilized. Additional GCMC simulation details can be found in Section 2 of the Supporting Information**.** All simulations were run on the BELUGA cluster of Compute Canada national computation network. The codes are included in Section 3 of Supplementary Information.

Table 6.2 summarizes critical properties of sevoflurane and desflurane based on the forcefield by Arcario [139] as recommended by Smith and Škvára [142].

Table 6.2 Critical properties of sevoflurane and desflurane [142]

Name	**T_C/K**	**P_C/bar**	**ρ_C/kg · m^{-3}**
Sevoflurane	513.62	28.78	455.68
Desflurane	496.63	36.88	506.51

Finally, the simulation results were validated by comparison with data from volumetric-adsorption experiments using our BELSORP-max (Bell, Japan) and are summarized independently in Supplementary Information Section I and included in combination with the graphs in the Results and Discussion Section.

6.3. Results and Discussion

A code was written in MATLAB to generate the input files and folders of all set points for a given simulation at once. Other Linux-based codes were prepared to parse sample

simulation progress as well as generate whole isotherms in real time on demand. Both codes are included in Section VI of Supplementary Information.

In general, discrepancy between simulation results and experimental data may be observed in some cases, which could be because of a deviation of the ideal model structure of the MOF or adsorbate molecule from the actual synthesized material. A Simulation usually assumes perfect crystalline structure of the MOF, whereas in practice the structure can have defects. These defects can act as highly active sites and therefore exhibit deviations from theoretically predicted values. There is also a case of more than one phase or collapsed structures due to shaping processes [143]. Moreover, amorphous phases might be formed as a result of residual solvents inside the cages [144]. Finally, incomplete activation could be another cause of discrepancy.

6.3.1. Sevoflurane on MIL-101-Cr

Figures 6.5a-c compares the RASPA simulation results with the experimental data obtained by Belsorp for the adsorption of sevoflurane on MIL-101-Cr at three distinct temperatures of 283K, 298K, and 308K, respectively. Satisfactory agreement is observed especially at lower partial pressures, which is significant for dilute solutions dealt with in practice.

Figure 6.6a shows the isosteric heat of adsorption obtained by comparing experimental data at 298K and 308K using the BELMASTER software. Generally, the heat of adsorption is expected to start from a high value at low pressures and decrease with increasing pressure. Such behavior is typical when the solid-fluid interactions are more significant at

lower pressures but are overwhelmed by adsorbate-adsorbate interaction at higher pressures. The simulation results were also compared with experimental results from Gargiulo and coworkers [6] (see Figures 6.12aS and 6.12bS in Supplementary Information). Their results were found to be slightly different because their samples were degassed at 298K and as a result the coordinated water molecules were still attached to chromium metal sites. In our case, for both the simulated and physical structures the coordinated waters are removed. Still, the similarity of the values for isosteric heats of adsorption at around 50 kJ/mol indicates that even when the CUS sites are shielded by water molecules they can act as active adsorption sites.

Our in-house parsing code also helped realize that the GCMC simulation speed is not the same for all pressure points but decreases for higher pressure points. This can be explained by increased density of the adsorbates making successful trial moves less probable.

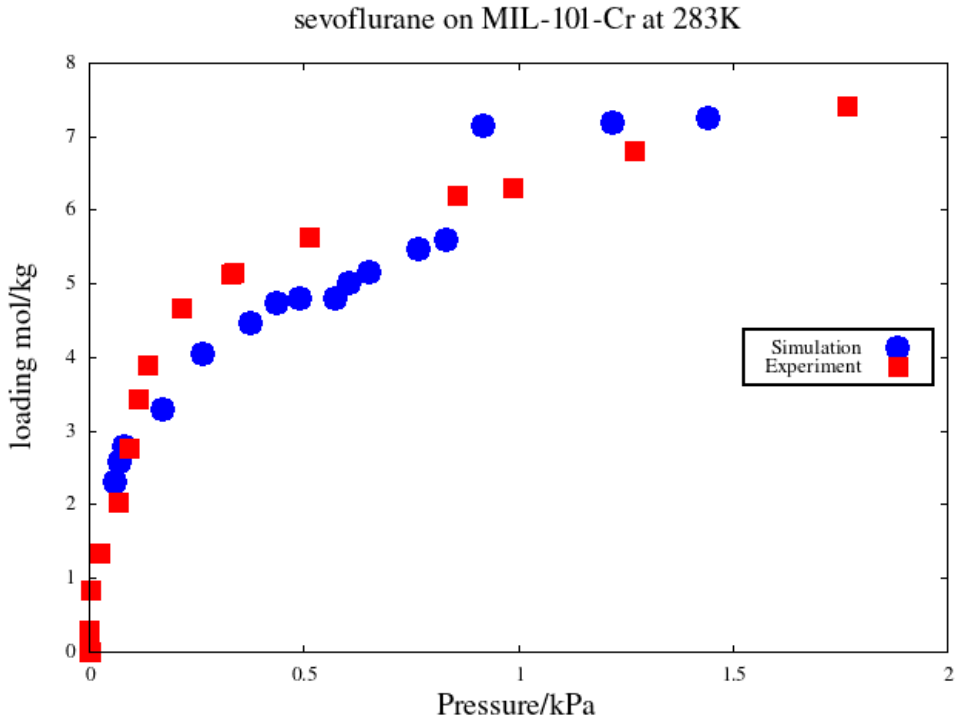

Figure 6.5a RASPA simulation results (blue solid spheres) for adsorption of sevoflurane on MIL-101-Cr at 283K compared with experimental results (red solid squares) from BELSORP

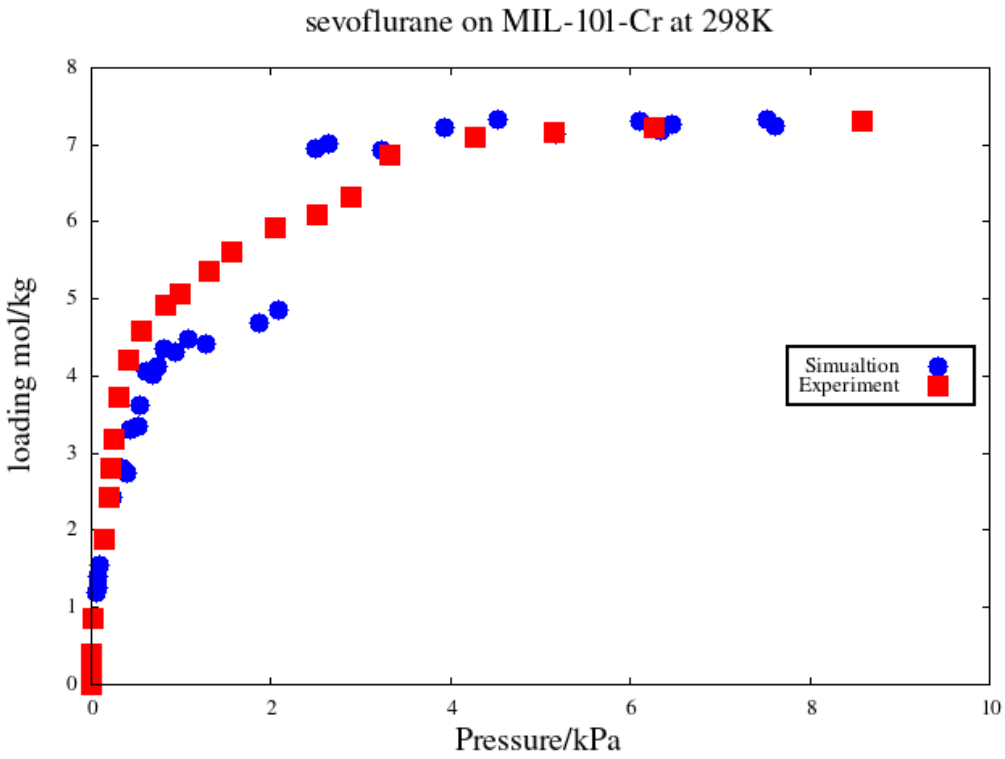

Figure 6.5b RASPA simulation results (blue solid spheres) for adsorption of sevoflurane on MIL-101-Cr at 298K compared with experimental results (red solid squares) from BELSORP

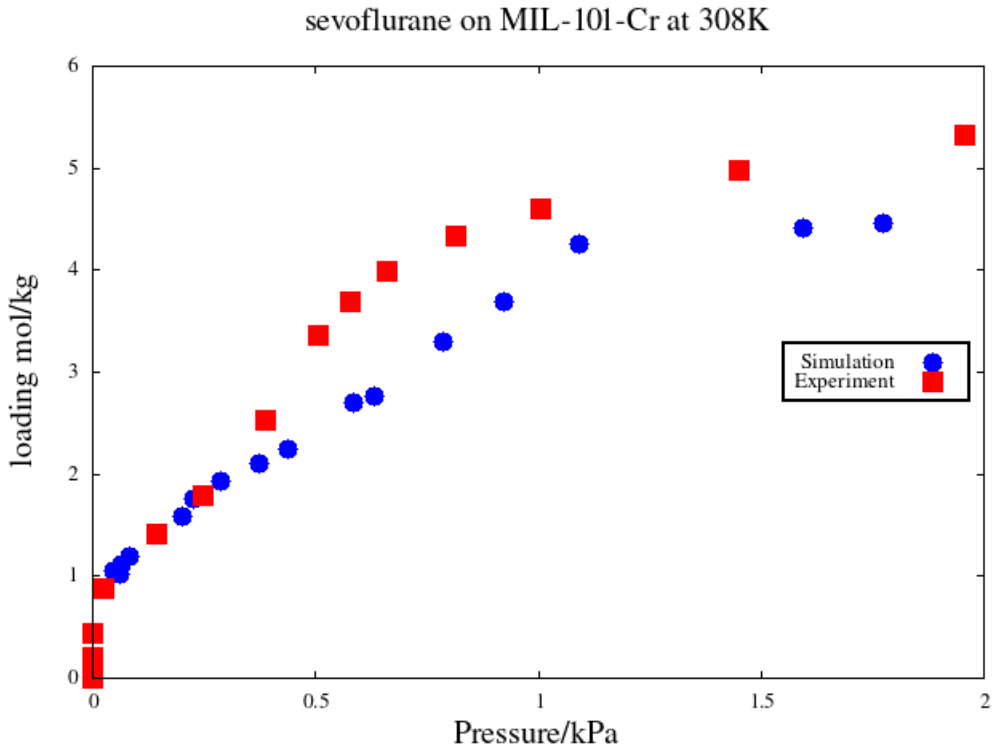

Figure 6.5c RASPA simulation results (blue solid spheres) for adsorption of sevoflurane on MIL-101-Cr at 308K compared with experimental results (red solid squares) from BELSORP

A discrepancy can be observed between simulation and experiment in cases where distinct 'bumps' were observed in the simulated adsorption isotherms especially in Figures 6.5a and 6.5b at about 1 kPa and 2 kPa, respectively. As discussed in [145] for the case of PCN3 MOF, which similar to MIL-101-Cr possesses a micro/mesoporous structure, a stepwise order of pore-filling is expected. The simulation snapshot shown in that study further reveals that molecular simulation recognizes face- and node adsorption inside the mesoporous cages as two sequential stages leading to a bump in the simulated adsorption

isotherm. However, in the experimental method, the sorbate molecule does not appear to make such a distinction during mesopore-filling [31].

Referring to the plots for isosteric heat of adsorption (Figure 6.6a) and the radial distribution function (Figure 6.6b) further reveals the variation of the affinity of SF towards MIL-101-Cr during adsorption.

The shape of the isosteric heat of adsorption for MIL-101-Cr confirms the heterogenous nature of the adsorption surface.

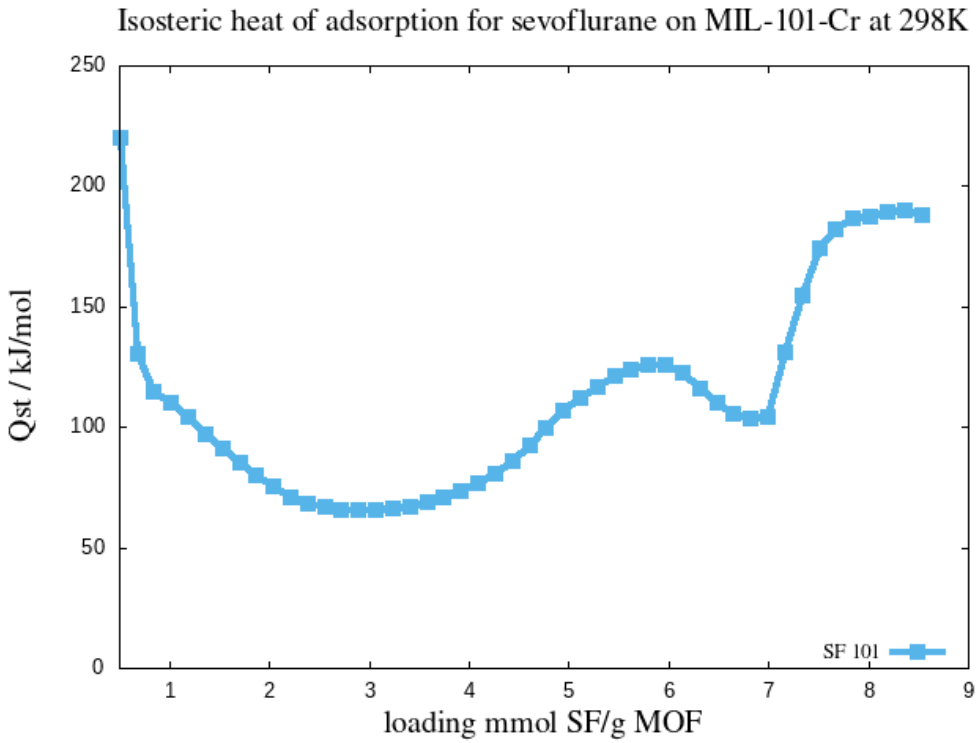

Figure 6.6a Isosteric heat of adsorption for sevoflurane on MIL-101-Cr

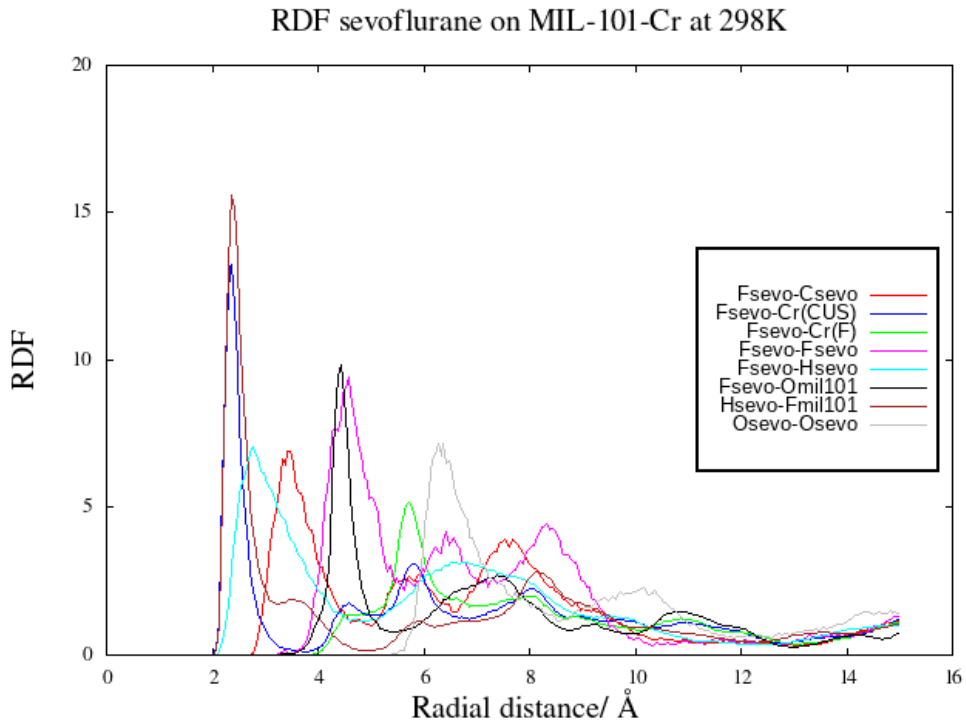

Figure 6.6b Radial distribution function of sevoflurane on MIL-101-Cr at 298K. Distances for the most significant interactions at a medium coverage of 5 adsorbate molecules per unit cell

Sevoflurane is an ether with a bulky $CH(CF_3)_2$ group on one side of the oxygen atom and a smaller CH_2F group on the other end. Observing the RDF (Figure 6.6b) confirms that the interactions between the MOF and SF are from the smaller head of the adsorbate and mostly involve interactions (1) between the fluoro atom of the sevoflurane (Fsevo) and the unsaturated Cr of the MIL101-Cr: (Cr (CUS)) and (2) between the two hydrogens on the small side of sevoflurane (Hsevo) and the fluoro group of the MOF (Fmil101). This fluoro group is in turn connected to a chromium atom in the MOF structure (Cr(F)). The F-F and O-O interactions are indicative of cluster formation between the sevoflurane molecule closest to the CUS chromium and the sevoflurane molecules in the bulk of the gas.

6.3.2. Desflurane adsorption on MIL-101-Cr

Figures 6.7a-b compare the RASPA simulation results with the experimental data obtained by Belsorp for the adsorption of desflurane on MIL-101-Cr at two distinct temperatures of 278K and 288K, respectively. As the normal boiling point of desflurane is about 295K, these lower temperatures were chosen. Figure 6.8 is the plot of isosteric heat of adsorption obtained by comparing experimental data at 278K and 288K using the BELMASTER software.

DF (5.4 Å) has a smaller diameter than SF (7.1 Å) and therefore we expect that more DF molecules can fit into the pore cages. Comparison between the heats of adsorption for SF and DF shows similar energies; however, at lower partial pressures, the adsorption energy is significantly lower for DF than for SF which indicates a possibility of selective removal of SF from DF in dilute binary mixtures using MIL-101-Cr.

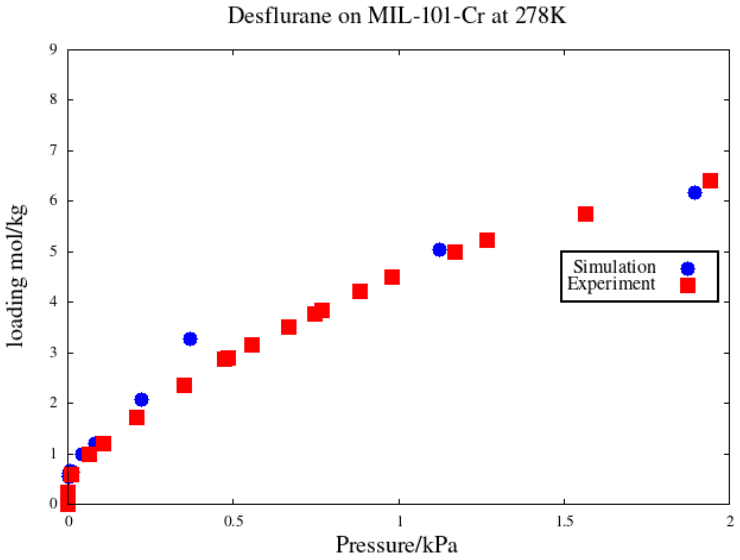

Figure 6.7a RASPA simulation results (blue solid spheres) for adsorption of desflurane on MIL-101-Cr at 278K compared with experimental results (red solid squares) from BELSORP

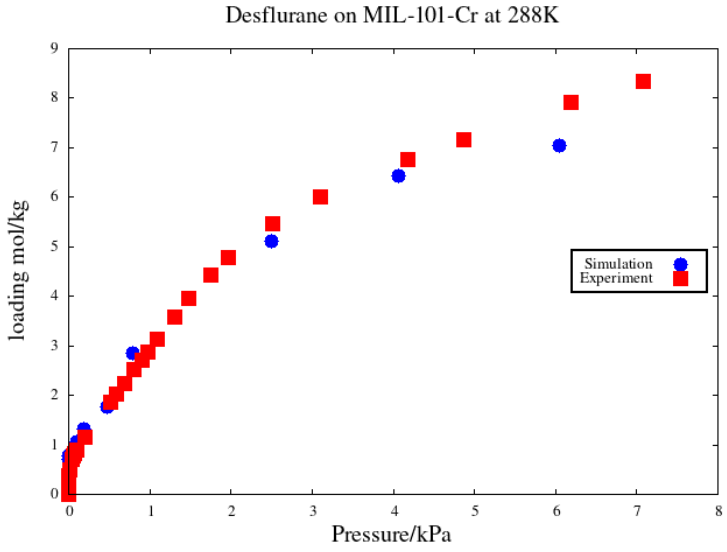

Figure 6.7b RASPA simulation results (blue solid spheres) for adsorption of desflurane on MIL-101-Cr at 288K compared with experimental results (red solid squares) from BELSORP

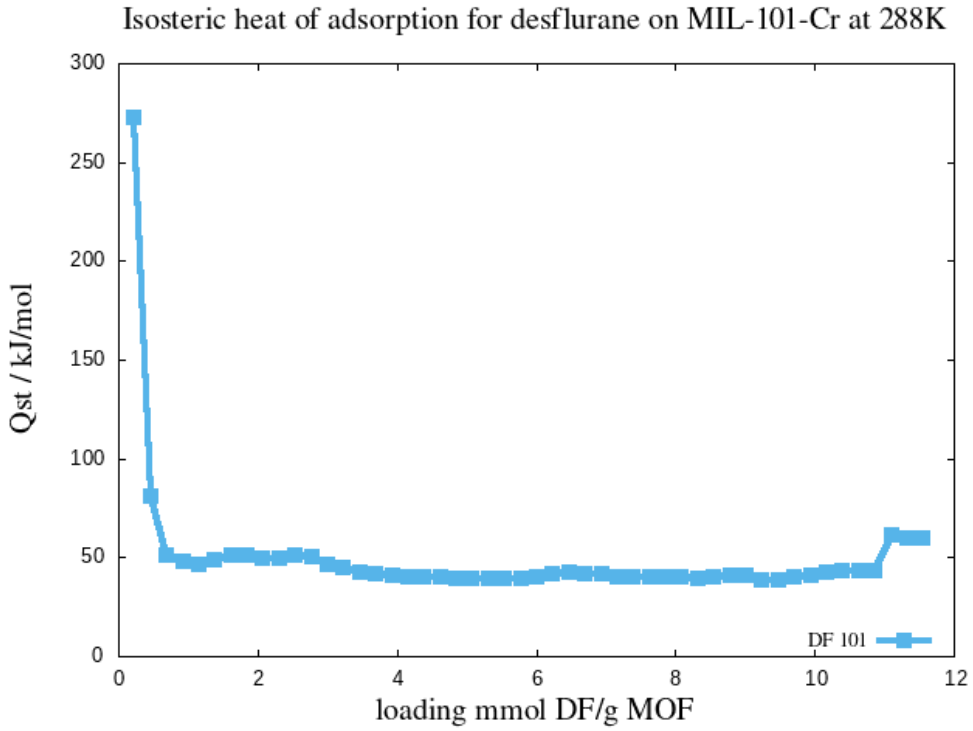

Figure 6.8 Isosteric heat of adsorption for desflurane on MIL-101-Cr

6.3.3. Sevoflurane and Desflurane adsorption on MIL-100-Al

Molecular simulation of adsorption for sevoflurane on MIL-100-Al is presented for three temperatures and compared with experiment as shown in Figures 6.9a-c. The simulated isotherm for desflurane on MIL-100-Al at 278K is also shown in Figure 6.11.

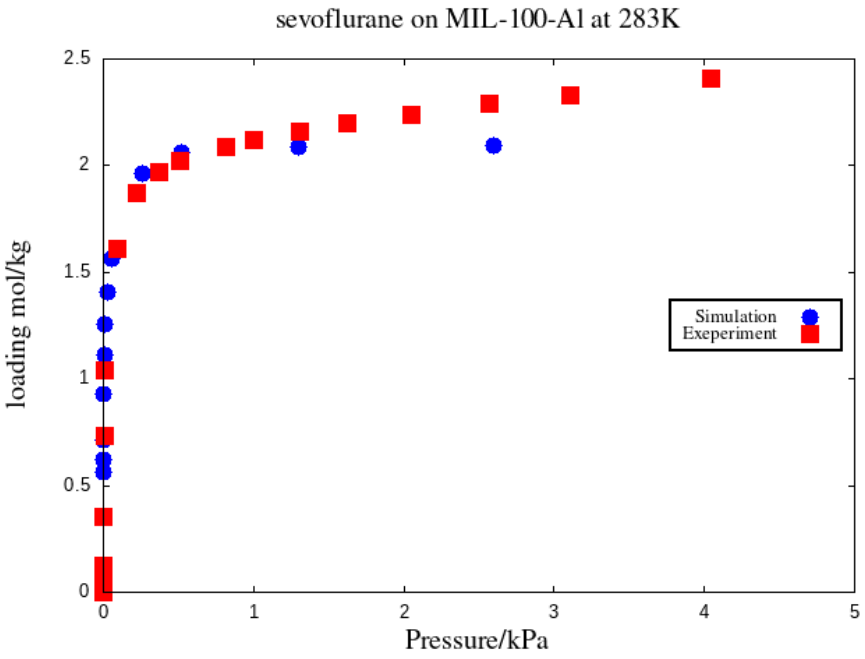

Figure 6.9a RASPA simulation results (blue solid spheres) for adsorption of sevoflurane on MIL-100-Al at 283K compared with experimental results (red solid squares) from

BELSORP

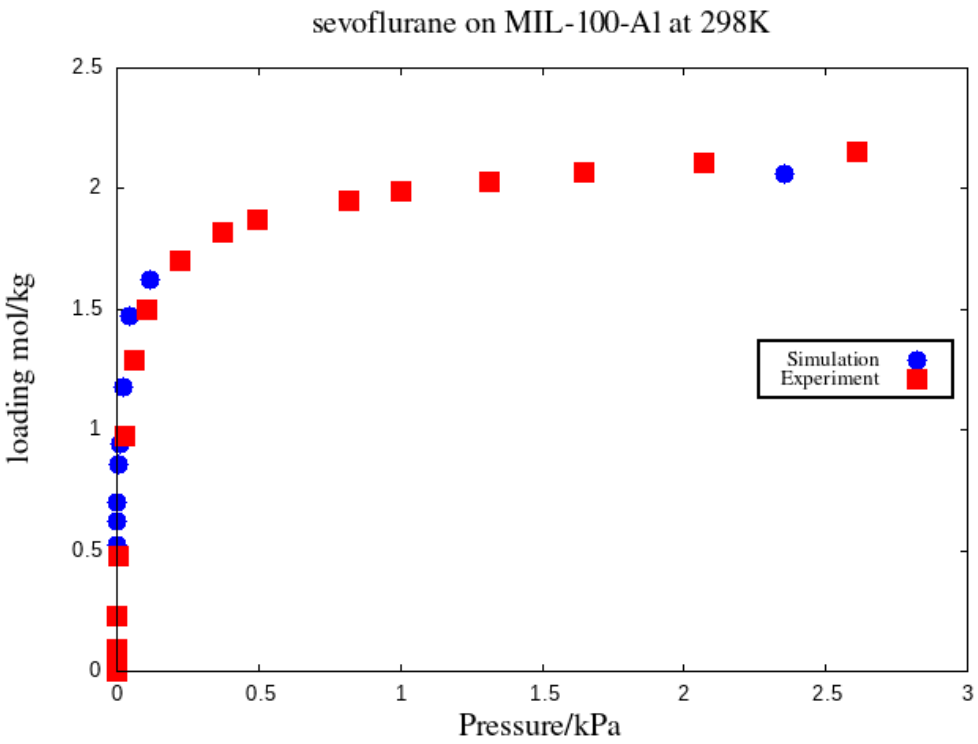

Figure 6.9b RASPA simulation results (blue solid spheres) for adsorption of sevoflurane on MIL-100-Al at 298K compared with experimental results (red solid squares) from BELSORP

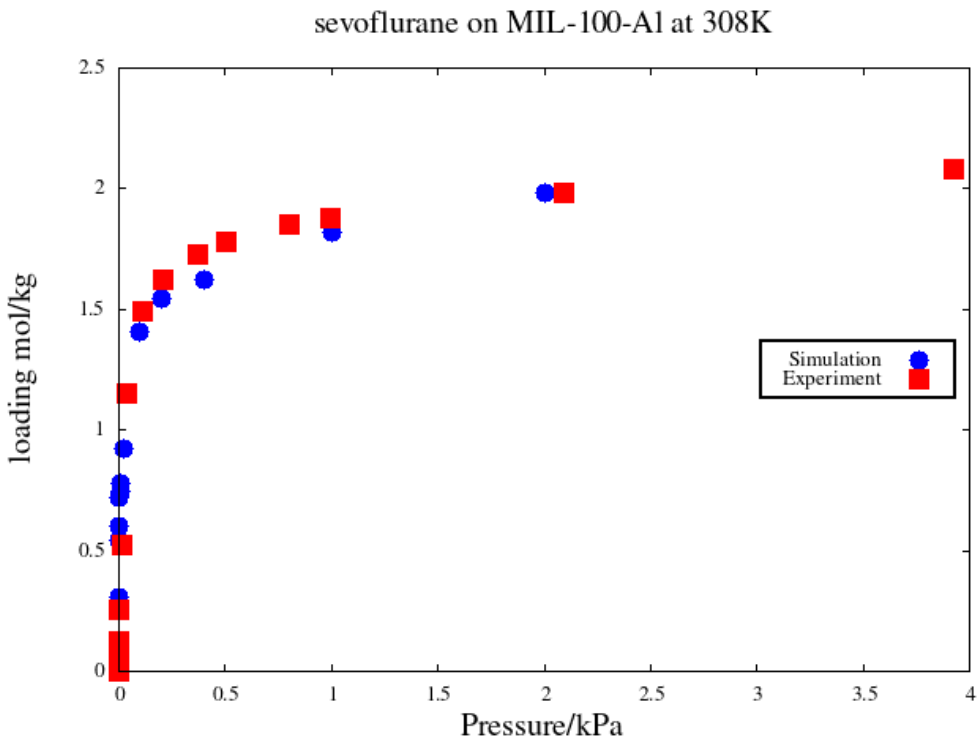

Figure 6.9c RASPA simulation results (blue solid spheres) for adsorption of sevoflurane on MIL-100-Al at 308K compared with experimental results (red solid squares) from BELSORP

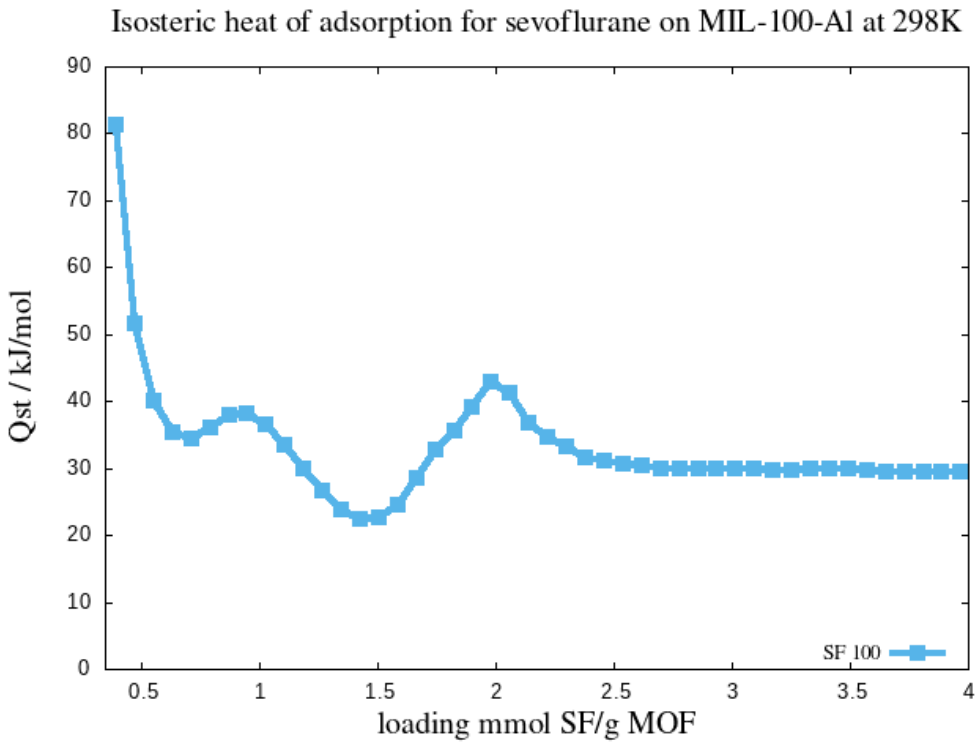

Figure 6.10 Isosteric heat of adsorption for sevoflurane on MIL-100-Al at 298K

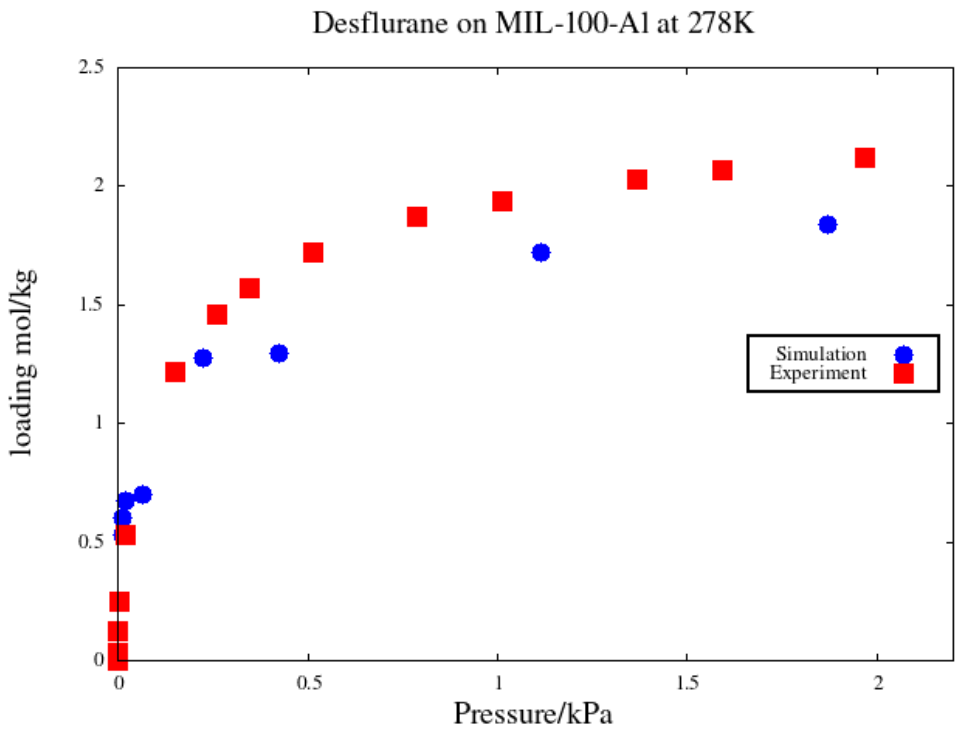

Figure 6.11 RASPA simulation results (blue solid spheres) for adsorption of desflurane on MIL-100-Al at 278K compared with experimental results (red solid squares) from BELSORP

Figure 6.10 shows the isosteric heat of adsorption for sevoflurane on MIL-100-Al at 298K. The interesting thing about this figure is the inhomogeneous energy surface. This kind of graph is typical of heterogenous surfaces and in this case due to the existence of CUS, micropores ,and mesopores in the MOF structure [146]. Still, the occurrence of this phenomena is very much dependent on the nature of the adsorbate, too. A possible reason that bumps are visible in MIL-100-Al but not in MIL-101-Cr can be due to the lower value

of Q_{st} in MIL-100-Al (34 kJ/mol) compared to MIL-101-Cr (60 kJ/mol) which makes these fluctuations significant.

Another issue is achieving good agreement between simulation and experiment at low relative pressures for CUS-containing such as MIL-101-Cr and MIL-100-Al. It has been reported that in low-pressure zone where the CUS active site is still partially occupied and the interaction between the solid and fluid is strong, the generic MOF forcefields such as DREIDING or UFF would underestimate the uptake and therefore special forcefield parameters are recommended to account for CUS interactions [147]. However, in our work, this is not the case. It seems that the polarity of the adsorbate molecule plays a role, too [148]. For generic FF of MOFs, the simulation-experiment agreement is worst for low to medium polarity molecules and best for high polarity molecules [147]. The fact that IAA molecules have high polarities (2.33D for SF and 1.74D for DF, see Table 6.1) can explain the good agreement achieved for IAA without the need to define additional FF parameters.

At higher relative pressure, though, accuracy of adsorption simulation on MOFs with CUS is significantly dependent on the choice of the FF for adsorbate molecules. Such an effect has only been reported for mesoporous MOFs [148].

6.3.4. Sevoflurane adsorption on MOF-177-Zn

The experimental results for adsorption of sevoflurane on MOF-177-Zn which has already been reported and discussed in an earlier publication [132] was compared with our simulated isotherm as summarized in Figures 4.12a-c. Unlike MIL-101-Cr and MIL-100-Al studied above, MOF-177-Zn does not have coordinated unsaturated sites. This is also

visible in the isotherm shape which is a type V isotherm. As studied by Gargiulo [132], self-association of the sevoflurane molecules in the absence CUS and a relatively uniform pore-size distribution is responsible for this peculiar shape of isotherm. The reported isosteric heat of adsorption for SF on MOF-177-Zn [132] at is lower than SF on MIL-101-Cr at 52 kJ/mol [6], which indicates weaker adsorbent-adsorbate interaction for MOF-177-Zn. Although this feature is desirable for cyclic adsorption processes by reducing the adsorbent regeneration energy demand, MOF-177-Zn is unstable and can totally decompose within 5 weeks when exposed to ambient humid air conditions [149].

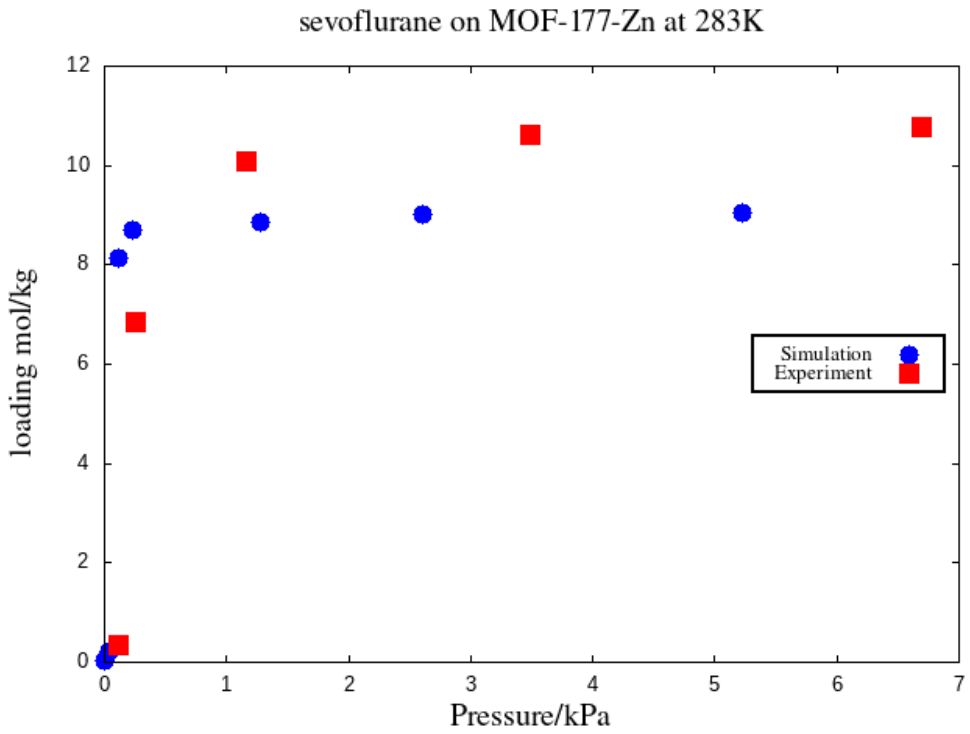

Figure 6.12a RASPA simulation results (blue solid spheres) for adsorption of sevoflurane on MOF-177-Zn at 283K compared with corresponding reported experimental results (red solid squares) from literature [132].

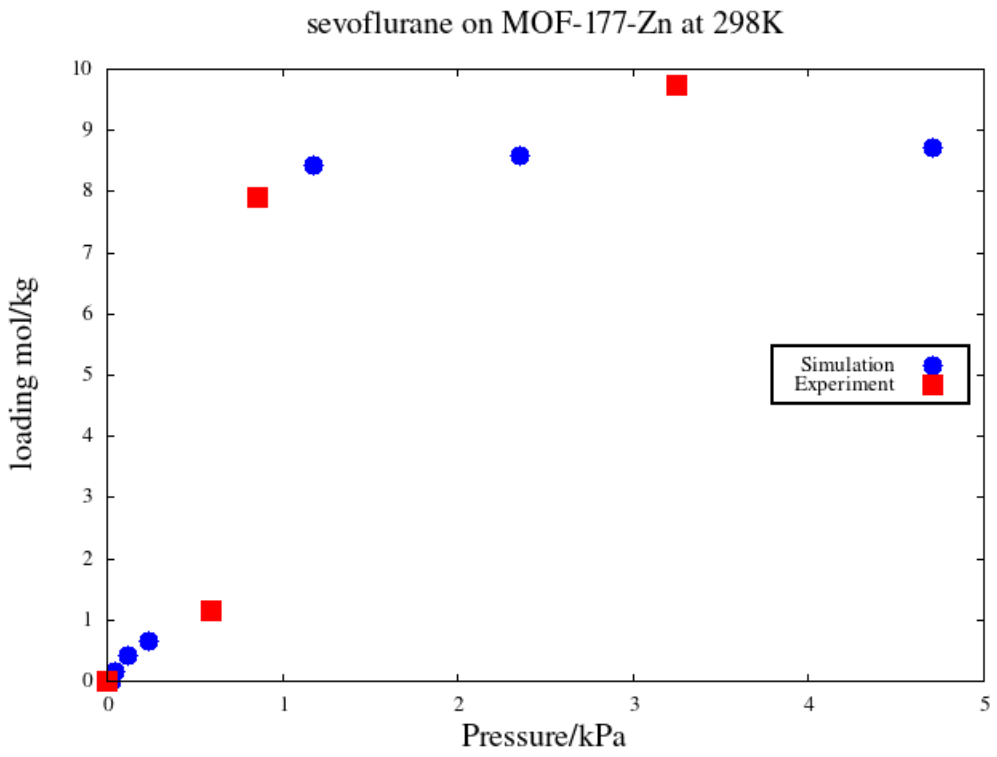

Figure 6.12b RASPA simulation results (blue solid spheres) for adsorption of sevoflurane on MOF-177-Zn at 298K compared with corresponding reported experimental results (red solid squares) from literature [132].

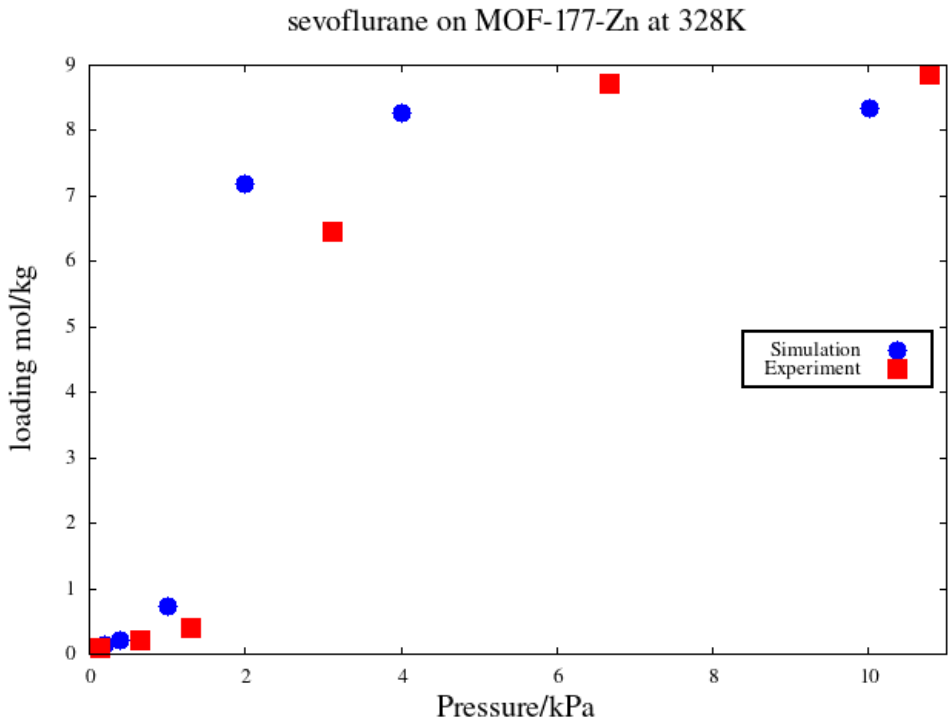

Figure 6.12c RASPA simulation results (blue solid spheres) for adsorption of sevoflurane on MOF-177-Zn at 328K compared with corresponding reported experimental results (red solid squares) from literature [132].

6.3.5. Comparison of the three adsorbents

Referring to the physical data summarized in Table 6.6S in SI, the S_{BET} and porosity of the three structures are in the following order: MOF-177-Zn > MIL-101-Cr > MIL-100-Al. And in terms of total pore volume: MIL-101-Cr > MOF-177-Zn > MIL-100-Al. Moreover, based on Table 6.1S in SI, the administration and scavenging concentration of the IAA is 1-2 vol% corresponding to 1-2 kPa.

An ideal adsorbent should also be stable in ambient atmosphere including moisture. Comparison of the isotherms and heats of adsorption in the foregoing sections (as summarized in Tables 8S and 9S in SI) suggests that MIL-101-Cr has the highest affinity towards both SF and DF. On the other hand, MOF-177-Zn has the highest uptake for SF at targeted working concentration. Moreover, MOF-177-Zn is the only adsorbent of the three that has already been commercially produced in large scale. However, its vulnerability towards moisture [149] makes it unfit for such applications. It can be concluded that MIL-101-Cr is the most suitable of the three MOFs investigated.

6.4. Conclusions

Metal-organic frameworks (MOFs) are an interesting alternative to zeolites and activated carbon for adsorptive removal of wasted inhalation anesthetic agents (IAA) due to MOFs higher surface areas and structural diversity. We studied the utility of molecular simulation of adsorption of large- molecular vapors of inhalation anesthetic agents on three MOFs. All MOFs in the study have mesopores large enough to accommodate the IAA molecules. To model the IAA molecules, we made use of forcefields specific to each adsorbate published by Arcario which includes parameters to account for molecular flexibility. Application of Continuous Fractional Component Monte Carlo (CFC MC) proved essential for speedy simulation of these large molecules provided that the right choice of the type and relative probability of the trial moves are considered. We found that allocating 70% probability to the CFlambdaSwap MC trial move gives the best fit between simulation and experiment.

The exceptionally good agreement between experiment and simulation at the lower partial pressures using generic FF for MOFs with CUS can be attributed to the high polarity of the IAA molecules which compensates for the CUS effect of the metal clusters. The choice of the FF for IAA is thought to be critical only for medium to higher pressures where adsorbate-adsorbate interactions become more significant.

Our molecular simulation results also corroborated earlier reports on self-association of sevoflurane molecules [132] which is responsible for the kink observed in the isotherm of IAA on MOFs such as MOF-177-Zn whose structures do not contain open-metal sites.

6.5. Acknowledgments

The authors (Masoud Haeri-Nejad and Mladen Eić) are grateful for the NSREC Discovery Grant. Our thanks also go to Dr. S. Kaskel and Dr. S. Hausdorf at TU Dresden for the synthesis of the MIL-100-Al samples. Dr. D. Caputo and Dr. N. Gargiulo are thanked for the MIL-101-Cr samples. Mr. S. Cogswell (UNB Biology Microanalysis and Microscopy) is acknowledged for assistance with SEM images, Dr. V. Reddy (UNB Earth Sciences) for XPRD spectra and Dr. L. Liu (UNB Chemical Engineering Surface Analysis) for Raman spectra of the MIL-101-Cr samples. This research was enabled in part by support provided by BELUGA (www.beluga.computecanada.ca) and the Digital Research Alliance of Canada (alliancecan.ca). I would like to thank Dr. S. Vassiliev at ACENET cluster of Compute Canada at UNB for assistance with installation of RASPA simulation software on BELUGA and the enhanced running of it on the national cluster.

Chapter 7. Post-Synthetic Modification/Functionalization of MOFs

7.1. Introduction

One of the attractive features of the MOFs is their greater potential for tuning the pore structure and size**,** as well as the possibility of changing the surface functional groups. In this chapter, a preview of some of the aspects related to post-synthetic modification/functionalization (PSM/F) of MOFs is discussed. Furthermore, the tools used for modification of crystal information files (CIF) are introduced. By modifying the CIF, it becomes possible to predict adsorption isotherms for modified structures derived from the pristine MIL-101-Cr. See Chapter 8.

7.2. Experimental methods of post-synthetic modification

Post-synthetic modification can have different purposes; sometimes it is applied when a desired structure cannot be synthesized directly (in one pot). Another reason could be to explore how to enhance certain properties of a MOF structure for a given application[40].

7.3. Molecular Modeling of post-synthetic modification

Sometimes, it is advantageous to predict how a certain modification can improve the performance of a MOF before doing synthesis/modification of the structure in the laboratory. One of the aspects of molecular simulation is its predictive power, especially when hazardous conditions and/or reagents are involved during the synthesis and/or the process where the modified structure is being used.

7.4. Development of input files for Post-synthesis modification

Starting with MIL-101-Cr ($X=F^-$) as the benchmark structure, the X = F was transformed to X=Cl by using ion exchange to obtain MIL-101-Cr ($X=Cl^-$). MIL-101Cr -NH_2 and NO_2-MIL-101-Cr were also synthesized. Finally, NH_3 was grafted to MIL-101-Cr ($X=F^-$) resulting in NH_3@MIL-101-Cr ($X=F^-$). The new structures were characterized, and their IAA adsorption isotherms were measured using the traditional volumetric method (see Chapter 8) and the rapid ZLC technique (see Chapter 10).

For the simulation part, the recently developed MOFUN software [104] was used to create new CIFs corresponding to NH_2-MIL-101-Cr and NO_2-MIL-101-Cr structures by adding NH_2 and NO_2 functional groups randomly on the benzene rings of the linkers in MIL-101-Cr . F was replaced with Cl manually when needed and used Bovia Material Studio DMOL^3 software for geometry optimization of the structure .i.e.to make sure the atoms in the MOF are in their equilibrium state ChEq method available in RASPA was utilized to assign the partial charges of atoms of the MOF. New blockfiles (see Chapter 5 , section 5.8.3) had to be for the new structures too using zeo++.

For design of the CIF for NH_3@MIL-101-Cr (X=F-) the strategies used above was not effective and another software named ToBaCCo was implemented to make the conventional cubic structure first before using Materials Studio[76] to make cubic into primitive structure. All the structures were prepared in the primitive form because of its smaller size compared to conventional form. The primitive form of the crystal is the smallest possible size of its unit cell. But as the files generated from XRD are in conventional form, one needs tools and software to create the primitive form. The fact that

primitive form contains fewer number of atoms (reduced by 75%) can result in remarkable decrease the computational effort and time. See Section I of Supplementary Information of Appendix D for the protocol used for CIF modification using the above-mentioned software.

An example of the suggested computational PSM is given in Figures 7.1 and 7.2 where the CIF for MIL-101-Cr ($X=F^-$) is transformed into NH_2-MIL-101-Cr ($X=F^-$), respectively using MOFUN.

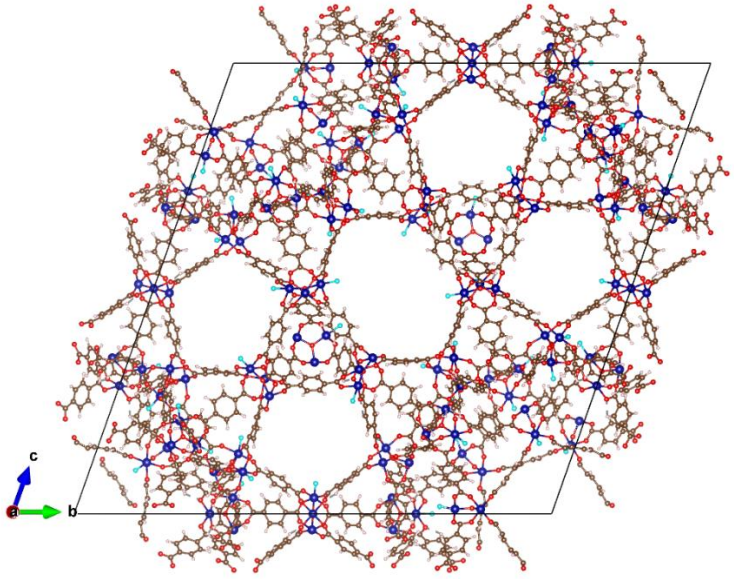

Figure 7.1 Visualization of the CIF for MIL-101-Cr ($X=F^-$) using Vesta[128] software.

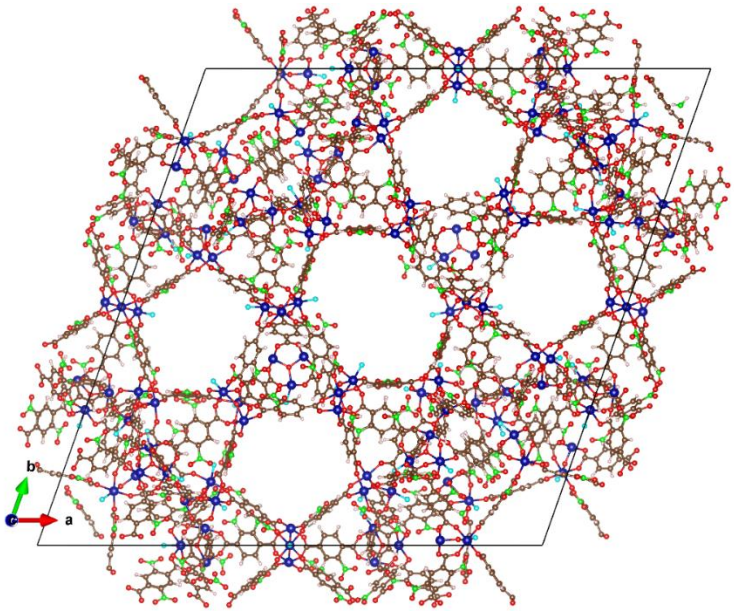

Figure 7.2 Visualization of the CIF for NH_2-MIL-101-Cr ($X=F^-$) using Vesta[128] software after functionalization of the linkers using MOFUN software.

.

Chapter 8. Use of molecular simulation to design modification of a chromium-based MOF for adsorptive removal of inhalation anesthetic agents

Masoud Haeri-Nejad[1], Mladen Eic[1]*

[1]Department of Chemical Engineering, University of New Brunswick, Fredericton, NB, Canada

Chapter 8 has been already published as a research paper in the Canadian Journal of Chemical Engineering July 2024 *DOI: 10.1002/cjce.25454*

.

Abstract

MIL-101-Cr-X (X=OH^-, F^-) has been reported to be the most suitable material so far for adsorptive removal of inhalation anesthetic agents (IAA) sevoflurane and desflurane at the working conditions in the hospital operation rooms. To further enhance its affinity and uptake capacity towards IAA, several structural modifications were proposed, and their isotherms were predicted using our molecular simulation approach adopted in our previous publication for the case of the pristine MIL-101-Cr (X=F^-, OH^-) structure. The proposed modifications include (1) grafting the metal-cluster site with coordinated NH_3 ligands to produce MIL-101-Cr@NH_3 (X=F^-, OH^-) (2) anion exchange of the fluorine atom bonded to chromium with chlorine to synthesize MIL-101-Cr (X=Cl^-) and (3) functionalization of the benzene rings of the ligand linkers in the MOFs with amino- and nitro- groups in order to form NH_2-MIL-101-Cr (X=Cl^-) and NO_2-MIL-101-Cr (X=Cl^-), respectively. Simulated

adsorption isotherms of IAA on these modifications were verified by the experimental results using the standard volumetric technique. The results clearly demonstrated that MIL-101-Cr@NH_3 ($X=F^-$, OH^-) possesses the highest equilibrium capacity for IAA. The new compound can significantly enhance the economy of adsorptive removal of IAA from vented gas mixtures.

Key words: *molecular simulation, post-synthetic modification/functionalization, inhalation anesthetic agents, adsorption isotherms, sevoflurane, desflurane, metal-organic frameworks, adsorbent ranking, working adsorption capacity*

8.1. Introduction

MIL-101-Cr has been extensively studied for its applications to various purposes including water adsorption [133], air separation [134], hydrogen storage [150], and CO_2 capture [151]. Each metal cluster trimer in this structure (see Figure 7.1d) accommodates two unsaturated chromium atom sites, each coordinated to a water ligand molecule. The third chromium atom accommodates an anion that neutralizes the overall positive charge of the trimer. The nature of the anion depends on the choice of the modulators used during synthesis. If hydrofluoric acid (HF) is used, the anion can be a mixture of F^- and OH^- in varied proportions. MIL-101-Cr is known for possessing mesoporous cages, high stability (even in boiling water) and durability towards successive adsorption/desorption cycles [76]. If sufficient thermal energy is applied, the coordinated water ligands surrounding the Cr atoms can be removed leading to two open-metal sites (OMS), also known as coordinatively unsaturated sites (CUS); see Figure 8.1(b).

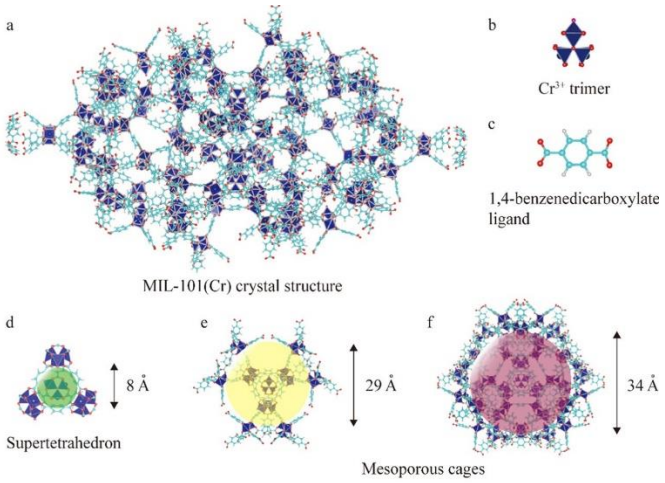

Figure 8.1 (a) 3D structure (b) Metal trimer (c) ligand linker (d) supertetrahedron (8 Å) (e) medium cage (f) large cage (34 Å), [135]

An attractive aspect of MIL-101-Cr, like any other MOF structure, is the ease of structural tuning and modification [10], [152]–[156]. One route to modifying MIL-101-Cr ($X=OH^-$, F^-) entails replacing the precursor terephthalic acid with ortho-substituted terephthalic acid as ligand linker [133], [157]–[160]. Alternatively, either the pristine MOF or its functionalized form can be subjected to further reactions. This additional treatment, which is known as post-synthetic modification (PSM), can sometimes involve multiple reactions in tandem [74] and [161].

Nitro functionalization of the linker in MIL-101-Cr has been reported to enhance air separation [134]. The increased N_2 selectivity of the modified structure has been attributed to enhanced electron-withdrawal ability of the nitro group to tune Lewis acidity of the exposed Cr atom during their interaction with the π^* orbitals of the N_2 molecules. Other choices of functional groups, that were studied, include amino, methyl and halogens. The

inductive (field) and resonance (mesomeric) effects of these substituents on the benzene ring as electron donors or electron withdrawers indirectly affect the Lewis acid strength of the CUS metals [162]. This advantageous contribution is somewhat offset by the decrease in available specific surface area and total pore volume due to the steric hindrance effect caused by the sheer bulk of the functional groups. When MIL-101-Cr was functionalized to study water adsorption, it was observed that NH_2 groups render the structure more hydrophilic and therefore move the inflection point of the type V isotherm to lower relative pressure values whereas NO_2, which are relatively hydrophobic, has no such effect [133]. Grafting the CUS chromium through replacing the coordinated water molecules with other ligands has also been reported [133], [159][163]–[165]. Finally, the effect of the nature of the metal cluster anion has been studied for MIL-101-Cr [158] and [146]. MIL-101-Cr ($X=Cl^-$) was found to possess higher N_2O capacity and N_2O/N_2 selectivity for trace N_2O removal in comparison to MIL-101-Cr ($X=F^-$) [166].

In our previous study [167], we used molecular simulation verified by experiment to examine three MOF structures MIL-101-Cr ($X=F^-$, OH^-), MIL-100-Al ($X=F^-$, OH^-), and MOF-177-Zn for their equilibrium adsorption capacity and heat of adsorption towards inhalation anesthetic agents, sevoflurane and desflurane. These MOFs possess two, one and zero CUS per metal node, respectively. It was shown that MIL-101-Cr is currently the best verified MOF candidate for IAA adsorption.

In this study, we combined molecular simulation with experimental synthesis/characterization to predict and verify how the IAA adsorption capacity of MIL-

101-Cr ($X=F^-$, OH^-) can further be improved by assessing the following paths: (1) altering the metal-cluster environment by anion exchange of fluorine with chlorine ions, (2) functionalization of the MIL-101-Cr ($X=Cl^-$) linkers with amino and nitro groups, and (3) substituting coordinated water molecules of MIL-101-Cr ($X=F^-$, OH^-) with NH_3 molecules. Finally, an overall ranking of the MOFs was performed.

8.2. Materials and Methodology

Two approaches were adopted for adsorption isotherm determinations, which included molecular simulation, as well as the commercial volumetric/manometric adsorption techniques.

8.2.1. Adsorbent materials and synthesis

Sevoflurane (98%) and desflurane (95%) were obtained from Blue-Zone Technologies Ltd. (Toronto, ON, Canada).

MIL-101-Cr ($X=F^-$, OH^-) was prepared by Dr. Caputo research group at the University of Naples Federico II, Italy.

NO_2-MIL-101-Cr ($X=Cl^-$) was synthesized at Dr. Kaskel research group at TU Dresden using $CrCl_3$ and 2-nitro-terphthalic acid as precursors, respectively and hydrochloric acid (HCl) as modulating agent. NH_2-MIL-101-Cr ($X=Cl^-$) was synthesized by Dr. Kaskel research group at TU Dresden by reduction of NO_2-MIL-101-Cr ($X=Cl^-$) with $SnCl_2$ as the reducing agent.

NH_2-MIL-101-Cr ($X=Cl^-$) was synthesized by Dr. Kaskel research group at TU Dresden by reduction of NO_2-MIL-101-Cr ($X=Cl^-$) with $SnCl_2$ as the reducing agent.

MIL-101-Cr ($X=F^-$, OH^-)@NH_3 was prepared at UNB Department of Chemistry, by Dr Mason C. Lawrence, a Postdoctoral Fellow on the Blight Research team

A portion of MIL-101-Cr ($X=F^-$, OH^-) was first dried to remove coordinated water molecules of the saturated coordinated site (2 for MIL-101-Cr) followed by using an aqueous solution of ammonia to introduce NH_3 molecules as coordinated ligands to the CUS formed during drying. Comparison of elemental analysis for carbon and nitrogen for the initial and final samples showed that the substitution was successful at a rate of 1.5 coordinated NH_3 per trimeric metal cluster of the MOF. Subsequent PXRD data and SEM images confirmed preservation of the crystal structure of the resulting compound. See Section I of Supplementary Information.

MIL-101-Cr ($X=Cl^-$, OH^-) was prepared at UNB Department of Chemistry, Professor Barry Blight's research group by anion exchange of the fluorine anions with chlorine using a 1N aqueous solution of NaCl. SEM images confirmed the preservation of the crystal structure and EDS mapping confirmed the presence of chlorine in the new structure. See Section I of Supplementary Information.

Physicochemical properties of MIL-101-Cr ($X=F^-$, OH^-), MIL-101-Cr ($X=Cl^-$, OH^-) and MIL-101-Cr ($X=F^-$, OH^-)@NH_3 were determined from N_2 adsorption at 77K using our BELSORP-max instrument (BEL Japan, Inc.). The samples were pretreated by degassing at 383K for 10 hours. The specific surface area, the total pore volume, and the pore size distribution were evaluated using the data analysis software BELMaster V6.1.0.4. For

NO_2-MIL-101-Cr ($X=Cl^-$) and NH_2-MIL-101-Cr ($X=Cl^-$, OH^-) samples, N_2 physisorption at 77K was performed at TU Dresden. Powder X-ray diffraction (PXRD) patterns for MIL-101-Cr samples were obtained using a Bruker D8 Advance spectrometer with a 2.2 kW Cu X-ray tube source, maintained at an operating current of 40 kV and 25 mA. Samples were scanned in the range of 5-80^o 2θ. Powder X-ray diffraction (PXRD) patterns for NO_2-MIL-101-Cr ($X=Cl^-$) and NH_2-MIL-101-Cr ($X=Cl^-$) samples were obtained at TU Dresden. TGA/DSC measurements for MIL-101-Cr ($X=Cl^-$, OH^-) and MIL-101-Cr ($X=F^-$, OH^-)@NH_3 and were performed using our SDT-Q600 (TA Instruments, USA). The samples were heated from room temperature to 600 °C at a ramp rate of 5 °C/min while being purged with nitrogen at a flow rate of 100 ml/min. Thermogravimetric analyses for the NO_2-MIL-101-Cr ($X=Cl^-$) and NH_2-MIL-101-Cr ($X=Cl^-$) samples were performed at TU Dresden. A Perkin Spectrum 100 FT-IR spectroscope with Diffuse Reflectance sample holder (DRIFTS) was used to record the middle-IR spectra for MIL-101-Cr ($X=F^-$), MIL-101-Cr ($X=Cl^-$), and MIL-101-Cr ($X=F^-$) @NH_3. FTIR spectra for NO_2-MIL-101-Cr ($X=Cl^-$) and NH_2-MIL-101-Cr ($X=Cl^-$) samples were provided by TU Dresden. Characterization data and synthesis procedure for all of the samples are included in Sections I and IV of Supplementary Information, respectively.

8.2.2. Molecular structure modeling and simulation of the isotherms

For adsorption simulation, the adsorbent, adsorbate, and their interactions were modeled. We used the CIF file for MIL-101-Cr-primitive first published in [24] and available in RASPA archive of structures [123]. The CIF for NH_2-MIL-101-Cr ($X=Cl^-$), and NO_2-MIL-101-Cr ($X=Cl^-$) were prepared using PoreModeMat.jl [168] and MOFUN [104] tools. For

Cr-MOF-2@NH_3, we used ToBaCCo-3.0 [169] and BOVIA Materials Studio software[76]. To prepare CIF file for MIL-101-Cr ($X=Cl^-$), the F atoms in the MIL-101-Cr-*primitive* were manually replaced by Cl and the partial atom charges were subsequently calculated using the Charge Equilibration method implemented in RASPA [123]. General simulation details are as described in our previous paper [167]and additional information on simulation specific to this study can be found in Section V of Supplementary Information.

8.2.3. Experimental adsorption isotherm measurement

The simulation results were consequently validated by comparison with experimental isotherms obtained from volumetric-adsorption measurements using our BELSORP-Max (Bell, Japan). Prior to measurement, each MOF sample was regenerated under a high vacuum at 110°C for 10 hours. Fresh liquid IAA were poured into small bottles (about 30 ml) serving as adsorbate reservoir and connected to the measurement manifold. The liquid in the bottle was degassed through a semi-automatic procedure which involved freezing the liquid IAA, followed by exposing the frozen IAA to vacuum for about 5 minutes before stopping the vacuum and melting of IAA by immersing the bottle in a beaker containing warm water. This cycle was performed at least three times to make sure no dissolved air exists in the liquid IAA reservoir. The IAA adsorption isotherms were measured at 298K for sevoflurane and 288K for desflurane, respectively. The dead volume of the adsorbent sample cell was also measured using helium gas automatically. The adsorption isotherm measurement consisted of dosing certain amount of evaporated IAA into the pre-evacuated sample cell before closing the admittance valve and waiting until equilibrium is achieved.

Equilibrium was defined when the pressure inside the sample cell changed within 0.3% for 300 seconds. Once the equilibrium was achieved, the admittance valve was reopened to allow more adsorbate into the cell needed to achieve the next equilibrium point on the isotherm. The pressure change during each step was translated into the amount adsorbed in terms of STP volume, number of moles or number of mill grams adsorbed. Once the adsorption isotherm steps were finished, the sample cell holder containing the adsorbent is detached from the machine and is weighed using a microbalance and entered into the measurement software which reports the isotherm as moles of adsorbate per gram of adsorbent *vs* relative pressure of the adsorbate. See Figure 8.6S in the Supplementary Information.

8.3. Results and Discussion

Some degree of discrepancy between simulation and experimental data is often expected. Reasons may be due to a deviation of adsorbate molecule from ideally modeled structure and/or the adsorbent material from perfect crystallinity. Some degree of structural defects can be expected especially on the highly active sites to be prone to deviating from the expected theory. Shaping processes can also generate new crystalline phases and/or result in partial collapse of the original structure [143]. Moreover, amorphous phases might be formed as a result of residual solvents inside the cages [144]. Incomplete activation could be another cause of discrepancy. Finally, the random nature of functionalization during modifications and adsorption-induced structural deformation should also be considered.

8.3.1. Sevoflurane adsorption isotherms

Figures 8.2a-d compare simulation results using RASPA with the experimental data obtained by Belsorp for the adsorption of sevoflurane on all studied MOF samples at 298K. Satisfactory agreement is observed especially at lower partial pressures, which is significant as dilute solutions are more often used in practical applications.

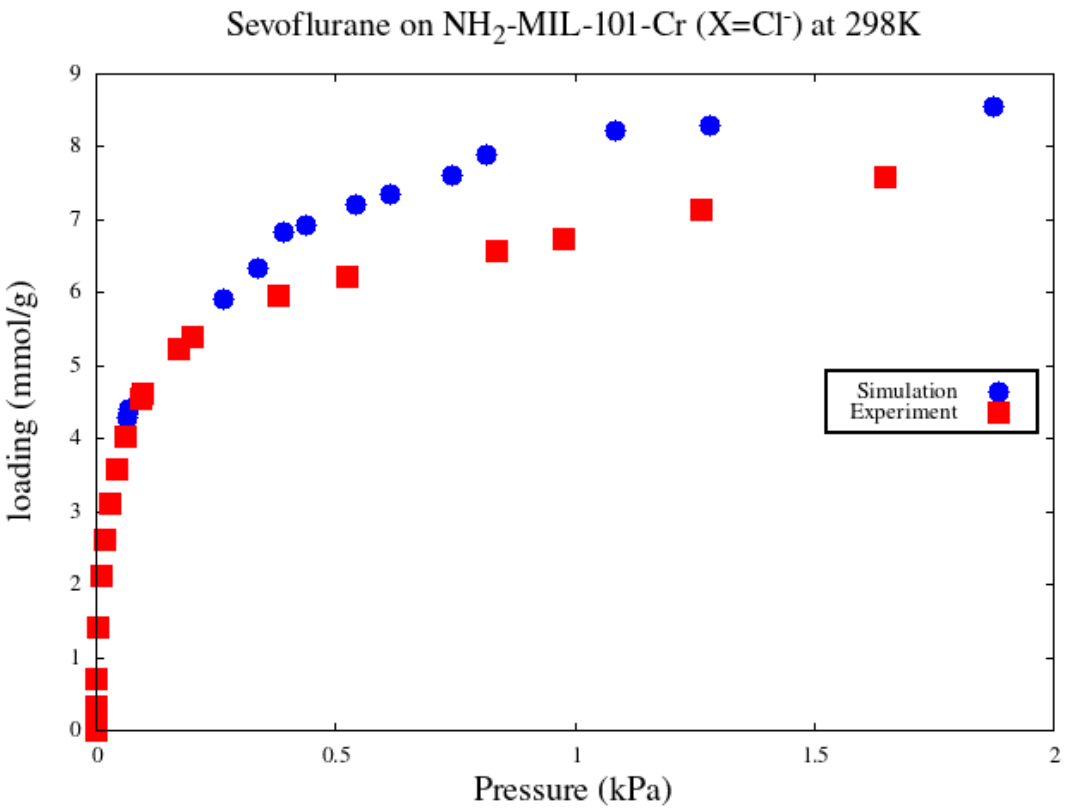

Figure 8.2a RASPA isotherm simulation results (blue solid spheres) for sevoflurane adsorption on NH_2-MIL-101-Cr ($X=Cl^-$) at 298K in comparison with experimental results (red solid squares) obtained from BELSORP instrument

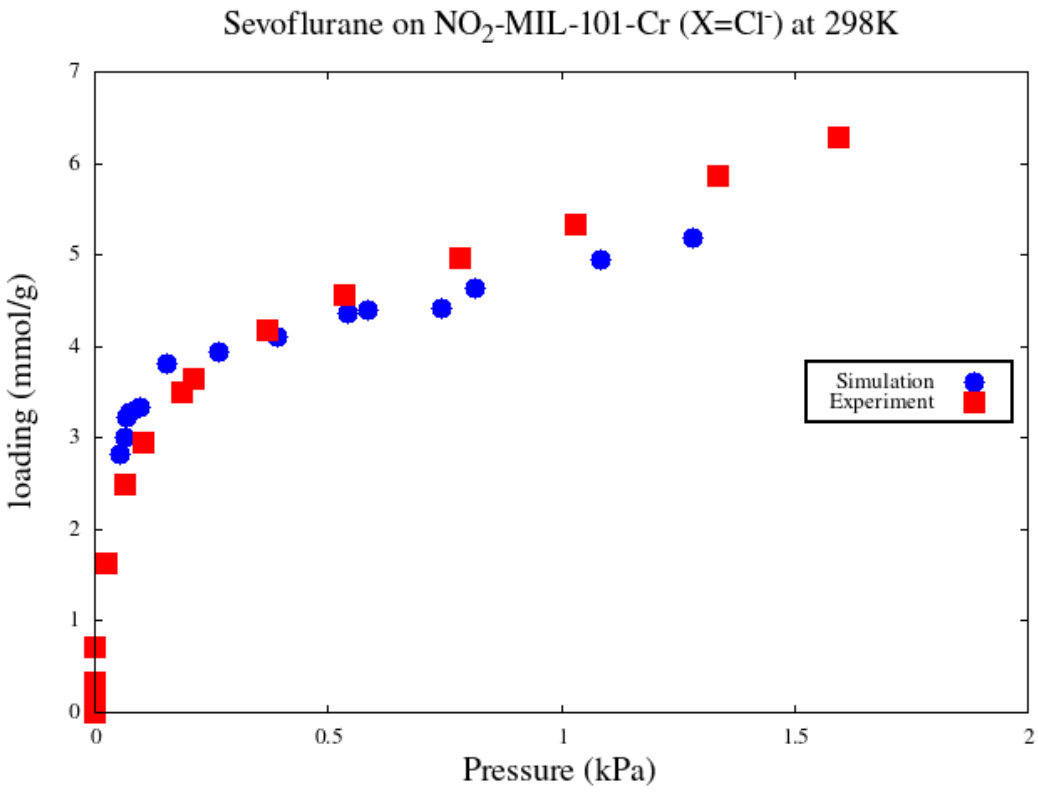

Figure 8.2b RASPA isotherm simulation results (blue solid spheres) for sevoflurane adsorption on NO_2-MIL-101-Cr ($X=Cl^-$) at 298K in comparison with experimental results (red solid squares) obtained from BELSORP instrument

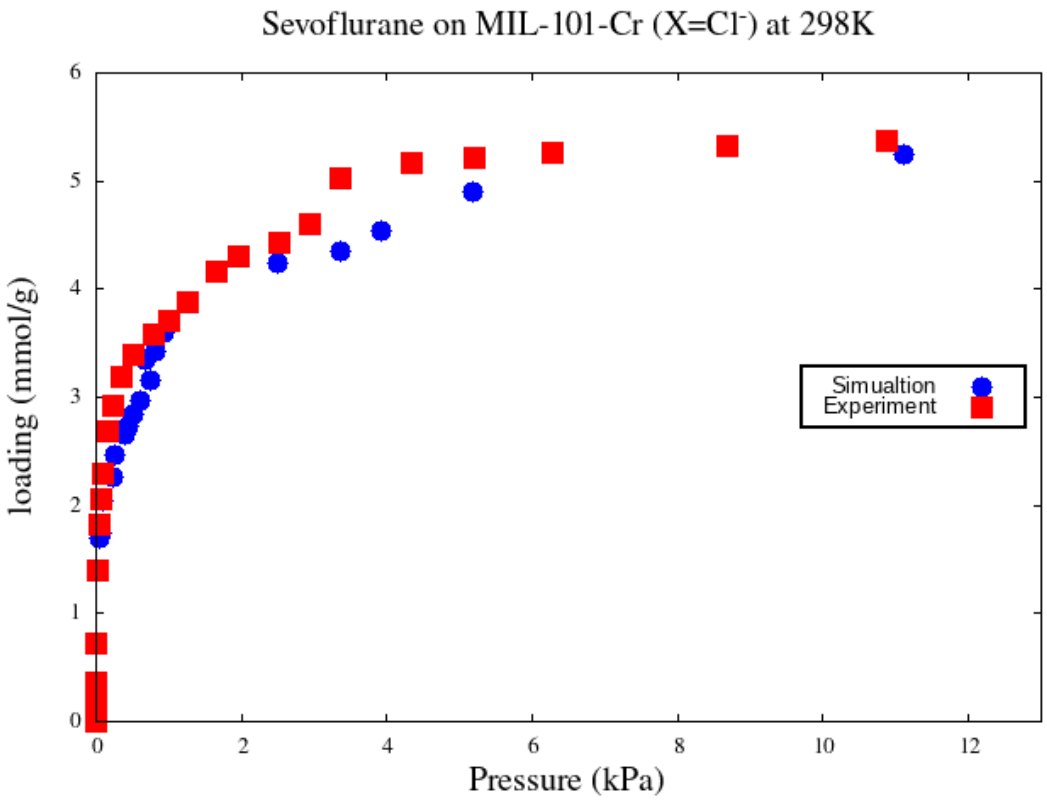

Figure 8.2c RASPA isotherm simulation results (blue solid spheres) for sevoflurane adsorption on MIL-101-Cr (X=Cl^-) at 298K in comparison with experimental results (red solid squares) obtained from BELSORP

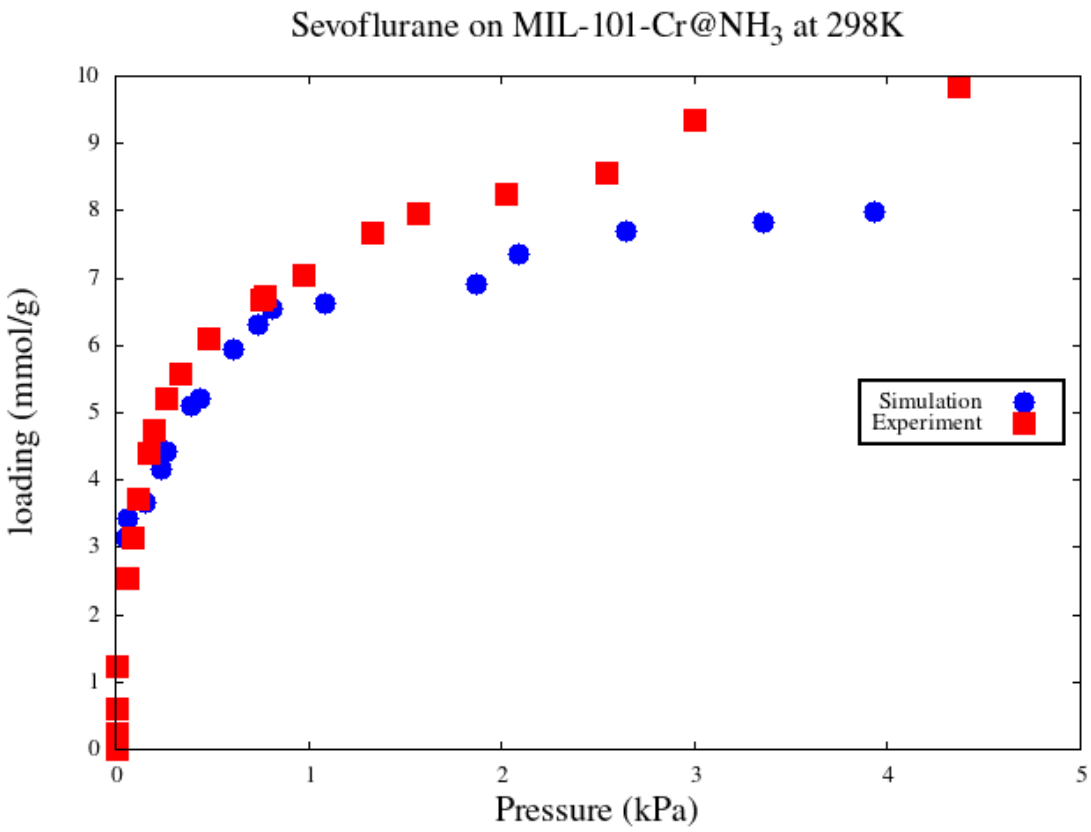

Figure 8.2d RASPA simulation results (blue solid spheres) for sevoflurane adsorption on MIL-101-Cr@NH_3 at 298K in comparison with corresponding experimental results (red solid squares) obtained from BELSORP

Due to the different nature of structural modifications, the comparison of the adsorption isotherms is discussed under two categories, i.e., metal-cluster ligand/anion modification and linker function substitution presented in subsections 8.3.1.1 and 8.3.1.2, respectively.

8.3.1.1. Effect of metal-cluster modification on sevoflurane uptake

Experimental and simulation data as summarized in Figure 8.3 show that anion exchange of fluorine in the metal cluster with chlorine has little to no effect on the uptake of sevoflurane. The slight decrease for Cl replacement falls within the measurement error and is therefore insignificant. On the other hand, exchange of coordinated water molecules with ammonia at the CUS sites shows an almost 100% increase in uptake. CUS in MOFs are known to be Lewis acid sites and substitution with NH_3 creates more favorable adsorption sites for sevoflurane uptake.

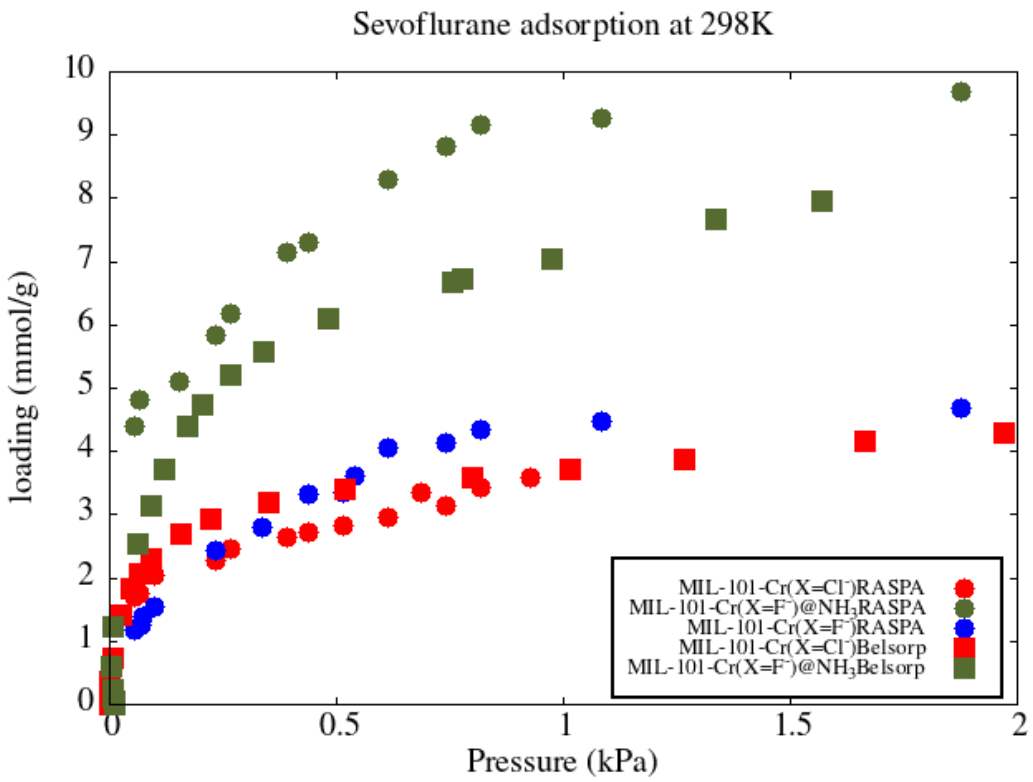

Figure 8.3 RASPA isotherm simulation results for adsorption of sevoflurane on MIL-101-Cr (X=Cl-), MIL-101-Cr (X=F-) and MIL-101-Cr (X=F-)@NH^3 at 298 K compared with corresponding experimental results obtained from BELSORP instrument

8.3.1.2. Effect of linker modification on sevoflurane uptake

Figure 8.4 examines the effect of linker functionalization. For the series MIL-101-Cr (X=Cl^-), NO_2-MIL-101-Cr (X=Cl^-), and NH_2-MIL-101-Cr (X=Cl^-), it is observed that despite the expected steric hindrance due to the bulk of the functional groups, both NO_2 and NH_2 derivatives outperform the unsubstituted form. This can be due to the fact that we are dealing with lower adsorption coverage and therefore, the adsorbate-adsorbent interactions are more significant than specific area or total pore volume which become

significant at medium to high adsorption coverage, where adsorbate-adsorbate interactions prevail [25].

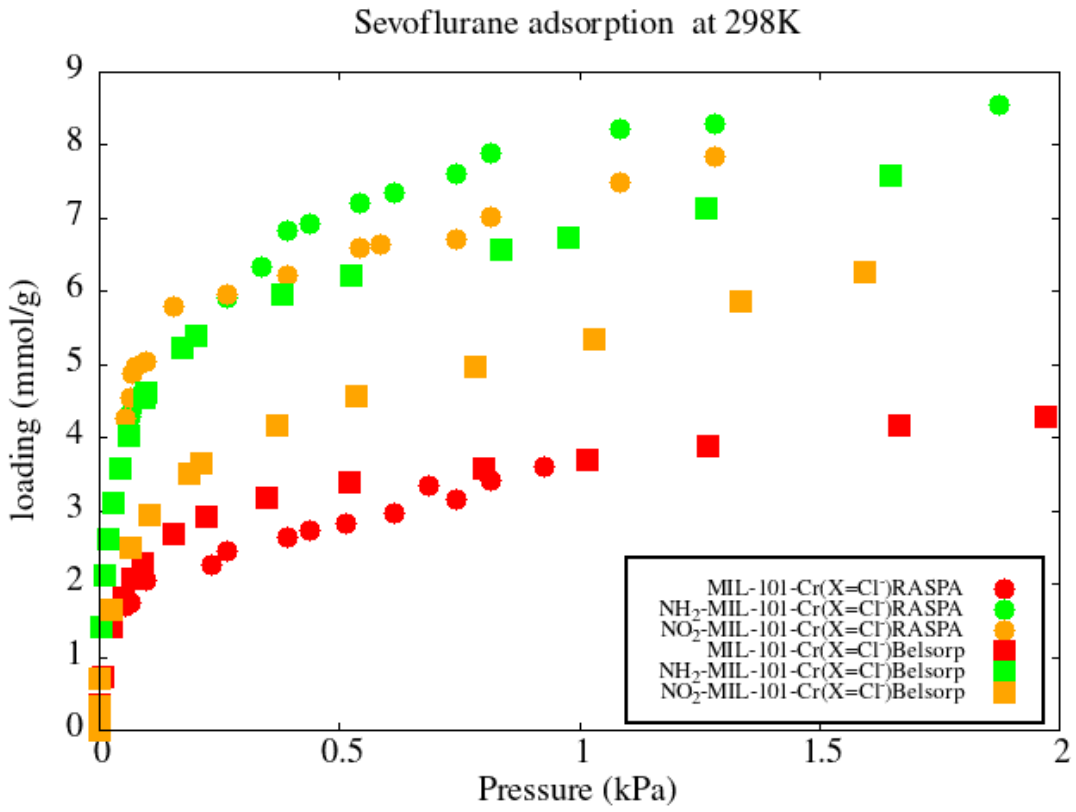

Figure 8.4 RASPA simulation results for adsorption of sevoflurane on MIL-101-Cr (X=Cl^-), NO_2-MIL-101-Cr (X=Cl^-) and NH_2-MIL-101-Cr (X=Cl^-) at 298K compared with corresponding experimental results using BELSORP

The effect of NO_2 and NH_2 groups on benzene ring has traditionally been explained in terms of the inductive and resonance effects [32]. Amine group can play two roles depending on the situation. When the atom of nitrogen participates through its free electron pair in resonance, the amine group plays the role of a donating group by conjugation; its inductive withdrawing effect still exists but is weaker and masked by the first effect. When amine groups cannot participate in conjugation through resonance, the amine group plays

the role of inductive electron-withdrawer group, due to the higher electronegativity of nitrogen atom compared to carbon atom. NO_2 functional group has a lower inducive effect than NH_2 functional group.

8.3.2. Desflurane adsorption isotherms

Figures 8.5a-d compare the RASPA isotherm simulation results with the experimental data obtained by Belsorp for the adsorption of desflurane on all MOFs. As the normal boiling point of desflurane is about 295K, the lower temperature of 288K was chosen as a safer point. Desflurane has a smaller diameter (5.4 Å) than SF (7.1 Å) and therefore more desflurane molecules are expected to fill the pore cages at medium to high coverages than sevoflurane. However, at lower adsorption coverages, adsorbent-adsorbate interactions become more important, resulting in weaker interaction and therefore lower adsorption capacity for desflurane as it is smaller, less branched, and less polar molecule than sevoflurane.

As was the case with sevoflurane adsorption isotherms, due to the different nature of structural modifications, the comparison of the desflurane adsorption isotherms is discussed under two categories, i.e., metal-cluster ligand/anion modification and linker function substitution in subsections 8.3.2.1 and 8.3.2.2, respectively.

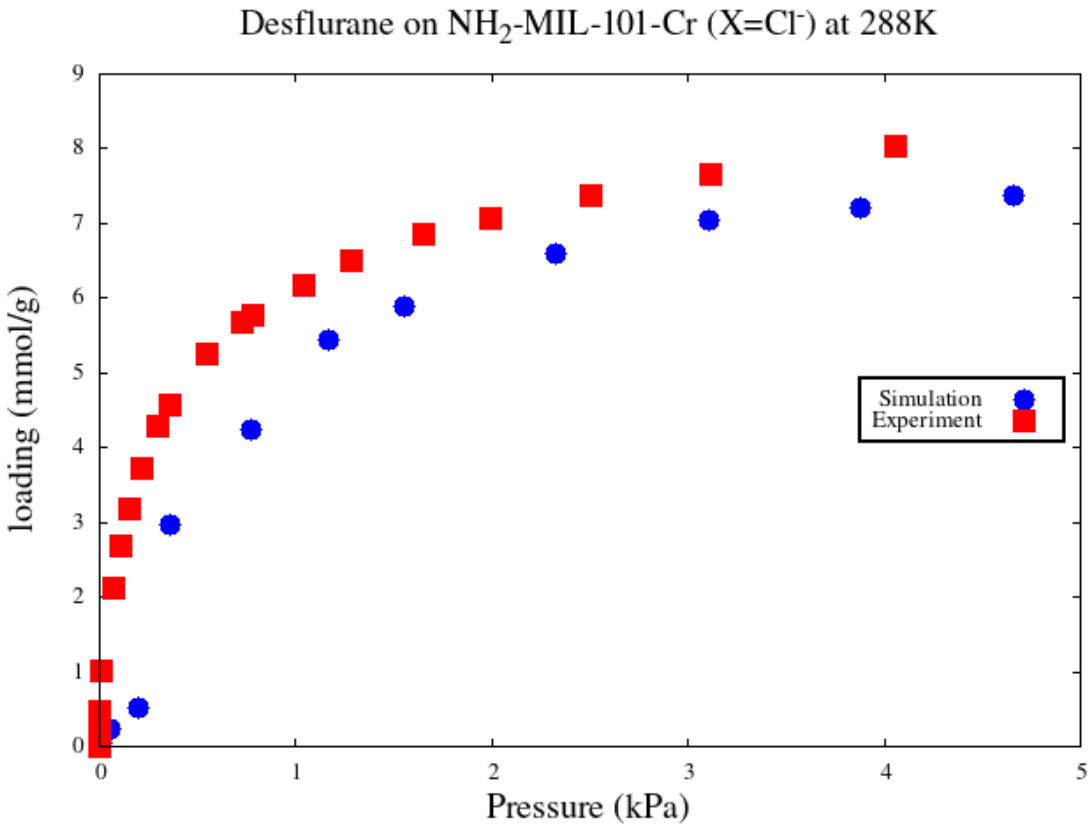

Figure 8.5a RASPA isotherm simulation results (blue solid spheres) for desflurane adsorption on NH_2-MIL-101-Cr ($X=Cl^-$) at 288K in comparison with experimental results (red solid squares) using BELSORP

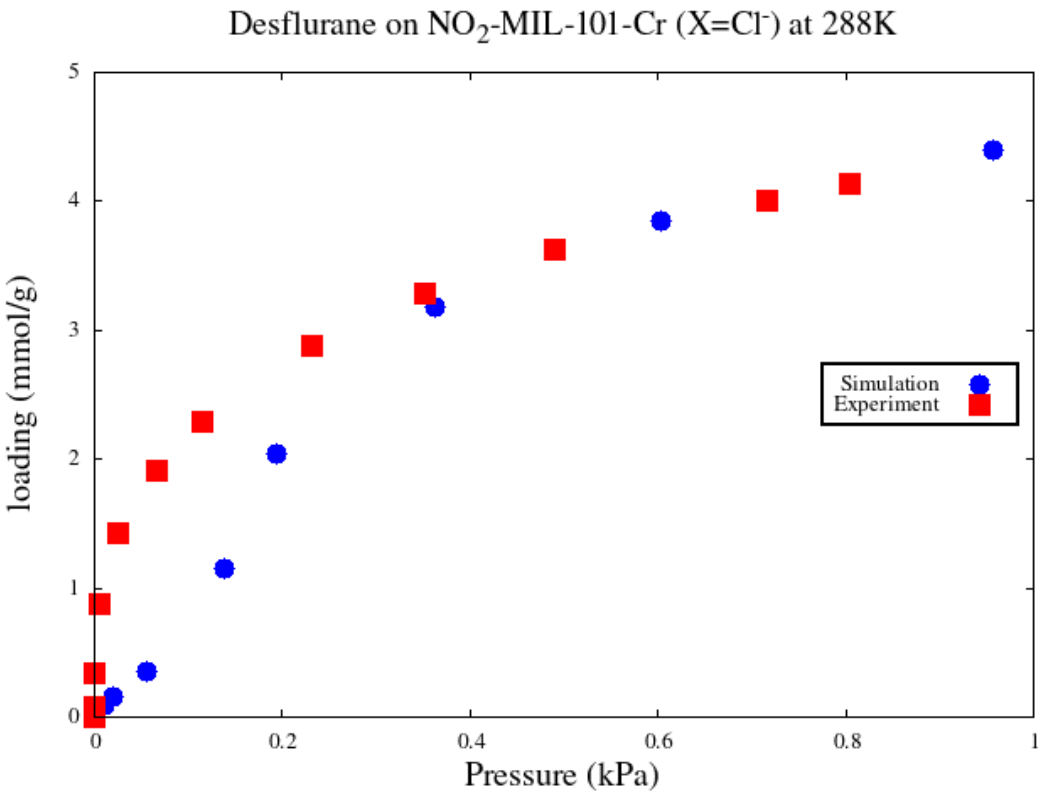

Figure 8.5b RASPA isotherm simulation results (blue solid spheres) for desflurane adsorption on NO_2-MIL-101-Cr ($X=Cl^-$) at 288K compared with corresponding experimental results (red solid squares) obtained from BELSORP instrument

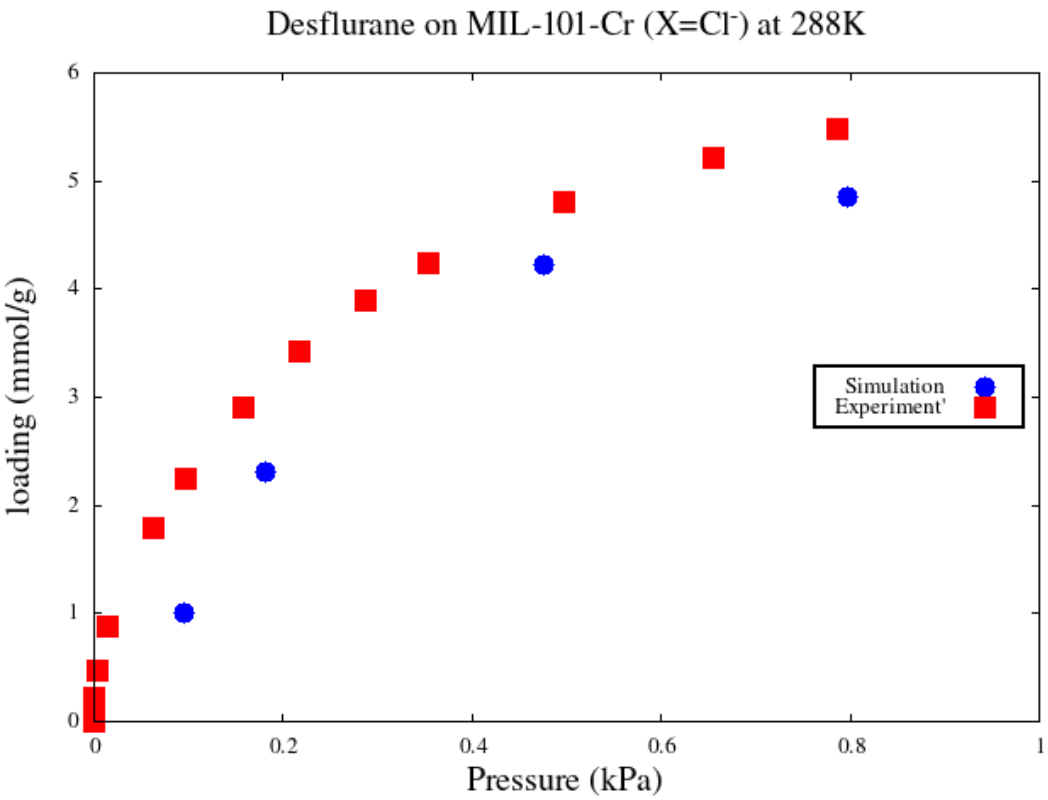

Figure 8.5c RASPA isotherm simulation results (blue solid spheres) for desflurane adsorption of on MIL-101-Cr (X=Cl^-) at 288K compared with corresponding experimental results (red solid squares) obtained from BELSORP instrument

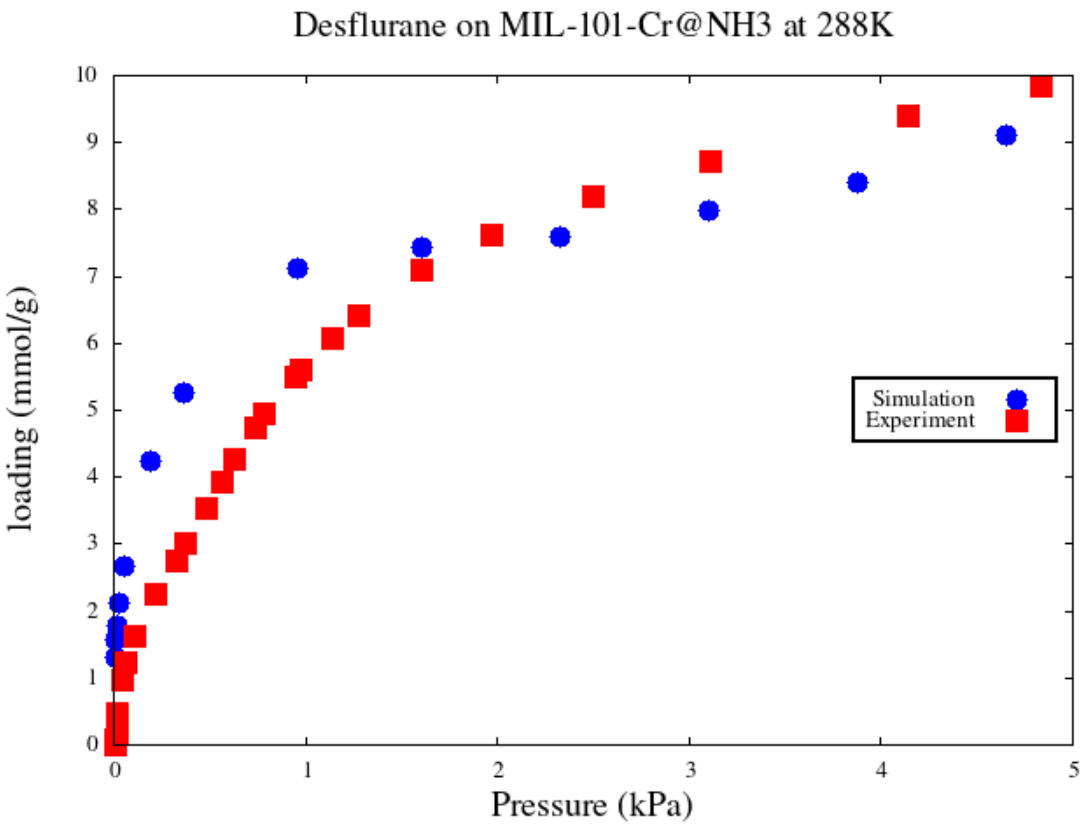

Figure 8.5d RASPA isotherm simulation results (blue solid spheres) for desflurane adsorption on MIL-101-Cr@NH_3 at 288K compared with corresponding experimental results (red solid squares) obtained from BELSORP instrument

8.3.2.1. Effect of Metal-cluster modification on desflurane uptake

Figure 8.6 compares experimental data from BELSORP and simulation results using RASPA. It shows that anion exchange of fluorine in the metal cluster with chlorine has little to no effect on desflurane uptake as was the case with sevoflurane. However, upon replacing coordinated water molecule at the CUS sites with ammonia the uptake of desflurane is enhanced significantly. An interesting feature of the experimental results in Figure 8.8S is that isotherms cross each other at around 1 kPa affecting the ranking of the adsorbents. As reported earlier in our publication [25], this can be explained in terms of the existence and concentration-dependence of different adsorption mechanisms for IAA on the MOFs where solid-fluid interactions prevail at lower partial pressures (coverages) but the adsorbate-adsorbate interactions prevail at medium to high coverages, where BET surface area and total pore volumes are determining factors.

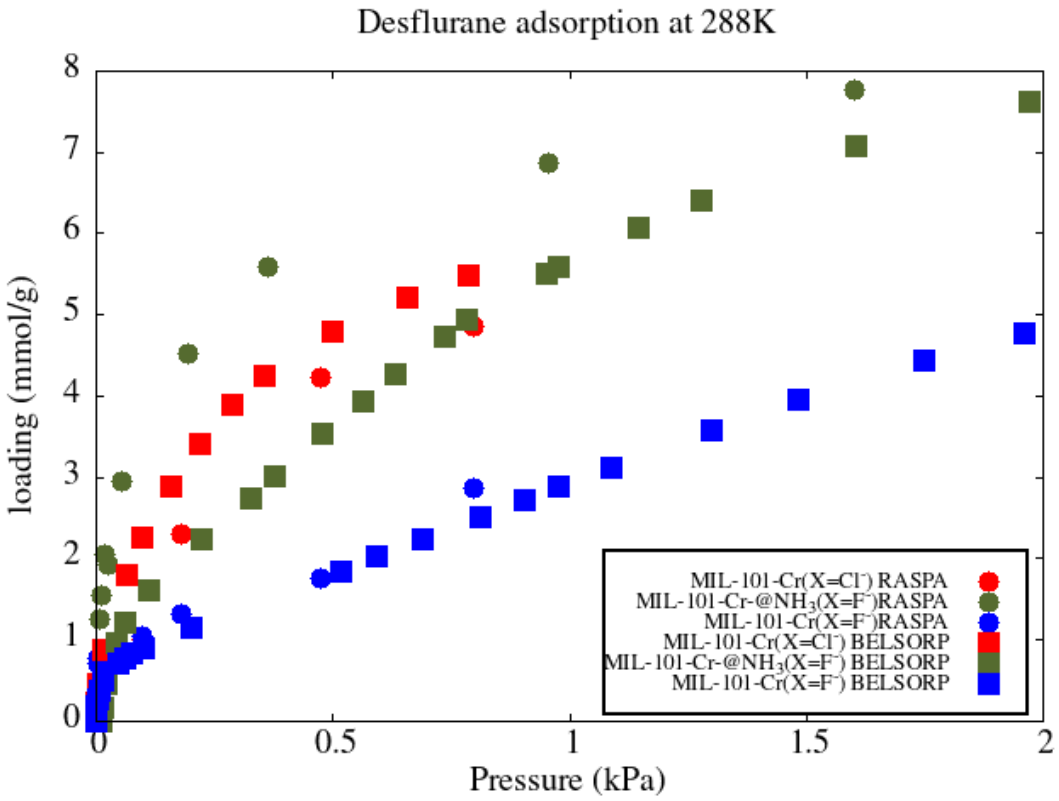

Figure 8.6 RASPA isotherm simulation results for desflurane adsorption on MIL-101-Cr (X=Cl^-), MIL-101-Cr (X=F^-) and MIL-101-Cr (X=F^-)@NH_3 at 288K compared with corresponding experimental results obtained from BELSORP instrument

8.3.2.2. Effect of linker modification on desflurane uptake

The effect of linker functionalization on desflurane uptake is shown in Figure 8.7. For the series MIL-101-Cr ($X=Cl^-$), NO_2-MIL-101-Cr ($X=Cl^-$), and NH_2-MIL-101-Cr ($X=Cl^-$), both NO_2 and NH_2 derivatives outperform the unsubstituted form.

The effect of NO_2 and NH_2 groups on benzene ring that has traditionally been explained in terms of the inductive and resonance effects [32] can play two roles depending on the conditions of exchange. When the atom of nitrogen in amine group participates through its free electron pair in resonance, the amine group plays the role of a donating group by conjugation; its inductive withdrawing effect still exists but is weaker and masked by the first effect. NO_2 functional group has a lower inductive effect than NH_2 functional group.

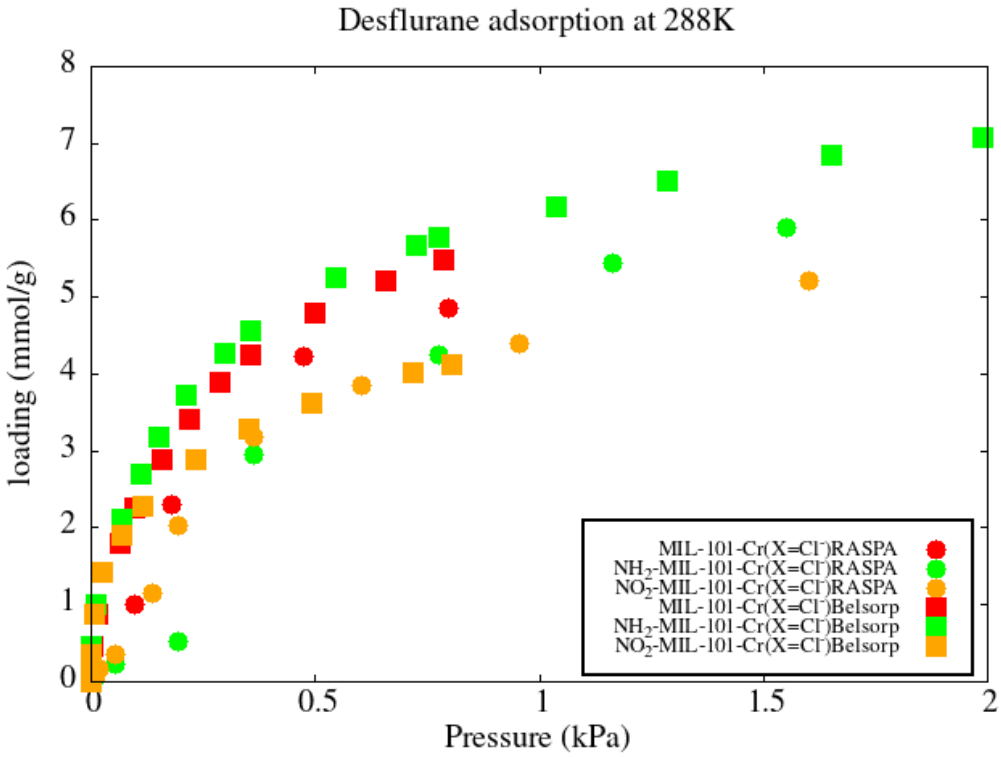

Figure 8.7 RASPA isotherm simulation results for desflurane adsorption of on MIL-101-Cr (X=Cl^-), NO_2-MIL-101-Cr (X=Cl^-) and NH_2-MIL-101-Cr (X=Cl^-) at 288K compared with corresponding experimental results obtained from BELSORP instrument

8.4. Comparison and ranking of the adsorbents

Figures 8.8 and 8.9 summarize the adsorption isotherms for all adsorbents for sevoflurane and desflurane, respectively. It is evident for sevoflurane that the capacity order is as follows:

NH_3@ MIL-101-Cr ($X=F^-$) > NH_2-MIL-101-Cr ($X=Cl^-$) > NO_2-MIL-101-Cr ($X=Cl^-$) > MIL-101-Cr ($X=F^-$) > MIL-101-Cr ($X=Cl^-$)

For desflurane the ranking is more challenging, and it depends on the choice of the partial pressure. At 1 kPa:

MIL-101-Cr ($X=Cl^-$) > MIL-101-Cr ($X=F^-$) > NH_3@ MIL-101-Cr ($X=F^-$) > MIL-101-Cr ($X=Cl^-$) > NO_2-MIL-101-Cr ($X=Cl^-$) > NH_2-MIL-101-Cr ($X=Cl^-$)

As hinted in subsection 8.2.1., the isotherms can cross each other at some partial pressures, affecting the overall ranking. Therefore, it is imperative to report the ranking based on the working adsorption conditions.

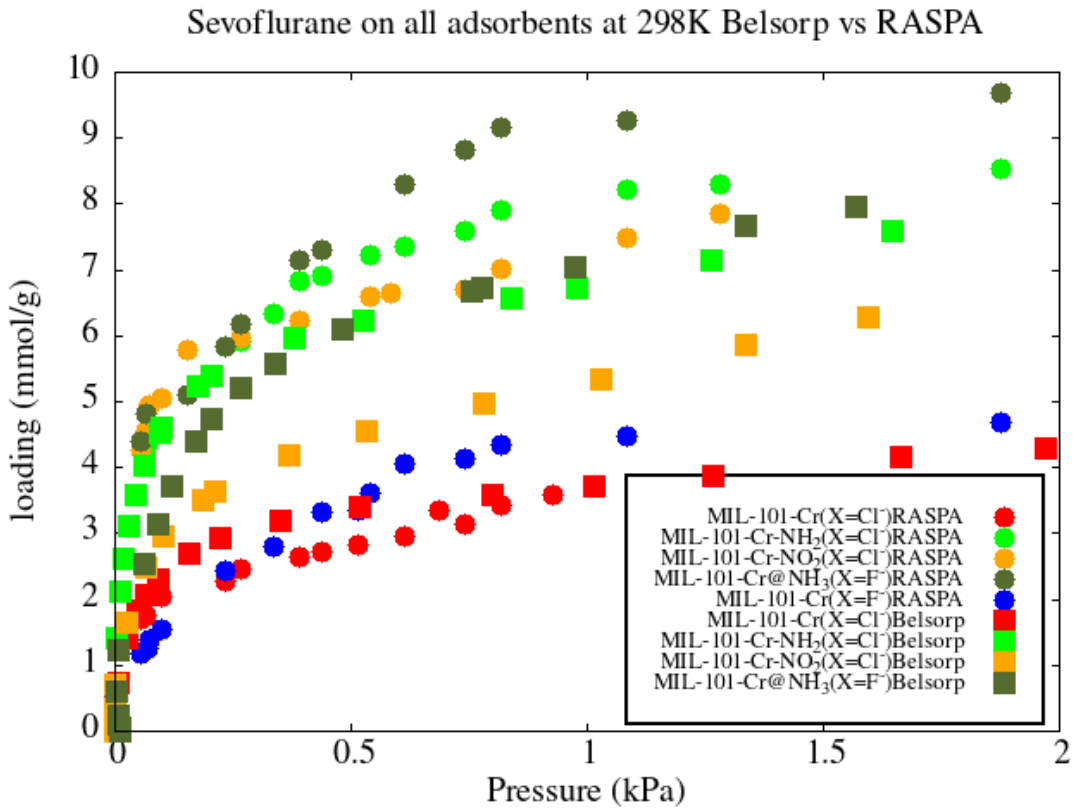

Figure 8.8 RASPA isotherm simulation results for sevoflurane adsorption on all adsorbents at 298K compared with corresponding experimental results obtained from BELSORP instrument

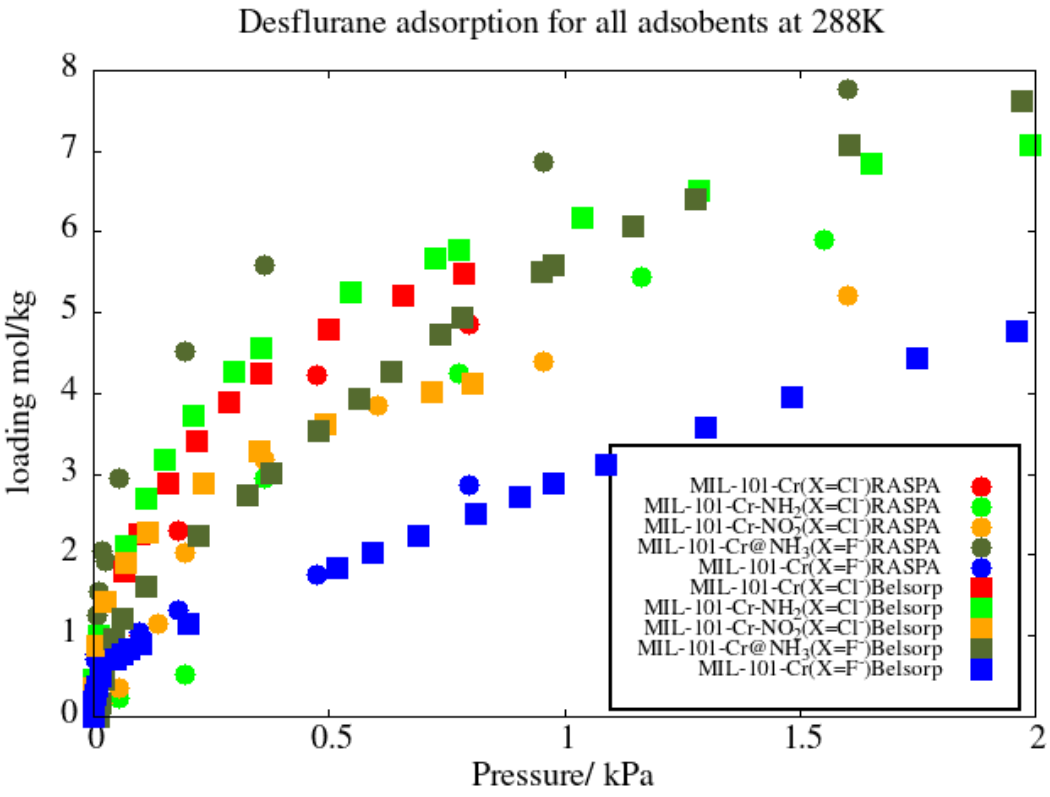

Figure 8.9 RASPA isotherm simulation results for desflurane adsorption on all adsorbents at 288K compared with corresponding experimental results obtained from BELSORP instrument

8.5. Conclusions

Several modifications to pristine MIL-101-Cr ($X=F^-$, OH^-) were performed and their capacity towards IAA molecules was assessed using volumetric experimental technique and molecular simulation. The results indicate that our previously successful molecular simulation approach [167] applies equally well for modified structures and can simplify the task of designing superior adsorbents and reduce the number of trials and errors during experimental modification and characterization procedures. Which is advantageous in terms of both time and expense. Our present work successfully introduced several new adsorbents for IAA, where grafting NH_3 to the metal cluster more than doubled the capacity towards sevoflurane but slightly decreased capacity towards desflurane. The latter observation hints at the potential of MIL-101-Cr ($X=F^-$, OH^-)@NH_3 to selectively remove sevoflurane from its binary mixture with desflurane.

8.6. Acknowledgment

The authors are grateful for the NSERC Discovery Grant. Our thanks go to the following for help with preparation and characterization of the samples: Dr. S. Kaskel and Dr. S. Hausdorf at TU Dresden for the synthesis and characterization of the NH_2-MIL-101-Cr ($X=Cl^-$) and NO_2-MIL-101-Cr ($X=Cl^-$) samples. Dr. Mason Lawrence at UNB Department for the synthesis of Cr-MOF-2@NH_3 and Cr-MOF-2-Cl samples, and Dr. N. Gargiulo for the synthesis of the MIL-101-Cr samples. Mr. S. Cogswell (UNB Biology Microanalysis and Microscopy) is thanked for SEM images, Dr. V. Reddy (UNB Earth Sciences) for PXRD spectra of MIL-101-Cr-F and SIN lab at UNB Department of Biology for elemental analysis of MIL-101-Cr-F and MIL-101-Cr@NH_3. This research was partially supported

by BELUGA (www.beluga.computecanada.ca) and the Digital Research Alliance of Canada (alliancecan.ca). We would like to thank Dr. S. Vassiliev at ACENET division of Compute Canada for assistance with installation of RASPA simulation

Chapter 9. Use of the rapid ZLC experimental technique for fast isotherm measurement of inhalation anesthetic agent vapors

9.1. Introduction

An adsorption isotherm describes adsorbate-adsorbent equilibrium at a given constant temperature. Several techniques have been developed for adsorption isotherm measurements [172]. In the following subsections, traditional methods will be described first, followed by the more rapid techniques [173]. Emphasis will be given to the rapid measurement technique called Zero-Length Column Chromatography (ZLC) which will be introduced and expanded in section 9.1.3.

9.2. Traditional techniques

The two most common traditional techniques for isotherm measurements are gravimetric and volumetric methods. They are briefly discussed in sections 9.2.1 and 9.2.2.

9.2.1. Gravimetric methods

This method is one of the oldest methods used for adsorption studies where changes in the weight of the adsorbent is monitored during adsorption and desorption scans. The measurement apparatus is often complicated because of the need to correct/compensate for several different effects including buoyancy.

Figure 9.1 shows an automatic gravimetric adsorption analyzer (IGA, Hidden Isochema) available in our laboratory. It consists of a sample holder hanging from a thin metal wire connected to arm of a very sensitive microbalance. A metal casing surrounds the sample

holder and the wire and is flanged to the manifold; thus, isolating the sample from the ambient disturbances such as air flow, pressure, temperature, and moisture conditions. The manifold is equipped with admittance and exhaust valves, and it is connected to the vacuum tubing which consists of a roughing pump and a turbo pump. Our instrument is capable of handling sample pressures of up to 20 bars. It can work in static mode to measure adsorption isotherms as well as in the dynamic mode for kinetic studies. There is a furnace for outgassing the sample and a water bath to keep the sample temperature constant during adsorption isotherm measurements. A dedicated software controls the operations of the instrument and provides real-time information of the sample condition including its weight change, temperature, and the equilibrium pressure.

Figure 9.1 Intelligent Gravimetric Analyzer (IGA) from Hiden Isochema, UK. It can be run in static or dynamic mode. In dynamic mode, it can handle mixing two gases from separate inlets.

9.2.2. Volumetric/manometric methods

These methods monitor pressure changes during uptake or release of adsorbate from the sample and convert them into the units of mass, STP volume or the number of moles of the adsorbate. Experimental setup is less complicated than those of gravimetric methods, but it is amenable to spurious effects that is handled in automatic systems. Examples of such effects are the dead volume and transpiration.

Figure 9.2 Belsorp Max volumetric adsorption instrument from BEL, Japan. It can measure both gas and vapor adsorption measurements. The liquid vapor reservoir is a bottle located near the sample holder ports.

Figure 9.2 shows our automatic volumetric adsorption analyzer (BEL, Belsorp Max**)**. It is capable of measuring adsorption of either permanent gas or liquid vapors up to their saturation pressures at the ambient pressure of 1 atm temperatures of up to 35°C. The liquid vapor reservoir consists of a bottle located near the sample holder ports and is connected to the system manifold using a pneumatic valve. It cannot handle gas mixtures, pressures above one atmosphere or temperatures higher than 35°C.

9.3. Rapid measurement techniques: Zero-Length Column Chromatography (ZLC)

Zero-Length Column Chromatography (ZLC) is another method for adsorption isotherm measurements. It was originally developed as a macroscopic technique for determination

of the intracrystalline diffusion phenomena in microporous crystals, such as zeolites [174]. The technique relies on a small sample size and fast detector response to eliminate concomitant mass and heat transfer effects such as bed and axial diffusion, allowing for the assumption of well-mixed conditions inside the sample cell. The technique comprises a brief adsorption (saturation) period followed by full desorption. It is the desorption that matters where its curve slope provides sufficient data for calculation of the diffusion constant using an appropriate mathematical model. The models are formulated based on the assumption of which diffusion mechanisms are dominant. Examples of these mechanisms are surface diffusion, pore-mouth diffusion and mesopores vs micropore diffusion. Using regression analysis one can then identify the best-fitting models and hence identify the most prominent diffusion mechanism(s) at play for a given sorbate(s)/sorbent system[175]. In this respect, ZLC technique, which is in principle a reverse-chromatography method, has proven to be a time-efficient and accurate alternative in comparison to its rival methodology such as volumetric and gravimetric measurements[176].

The original ZLC technique described above is essentially a transient measurement technique relying on high flow rates of sorbates in a continuous flow arrangement. However, the theory of ZLC allows for smaller flow rates, too. In this case, the outlet flow concentration(s) of the sorbate(s) is (are) essentially in thermodynamic equilibrium with their adsorbed amount in the sample. This way equilibrium ZLC can be used for studying equilibrium phenomena i.e. measurement of adsorption isotherms. Equilibrium ZLC has already been attempted for adsorption of single component and binary mixture of hydrocarbon sorbates on zeolites[177][178]. It has also found application for fast-screening

of adsorbents for CO_2 capture applications[179]. It has also been used for adsorption water vapor which is known to exhibit adsorption hysteresis [180]. This is the only example of using ZLC technique to measure adsorption isotherm of liquid vapors, so far.

9.4. Use of ZLC for fast screening of adsorbents: permanent gases on zeolites and IAA vapors on MOFs

Zero-Length Column Chromatography (ZLC) was first introduced in 1988 by Eić and Ruthven as a macroscopic technique to measure intracrystalline diffusivity of hydrocarbon vapors inside zeolites [174]. It has found multiple applications which includes equilibrium regimes of operation in order to obtain adsorption isotherms for permanent gases and liquid vapors [9]. Here, we briefly describe the theory of ZLC for adsorption.

ZLC is a reverse chromatographic technique (based on desorption rather than adsorption), originally developed for kinetic studies[174][181]**.** It employs a very thin layer of sample, resulting in negligible axial dispersion, bed effects ,and heat transfer effects. A single layer of pellets/powder is exposed to adsorbate mixed in a carrier gas and then the sample holder cell is purged with pure carrier gas of the same flow rate. Assuming perfect mixing, we can write the differential mass balance for desorption inside the sample cell as in Equation (9.1).

Differential mass balance due to desorption can be expressed as:

$$V_s \frac{d\bar{q}}{dt} + V_g \frac{dc}{dt} + Fc = 0 \qquad (9.1)$$

V_g = gas hold-up volume (ml)

V_s = solid hold-up volume (ml)

$\bar{q}$ = Average loading inside the adsorbent particle (mmol/g)

F = Flow rate of the gas (ml/min)

c = adsorbate concentration during desorption (mmol/ml)

In order to get to the equilibrium-controlled regime, low purge flow rate has to be applied[177].

At equilibrium, Eqn. (9.1) can be rewritten as:

$$FC\frac{y}{1-y} = -V_s\frac{dq^*}{dt} - V_gC\frac{dy}{dt} \qquad (9.2)$$

F = Flow rate of the carrier gas (ml min^{-1})

y = molar fraction of the adsorbate in the gas phase

q^*=equilibrium loading inside the adsorbent particle (mmol/g)

C = total gas concentration (density) (mmol/ml)

Integrating Equation (9.2) yields:

$$q^* = \left(\int_0^{\infty}\frac{y}{1-y}d\left(\frac{F_ct}{V_s}\right) - \int_0^{t}\frac{y}{1-y}d\left(\frac{F_ct}{V_s}\right) - \frac{V_g}{V_s}y\right)C \qquad (9.3)$$

The first term on the R.H.S. of Equation 9.3 gives the saturation (total) capacity (q^* at c_o corresponding to time of desorption from t=0 to t=t∞)) and the second term is the amount desorbed from t_0 to t_1 .The sum of all three terms gives isotherm curve points.

As it is also summarized graphically in Figure 9.3, Equation 9.3 indicates that by plotting c/c_0 (or y/y_0) from $t = 0$ to $t = \infty$, one can calculate adsorption capacities at different concentrations, by selecting the area under the curve and generating isotherm points.

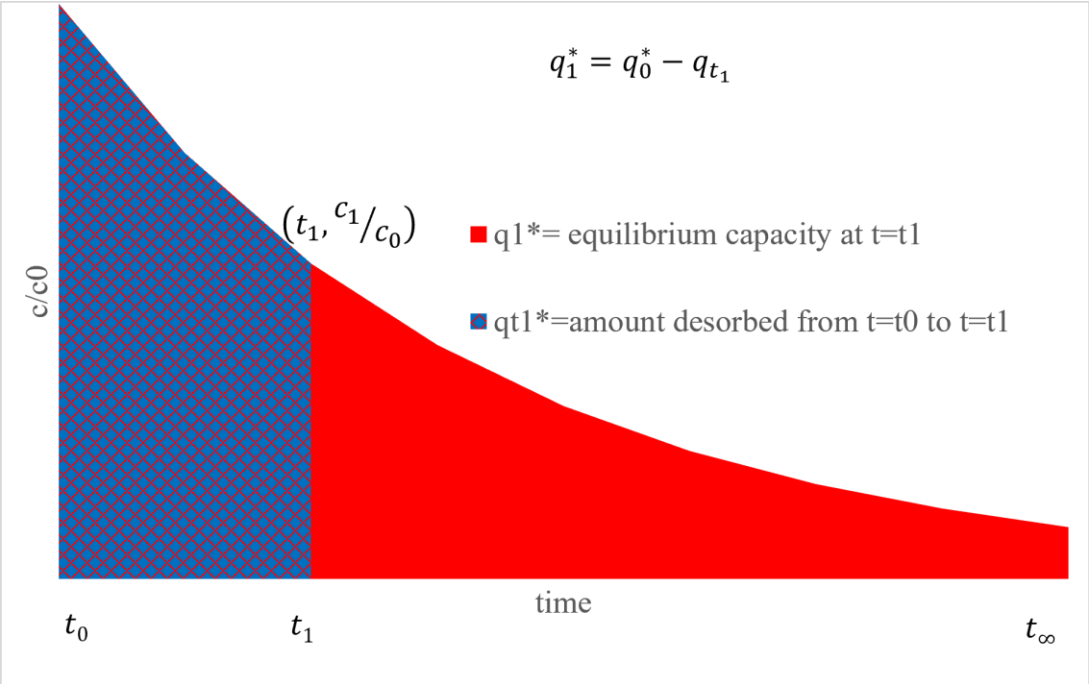

Figure 9.3 Graphical representation of Equation 9.3. The red area represents equilibrium capacity at t_1 , $\boldsymbol{q_1^*}$, whereas the double-hashed part represents the capacity between t=0 and t=t_1, $\boldsymbol{q_{t_1}}$. $\boldsymbol{q_0^*}$ is the total area between t=0 to t=∞

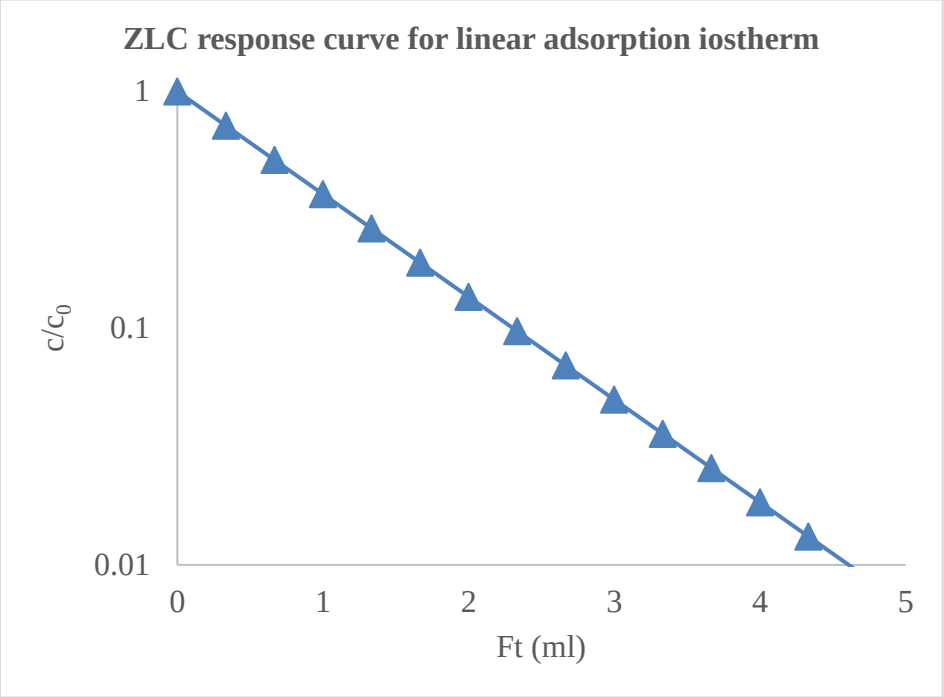

Figure 9.4 The case of a linear ZLC response curve $\boldsymbol{ln\frac{c}{c_0} = \frac{-Ft}{KV_s+V_g}}$

For the special cases of linear isotherm, e.g., Henry's Law, and nonlinear single-site Langmuir, integration of Equation 9.3 reduces to the simplified equations summarized in Table 9.1. Figure 9.4. illustrates an example of ZLC response curve for a linear isotherm

Table 0.1 Isotherm Equations and corresponding ZLC desorption curves equations for two simplified cases

Isotherm type	Isotherm Equation	ZLC desorption curve equation
Linear isotherm (Henry's Law)	$\bar{q} = q^* = Kc$	$ln\frac{c}{c_0} = \frac{-Ft}{KV_s + V_g}$
Nonlinear isotherm (Single-site Langmuir)	$\frac{q*}{q_s} = \frac{bc}{1 + bc}$	$ln\frac{c}{c_0} = \frac{-Ft}{KV_s} + ln(1-\lambda) - \lambda$ $\lambda = \frac{bc_0}{1+bc_0}; K = bq_s$

9.5. Experimental Procedure

ZLC can be used for permanent gases as well as vapors from organic solvents. Experiments consist of two main stages: (1) an adsorption stage, also known as equilibration, followed by (2) a purge (or desorption) stage. See Figure 9.5. It is the desorption step that is used to determine isotherm data. The desorption stage should be performed under the equilibrium-controlled conditions. Often, a pretreatment stage that involves purging with pure carrier gas at elevated temperatures precedes the adsorption stage to make sure the pores of the adsorbent are free from residual moisture or other contaminants.

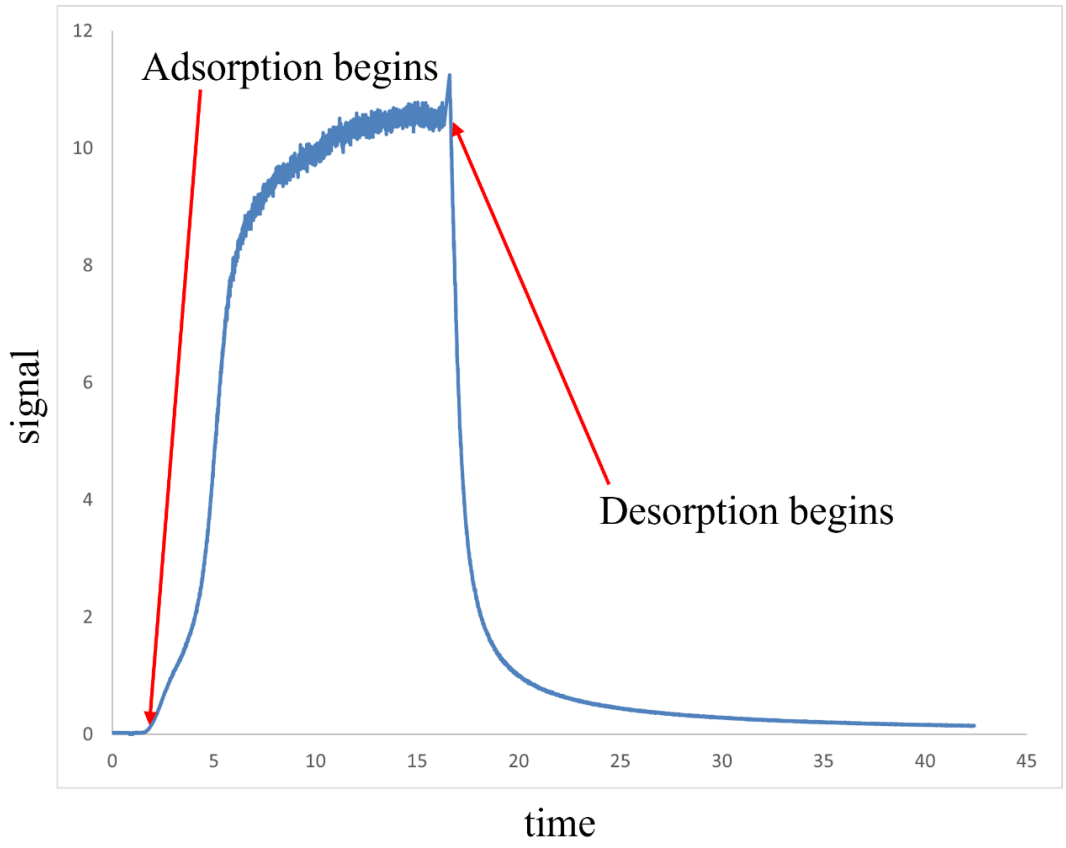

Figure 9.5 The two major steps of a ZLC experiment: Adsorption step and Desorption step. It is the data from the desorption step that is used for isotherm generation

9.5.1. ZLC for permanent gases on zeolites

For ZLC tests on permanent gases, we used our own in-house built setup as shown in Figures 9.6 to 9.7. 5-10 mg of an adsorbent was placed inside a 1/8" Swagelok compression union fitting closed at both ends with nickel sinter disks. The sample holder was mounted back onto tubing inside the GC oven. All the fittings were inspected for being airtight using soap water solution. The sample- and purge gas cylinders, and the MFC boxes were turned

on. The correct pressures and flow rates were adjusted. The cylinder regulators were set on a pressure of 40 psi before the pre-heat runs were started. To shift between adsorption mode and desorption mode, VICI valves were used When using the GC450 Varian, the VICI valve was set in desorption position corresponding to (-) or fill mode on the GC valve table. Then, the mass spectrometer was turned on.

A) Adsorption (Equilibration):

After the preheat stage was completed, the GC method was selected and loaded. GC method refers to the file in which all the settings chosen for the specific experiment including the oven temperature and detector settings are saved. As soon as the signals were ready, the RGA software of the mass spectrometer was opened, and a new file was saved. The scan mode of P vs T was selected, and the scan parameters were set for the gases of interest. The RGA software for mass spectrometer was connected and the filament of the mass spectrometer was turned on and allowed to warm up for a couple of hours while a background scan was in progress. Note that a general detector such as a Thermal Conductivity Detector (TCD) or Flame Ionization Detector (FID) can be used as an alternative to the mass spectrometer. The front panel of the GC was used to turn the VICI valve into inject (+) position, which started adsorption step.

B) Desorption (purging):

When the concentration reached a plateau on mass spectrum reading, the VICI valve was turned back to fill (-) position. (At this stage, one can stop the adsorption flows by switching off the MFC boxes). The signal on mass spectrometer was monitored until full desorption was achieved. When the measurement is complete stop scan was stopped and the filament

was turned off. An ASCII version of the output file was saved before being exported to MS Excel for data analysis. See Appendix F.

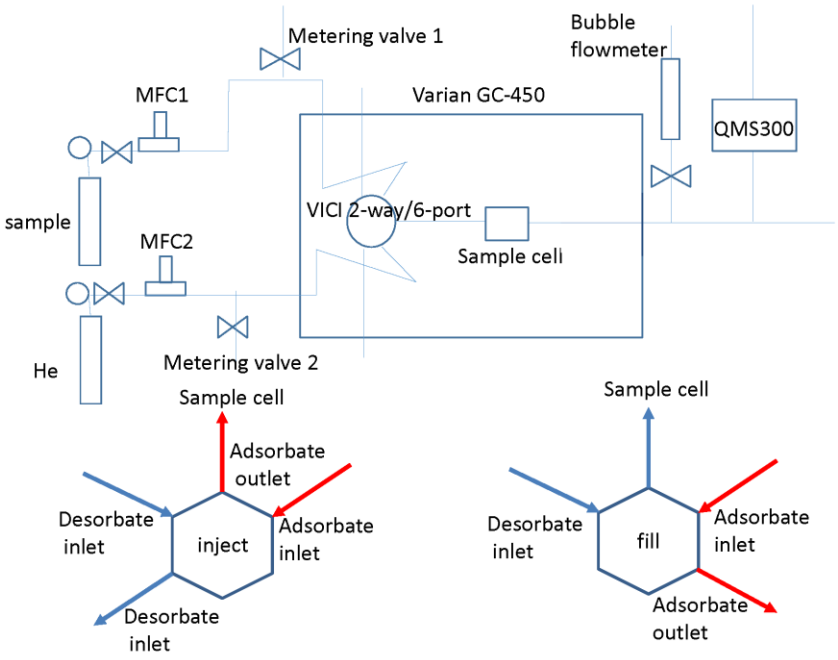

Figure 9.6 ZLC arrangement for permanent gases

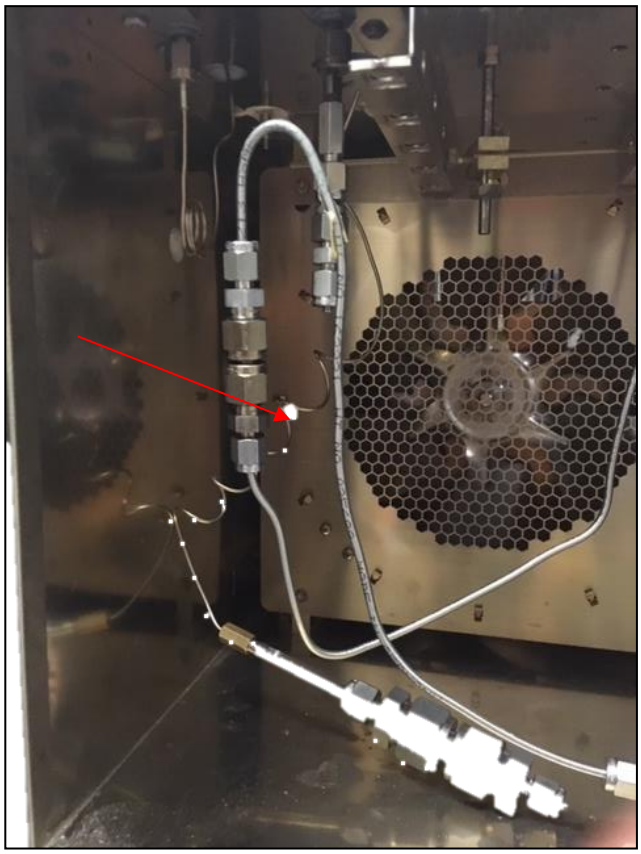

Figure 9.7 ZLC sample cell comprises a 1/8 " Swagelok fitting with a small amount of the sample sandwiched between nickel sintered disks as mounted inside GC oven. The sample cell is indicated by the red arrow

9.5.2. ZLC for IAA vapors on MOFs

IAA are liquids. Therefore, to measure their vapor isotherms, some modifications were needed to carry out the measurements as explained further in the text. See Figure 9.8. The sample cell was placed inside the GC oven equipped with an FID (used range 12 for optimal signal sensitivity). Carrier gas (helium) was passed through a bubbler placed inside a water bath. The low flow rate of the carrier gas ensured that the gas/vapor mixture leaving the

bubbler is saturated with sevoflurane. The saturation pressure of sevoflurane at 298K is 26.3 kPa, therefore at the operating conditions of 1 atm and 298K, the gas/vapor mixture has a concentration of 26% in sevoflurane vapor in helium. This saturated sevoflurane-carrier gas/vapor mixture was further diluted with a pure flow of the carrier gas to a desired final concentration using mass flow controllers. This final flow constituted the sample (adsorption) line, while a second flow of pure carrier gas with the same flow rate as the sample line served as the desorption line. We used a heating-tape blanket connected to a circuit consisting of a thermocouple, a VARIAC powerstat, and a temperature PID controller to prevent sevoflurane vapor from condensing inside the tubing.

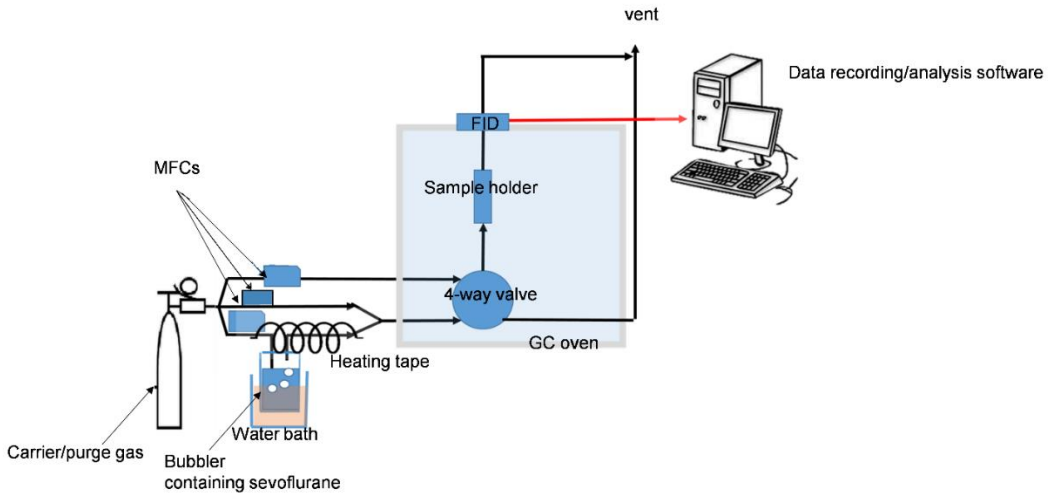

Figure 9.8 ZLC setup used for sevoflurane adsorption measurement

9.6. Results and Discussion

The ZLC adsorption isotherms for small permanent gases on selected zeolites and for IAA vapors on selected MOF structures (already introduced in Chapters 6 and 8) are shown in sections 9.6.1 and 9.6.2, respectively.

9.6.1. Permanent gases on zeolites

ZLC response curves for desorption of CO_2 from three selected zeolites is shown in Figure 9.10. They correspond to flow rates of 5 ml/min where equilibrium conditions are met. (For any flow rates below 5 ml/min, the curves for *log (c/c0)* vs *Ft* superimposes the corresponding curve at 5 ml/min). It should be noted the curves do not necessarily have to be straight lines. Straight lines occur for less polar adsorbates such as methane at low ranges of concentrations (Henry's Law region). [182] For CO_2 with a significant quadrupole interaction with the gradient of the electric field of the zeolite (see also Chapter 2, Section 2.2), the curve is expected to be nonlinear even for very low ranges of adsorbate concentration[183]. Data in Figure 9.9 is then used to generate the corresponding adsorption isotherms (see Section 1.1. of Appendix F) as shown in Figure 9.10 where they are compared with data from gravimetric measurements performed by our IGA instrument. Response curves and adsorption isotherms for different gases/adsorbents were obtained as shown in Appendix F. They all showed good agreement with data from IGA. These observations suggest that ZLC can conveniently replace the volumetric instrument for experimental verification or simulations as well as pre-screening of candidate adsorbents (see Figure 9.10) with the additional advantage of being a faster and less costly technique especially when dealing with dilute vapor/gas mixtures.

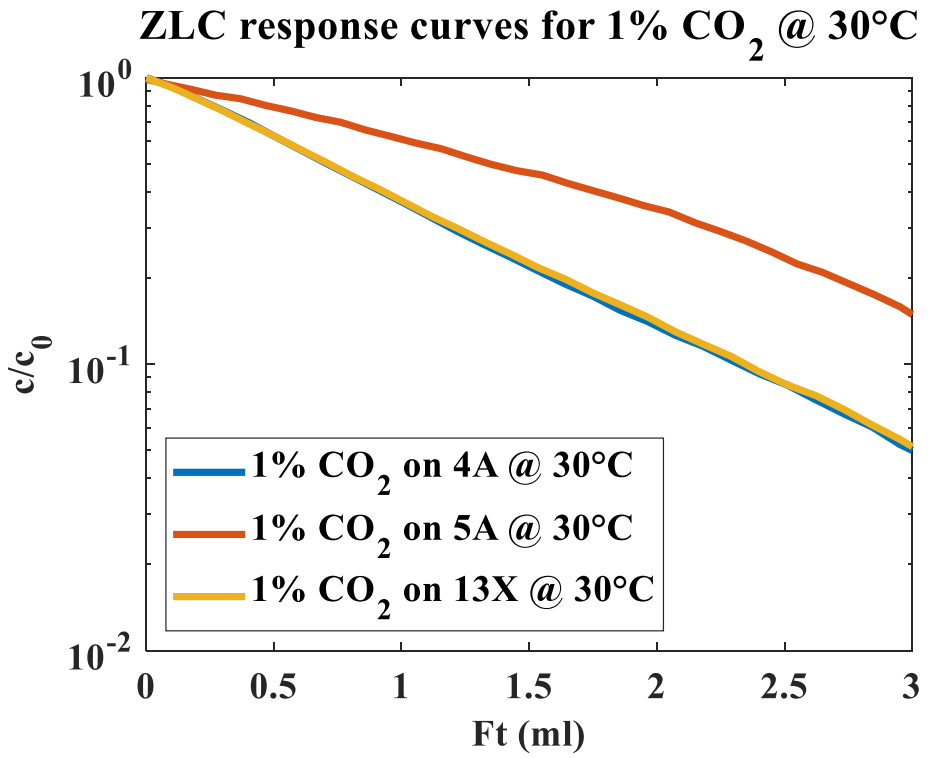

Figure 0.9 ZLC response curve for 1% CO_2 at 30°C for zeolites 4A, 5A and 13X

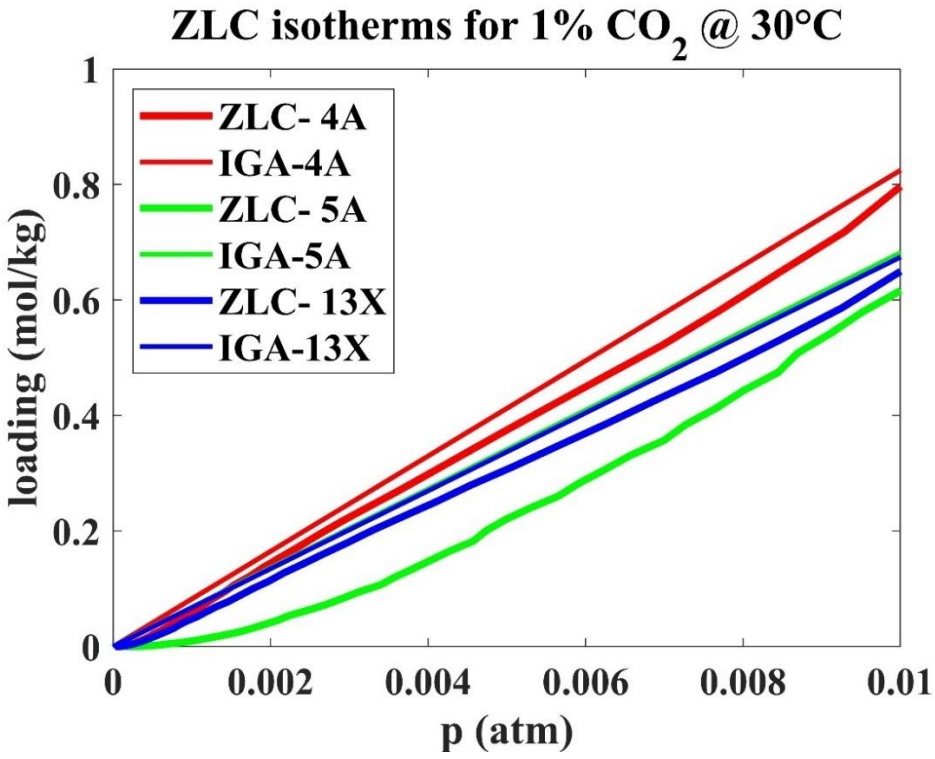

F

Figure 9.10 ZLC adsorption isotherms for 1% CO_2 at 30°C for zeolites 4A, 5A and 13X in comparison to IGA gravimetric (IGA) results

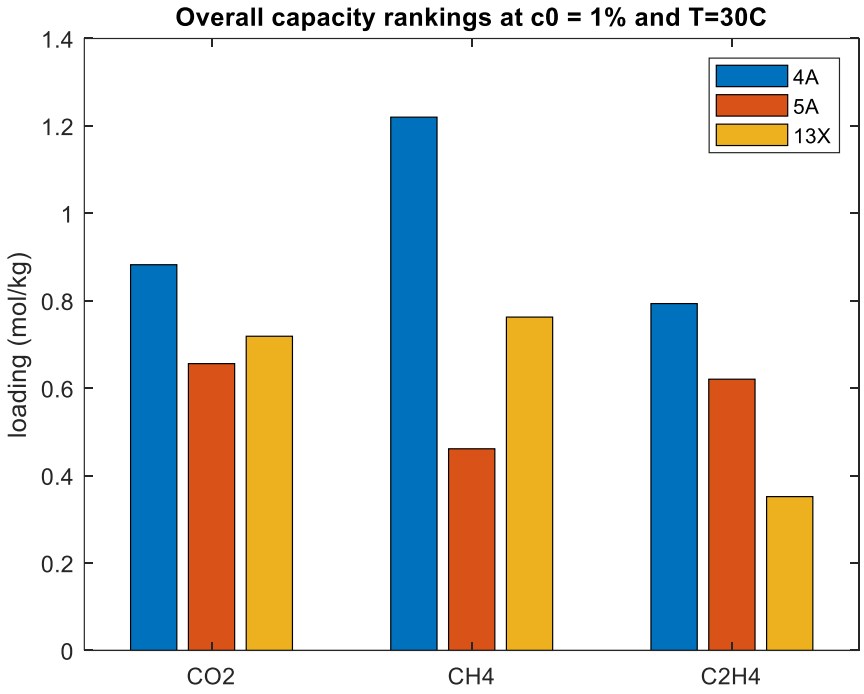

Figure 9.11 Overall adsorption capacity ranking of 4A, 5A, and 13X zeolite adsorbents for adsorbates CO_2, CH_4 , and C_2H_4.The results in the figure are an average between IGA and ZLC

9.6.2. Vapors on MOFs

The ZLC isotherms obtained for IAA vapors sevoflurane and desflurane are shown in Figures 9.12 and 9.13. Comparison with data from BELSORP shows good agreement. This observation suggests that ZLC can conveniently replace the volumetric instrument for experimental verification of simulated results as well as pre-screening of candidate adsorbents. ZLC possesses the additional advantage of being a faster and less costly technique especially when dealing with dilute vapor/gas mixtures. ZLC method is on

average 4 to 5 times faster than a traditional gravimetric or volumetric measurement due to much smaller sample size as well as detector choice. By replacing a detector with medium response time, such as a mass spectrometer, with more sensitive detectors such as FID or TCD, the speed of ZLC can be further enhanced viz-a-viz its traditional rivals. This observation was decisive in this work to shift from mass spectrometer to FID for measurement of isotherms for IAA vapors on MOFs.

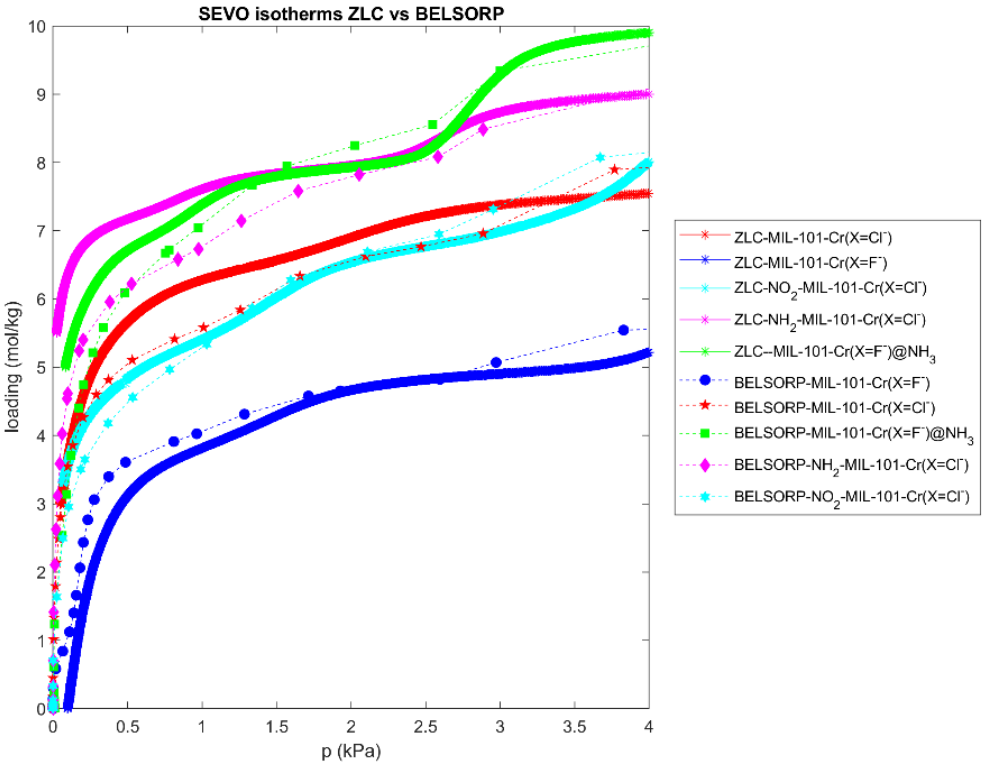

Figure 9.12 Adsorption isotherms for sevoflurane on different adsorbents at 298K are compared using Equilibrium ZLC, and volumetric adsorption (BELSORP)

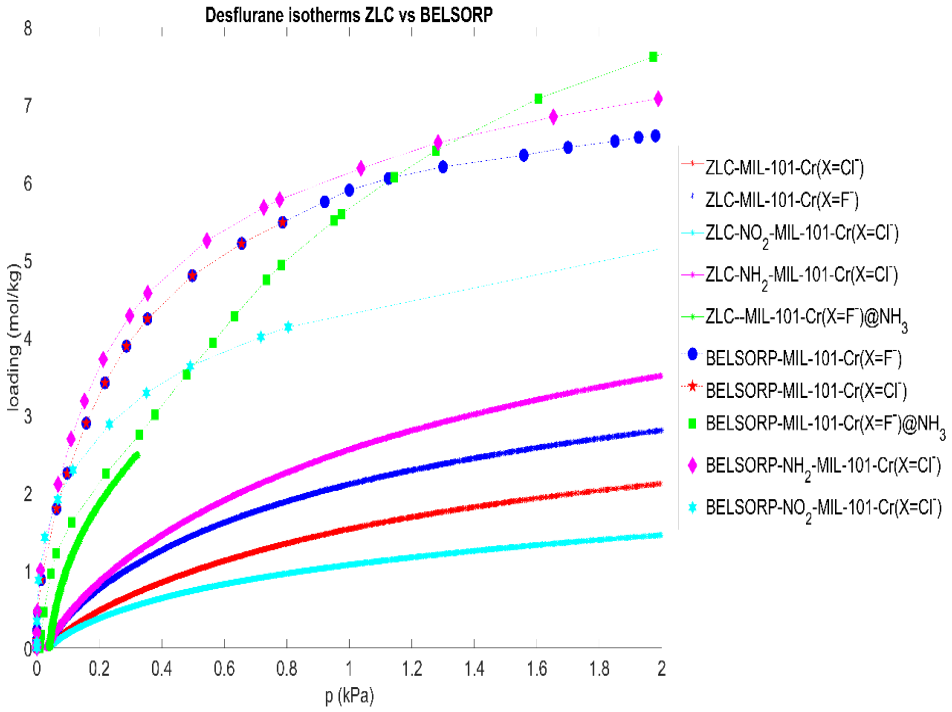

Figure 0.13 Adsorption isotherms for desflurane on different adsorbents at 298K are compared using Equilibrium ZLC, and volumetric adsorption (BELSORP)

9.7. Conclusions

ZLC response curves were used for obtaining adsorption isotherms for permanent adsorbate gases CO_2, CH_4 and C_2H_4 on zeolites 4A, 5A ,and 13X as well as vapors of IAA on MOF MIL-101-Cr and its derivates as described in Chapter 8. The isotherms were summarized and grouped based on the choice of adsorbate. The ZLC isotherms show good agreement with isotherms from our gravimetric and volumetric equipment. ZLC response curves were used to calculate and rank total adsorption capacities of the adsorbents for different adsorbates.

Advantages of ZLC technique can be concluded as follows: (1) smaller sample size requirements and shorter measurement times compared to the traditional methods. (2) A single ZLC run can provide the data needed for a complete isotherm curve and as it is a continuous line, the ZLC desorption corresponds to infinite number of isotherm equilibrium points (pressure points) compared to the traditional measurements that are confined to a discrete number of pre-assigned measurement pressure points. (3) The very nature of a ZLC measurement which is based on desorption makes the sample inside the measurement cell already regenerated and ready for the next test run , saving time when a sequence of isotherms are being measured on the same sample.(4) As hinted in (1) , ZLC method is on average 4 to 5 times faster than a traditional gravimetric or volumetric measurement, which makes ZLC the method of choice for rapid screening and ranking of a group of sample. When coupled with other characterization methods e.g. kinetic ZLC, equilibrium ZLC provides a complete picture of adsorption on a sorbent. ZLC has the capability to be used for binary and multicomponent adsorption measurement if mass spectrometer detection is employed

Chapter 10. General Conclusions and Future Work

10.1.Conclusions

Metal-organic frameworks (MOFs) are an interesting alternative to zeolites and activated carbon for adsorptive removal of wasted inhalation anesthetic agents (IAA) due to MOFs higher surface areas and structural diversity. This work studied the utility of molecular simulation of large- molecular vapors of inhalation anesthetic agents adsorption on three MOFs. All MOFs in the study have mesopores large enough to accommodate the IAA molecules.

To model the IAA molecules, use was made of forcefields specific to each adsorbate published by Arcario which includes parameters to account for molecular flexibility. Application of Continuous Fractional Component Monte Carlo (CFCMC) proved essential for speedy simulation of these large molecules provided that the right choice of the type and relative probability of the trial moves are considered. It was found that allocating 70% probability to the CFlambdaSwap MC trial move gives the best fit between simulation and experiment.

The exceptionally good agreement between experiment and simulation at the lower partial pressures using generic FF for MOFs with CUS can be attributed to the high polarity of the IAA molecules (compare dipole moments of SF 2.33D, DF 1.77D with water 1.85D [184]) which compensates for the CUS effect of the metal clusters. The choice of the FF for IAA

is thought to be critical only for medium to higher pressures where adsorbate-adsorbate interactions become more significant.

Our molecular simulation results also corroborated earlier reports on self-association of sevoflurane molecules [132] which is responsible for the kink observed in the isotherm of IAA on MOFs such as MOF-177-Zn whose structures do not contain open-metal sites.

Several modifications to pristine MIL-101-Cr ($X=F^-$, OH^-) were performed and their capacity towards IAA molecules was assessed using volumetric experimental technique and molecular simulation. The results indicate that our previously successful molecular simulation approach [167] applies equally well for modified structures and can simplify the task of designing superior adsorbents and reduce the number of trials and errors during experimental modification and characterization procedures. Which is advantageous in terms of both time and expense. Our present work introduced several new adsorbents for IAA, where grafting NH_3 to the metal cluster more than doubled the capacity towards sevoflurane but slightly decreased capacity towards desflurane. The latter observation hints at the potential of MIL-101-Cr ($X=F^-$, OH^-)@NH_3 to selectively remove sevoflurane from its binary mixture with desflurane.

ZLC response curves were used to obtain adsorption isotherms for permanent gases CO_2, CH_4 ,and C_2H_4 on zeolite adsorbents 4A, 5A, and 13X. The usefulness of the method was also demonstrated for other systems**,** such as vapors of sevoflurane and desflurane IAA on MOF MIL-101-Cr and its derivatives as described in Chapters 6 and 8. The isotherms were

summarized and grouped based on the choice of adsorbate. The ZLC isotherms show good agreement with isotherms from our gravimetric and volumetric equipments. ZLC response curves were used to calculate and rank total adsorption capacities of the adsorbents for different adsorbates.

Advantages of ZLC technique can be concluded as follows: (1) smaller sample size requirements and shorter measurement times compared to the traditional methods. (2) A single ZLC run can provide the data needed for a complete isotherm curve and as it is a continuous line, the ZLC desorption corresponds to infinite number of isotherm equilibrium points (pressure points) compared to the traditional measurements that are confined to a discrete number of pre-assigned measurement pressure points. (3)The very nature of a ZLC measurement which is based on desorption makes the sample inside the measurement cell already regenerated and ready for the next test run , saving time when a sequence of isotherms are being measured on the same sample.(4) As hinted in (1) , ZLC method is on average 4 to 5 times faster than a traditional gravimetric or volumetric measurement, which makes ZLC the method of choice for rapid screening and ranking of a group of sample. When coupled with other characterization methods e.g. kinetic ZLC, equilibrium ZLC provides a complete picture of adsorption on a sorbent. ZLC has the capability to be used for binary and multicomponent adsorption measurement if mass spectrometer detection is employed.

10.2.Recommendations for Future Work

High-speed computational screening of adsorbents[185] for different applications has become an active area of research recently thanks to the advances in high-performance computing and Machine Learning Algorithms[186]. These efforts have been mainly applied to smaller adsorbates such as hydrogen[185], methane[187][188] and carbon dioxide[187]. It should be beneficial to extend it to larger molecules such as IAA. One important result to watch for is to assess sensitivity of the simulations and the rankings on the choice of force field and the method of atomic partial charge calculation[189].

Another interesting area as follow-up to the present thesis is to perform dynamic breakthrough tests[190] and kinetic tests for determination of diffusivity of IAA molecules inside MOF structures[191]. Use of ZLC as a fast technique can prove to be a wise choice for the kinetic measurements[192] as it uses very small amount of sample and can be performed for large sets of adsorbents at a relatively short time using the relatively cheap equipment.

For future work, it is also suggested to try isotherm adsorption measurements for binary mixtures involving IAA. The binary mixture composition could include sevoflurane/desflurane vs water, sevoflurane/desflurane vs carbon dioxide, and sevoflurane vs desflurane. Also, it would be worthwhile to try a ternary mixture of IAA/water/CO_2. These tests will give us better idea of the selectivity of the new adsorbents explored in this thesis towards IAA.

Finally, it would be worthwhile exploring other post-synthetic routes for modification of promising adsorbents.

References

[1] Y. R. Tao, G. H. Zhang, and H. J. Xu, "Grand canonical Monte Carlo (GCMC) study on adsorption performance of metal organic frameworks (MOFs) for carbon capture," *Sustain. Mater. Technol.*, vol. 32, no. December 2021, 2022, doi: 10.1016/j.susmat.2021.e00383.

[2] T. N. Ang, B. R. Young, R. Burrell, M. Taylor, M. K. Aroua, and S. Baroutian, "Oxidative hydrothermal surface modification of activated carbon for sevoflurane removal," *Chemosphere*, vol. 264, 2021, doi: 10.1016/j.chemosphere.2020.128535.

[3] M. Mehrata, C. Moralejo, and W. A. Anderson, "Adsorbent comparisons for anesthetic gas capture in hospital air emissions," *J. Environ. Sci. Heal. - Part A Toxic/Hazardous Subst. Environ. Eng.*, vol. 51, no. 10, pp. 805–809, Aug. 2016, doi: 10.1080/10934529.2016.1181438.

[4] Y. Hua, N. Gargiulo, A. Peluso, P. Aprea, M. Eić, and D. Caputo, "Adsorption Behavior of Halogenated Anesthetic and Water Vapor on Cr-Based MOF (MIL-101) Adsorbent. Part I. Equilibrium and Breakthrough Characterizations," *Chemie-Ingenieur-Technik*, vol. 88, no. 11, pp. 1730–1738, 2016, doi: 10.1002/cite.201600052.

[5] D. J. Doyle, R. Byrick, D. Filipovic, and F. Cashin, "Silica zeolite scavenging of exhaled isoflurane: a preliminary report".

[6] N. Gargiulo *et al.*, "A chromium-based metal organic framework as a potential high performance adsorbent for anaesthetic vapours," *RSC Adv.*, vol. 4, no. 90, pp. 49478–49484, 2014, doi: 10.1039/c4ra05905k.

[7] Y. Hua, N. Gargiulo, A. Peluso, P. Aprea, M. Eić, and D. Caputo, "Adsorption

Behavior of Halogenated Anesthetic and Water Vapor on Cr-Based MOF (MIL-101) Adsorbent. Part II. Multiple-Cycle Breakthrough Tests," *Chemie-Ingenieur-Technik*, 2016, doi: 10.1002/cite.201600052.

[8] T. H. Chen *et al.*, "Mesoporous Fluorinated Metal-Organic Frameworks with Exceptional Adsorption of Fluorocarbons and CFCs," *Angew. Chemie - Int. Ed.*, vol. 54, no. 47, pp. 13902–13906, Nov. 2015, doi: 10.1002/anie.201505149.

[9] T. H. Chen, W. Kaveevivitchai, A. J. Jacobson, and O. S. Miljanić, "Adsorption of fluorinated anesthetics within the pores of a molecular crystal," *Chem. Commun.*, vol. 51, no. 74, pp. 14096–14098, Aug. 2015, doi: 10.1039/c5cc04885k.

[10] S. M. Cohen, "Postsynthetic Methods for the Functionalization of Metal–Organic Frameworks," *Chem. Rev.*, vol. 112, no. 2, pp. 970–1000, 2012, doi: 10.1021/cr200179u.

[11] Y. G. Chung *et al.*, "Computation-ready, experimental metal-organic frameworks: A tool to enable high-throughput screening of nanoporous crystals," *Chem. Mater.*, vol. 26, no. 21, pp. 6185–6192, 2014, doi: 10.1021/cm502594j.

[12] J. Burner *et al.*, "ARC-MOF: A Diverse Database of Metal-Organic Frameworks with DFT-Derived Partial Atomic Charges and Descriptors for Machine Learning," *Chem. Mater.*, vol. 35, no. 3, pp. 900–916, 2023, doi: 10.1021/acs.chemmater.2c02485.

[13] D. Frenkel and B. Smit, *Understanding Molecular Simulation, From Algorithm to Application*, 2nd ed. Academic Press, 2002.

[14] T. G. Glover and B. Mu, *Gas Adsorption in Metal-Organic Frameworks, Fundamental sand Applications*. 2019.

[15] E. J. Maginn and J. R. Elliott, “Historical perspective and current outlook for molecular dynamics as a chemical engineering tool,” *Ind. Eng. Chem. Res.*, vol. 49, no. 7, pp. 3059–3078, 2010, doi: 10.1021/ie901898k.

[16] R. A. Lippert *et al.*, “Accurate and efficient integration for molecular dynamics simulations at constant temperature and pressure,” *J. Chem. Phys.*, vol. 139, no. 16, 2013, doi: 10.1063/1.4825247.

[17] P. Teerachawanwong *et al.*, “Insights into the heat contributions and mechanism of CO2 adsorption on metal–organic framework MIL-100 (Cr, Fe): Experiments and molecular simulations,” *Fuel*, vol. 331, no. P2, p. 125863, 2023, doi: 10.1016/j.fuel.2022.125863.

[18] M. Haeri-nejad, “Use of molecular simulation for evaluating adsorption equilibrium of inhalation anaesthetic agents on metal – organic frameworks,” *Can. J. Chem. Eng.*, no. August, pp. 1–12, 2023, doi: 10.1002/cjce.25134.

[19] R. T. YANG, *Adsorbents: Fundamentals and Applications*. Hoboken, New Jersey: John Wiley and Sons Inc, 2003.

[20] R. M. Barrer, “Zeolites and their synthesis,” *Zeolites*, vol. 1, no. 3, pp. 130–140, 1981, doi: 10.1016/S0144-2449(81)80001-2.

[21] Y. Li and J. Yu, “New stories of zeolite structures: Their descriptions, determinations, predictions, and evaluations,” *Chem. Rev.*, vol. 114, no. 14, pp. 7268–7316, 2014, doi: 10.1021/cr500010r.

[22] M. Hartmann, M. Thommes, and W. Schwieger, “Hierarchically-Ordered Zeolites: A Critical Assessment,” *Adv. Mater. Interfaces*, vol. 8, no. 4, 2021, doi: 10.1002/admi.202001841.

[23] S. Smeets and Z. Xiaodong, *Zeolite structures*. 2017.

[24] IZA, “Database of Zeolite Structures,” *Http://Www.Iza-Structure.Org/Databases/*, pp. 1–5, 2017, [Online]. Available: http://www.iza-structure.org/databases/

[25] Z. Heidarinejad, M. H. Dehghani, M. Heidari, G. Javedan, I. Ali, and M. Sillanpää, “Methods for preparation and activation of activated carbon: a review,” *Environ. Chem. Lett.*, vol. 18, no. 2, pp. 393–415, 2020, doi: 10.1007/s10311-019-00955-0.

[26] S. Wong, N. Ngadi, I. M. Inuwa, and O. Hassan, “Recent advances in applications of activated carbon from biowaste for wastewater treatment: A short review,” *J. Clean. Prod.*, vol. 175, pp. 361–375, 2018, doi: 10.1016/j.jclepro.2017.12.059.

[27] G. Newcombe, R. Hayes, and M. Drikas, “Granular activated carbon: Importance of surface properties in the adsorption of naturally occurring organics,” *Colloids Surfaces A Physicochem. Eng. Asp.*, vol. 78, no. C, pp. 65–71, 1993, doi: 10.1016/0927-7757(93)80311-2.

[28] P. Lewińska and A. Gałaś, “Carbon Moelcular Sieve Gs Separation Materials and Membranes: A Comprehensive Review,” *J. South Am. Earth Sci.*, p. 103058, 2020, doi: 10.1016/j.memsci.2024.122533.

[29] O. M. Yaghi, “Reticular Chemistry in All Dimensions,” *ACS Cent. Sci.*, p. acscentsci.9b00750, 2019, doi: 10.1021/acscentsci.9b00750.

[30] M. Ermer, J. Mehler, B. Rosenberger, M. Fischer, P. S. Schulz, and M. Hartmann, “UiO-66 and hcp UiO-66 Catalysts Synthesized from Ionic Liquids as Linker Precursors,” *ChemistryOpen*, pp. 1–11, 2020, doi: 10.1002/open.202000291.

[31] B. A. Day and C. E. Wilmer, “Genetic Algorithm Design of MOF-Based Gas Sensor Arrays for CO 2 -in-Air Sensing,” no. December, pp. 1–10, 2019, doi:

10.20944/preprints201912.0281.v1.

[32] M. Vallet-Regí, F. Balas, and D. Arcos, “Mesoporous materials for drug delivery,” *Angew. Chemie - Int. Ed.*, vol. 46, no. 40, pp. 7548–7558, 2007, doi: 10.1002/ANIE.200604488.

[33] W. Xu and O. M. Yaghi, “Metal − Organic Frameworks for Water Harvesting from Air, Anywhere, Anytime,” *ACS Cent. Sci.*, 2020, doi: 10.1021/acscentsci.0c00678.

[34] N. Gargiulo and A. Peluso, “MOF-Based Adsorbents for Atmospheric Emission Control : A Review,” pp. 1–21.

[35] M. I. Severino, E. Gkaniatsou, F. Nouar, M. L. Pinto, and C. Serre, “MOFs industrialization: A complete assessment of production costs,” *Faraday Discuss.*, vol. 231, pp. 326–341, 2021, doi: 10.1039/d1fd00018g.

[36] Q. Qian *et al.*, “MOF-Based Membranes for Gas Separations,” *Chem. Rev.*, vol. 120, no. 16, pp. 8161–8266, 2020, doi: 10.1021/acs.chemrev.0c00119.

[37] Y. G. Chung *et al.*, “Advances, Updates, and Analytics for the Computation-Ready, Experimental Metal-Organic Framework Database: CoRE MOF 2019,” pp. 1–14, 2019, doi: 10.1021/acs.jced.9b00835.

[38] C. E. Wilmer *et al.*, “Large-scale screening of hypothetical metal-organic frameworks,” *Nat. Chem.*, vol. 4, no. 2, pp. 83–89, 2012, doi: 10.1038/nchem.1192.

[39] S. Yue, C. Oh, A. Nandy, G. G. Terrones, and H. J. Kulik, “Effects of MOF linker rotation and functionalization on methane uptake and diffusion,” *Mol. Syst. Des. Eng.*, p. 1DYMMY, 2023, doi: 10.1039/d2me00237j.

[40] S. Mandal, S. Natarajan, P. Mani, and A. Pankajakshan, “Post-Synthetic Modification of Metal–Organic Frameworks Toward Applications,” *Adv. Funct.*

Mater., vol. 2006291, pp. 1–22, 2020, doi: 10.1002/adfm.202006291.

[41] A. K. Ladavos, A. P. Katsoulidis, A. Iosifidis, K. S. Triantafyllidis, T. J. Pinnavaia, and P. J. Pomonis, "The BET equation, the inflection points of N 2 adsorption isotherms and the estimation of specific surface area of porous solids," *Microporous Mesoporous Mater.*, vol. 151, pp. 126–133, 2012, doi: 10.1016/j.micromeso.2011.11.005.

[42] C. G. V. Burgess, D. H. Evereter, and S. Nuttall, "Adsorption hysteresis in porous materials," *Pure Appl. Chem.*, vol. 61, no. 11, pp. 1845–1852, 1989, doi: 10.1351/pac198961111845.

[43] K. S. Sing, "Reporting physisorption data for gas/solid systems with special reference to the determination of surface area and porosity (Recommendations 1984)57.4," 1985.

[44] N. Saadatkhah *et al.*, "Experimental methods in chemical engineering: Thermogravimetric analysis—TGA," *Can. J. Chem. Eng.*, vol. 98, no. 1, pp. 34–43, 2020, doi: 10.1002/cjce.23673.

[45] T. M. Rossi, J. C. Campos, and M. M. V. M. Souza, "An evaluation of calcined hydrocalumite as carbon dioxide adsorbent using thermogravimetric analysis," *Appl. Clay Sci.*, vol. 182, no. February, p. 105252, 2019, doi: 10.1016/j.clay.2019.105252.

[46] Z. S. Liu, Y. H. Peng, C. Y. Huang, and M. J. Hung, "Application of thermogravimetry and differential scanning calorimetry for the evaluation of CO2 adsorption on chemically modified adsorbents," *Thermochim. Acta*, vol. 602, pp. 8–14, 2015, doi: 10.1016/j.tca.2015.01.002.

[47] L. Pellenz *et al.*, "A comprehensive guide for characterization of adsorbent materials," *Sep. Purif. Technol.*, vol. 305, no. August 2022, 2023, doi: 10.1016/j.seppur.2022.122435.

[48] J. Hafizovic *et al.*, "The inconsistency in adsorption properties and powder XRD data of MOF-5 is rationalized by framework interpenetration and the presence of organic and inorganic species in the nanocavities," *J. Am. Chem. Soc.*, vol. 129, no. 12, pp. 3612–3620, 2007, doi: 10.1021/ja0675447.

[49] D. Sud and G. Kaur, "A comprehensive review on synthetic approaches for metal-organic frameworks: From traditional solvothermal to greener protocols," *Polyhedron*, vol. 193, p. 114897, 2021, doi: 10.1016/j.poly.2020.114897.

[50] N. Saeidi and M. N. Lotfollahi, "Effects of powder activated carbon particle size on adsorption capacity and mechanical properties of the semi activated carbon fiber," *Fibers Polym.*, vol. 16, no. 3, pp. 543–549, 2015, doi: 10.1007/s12221-015-0543-6.

[51] Y. Qian, F. Zhang, and H. Pang, "A Review of MOFs and Their Composites-Based Photocatalysts: Synthesis and Applications," *Adv. Funct. Mater.*, vol. 31, no. 37, pp. 1–34, 2021, doi: 10.1002/adfm.202104231.

[52] H. C. J. Zhou and S. Kitagawa, "Metal-Organic Frameworks (MOFs)," *Chem. Soc. Rev.*, vol. 43, no. 16, pp. 5415–5418, 2014, doi: 10.1039/c4cs90059f.

[53] H. Li *et al.*, "Porous metal-organic frameworks for gas storage and separation: Status and challenges," *EnergyChem*, vol. 1, no. 1, p. 100006, 2019, doi: 10.1016/j.enchem.2019.100006.

[54] M. Li, D. Li, M. O'Keeffe, and O. M. Yaghi, "Topological analysis of metal-organic frameworks with polytopic linkers and/or multiple building units and the minimal

transitivity principle," *Chem. Rev.*, vol. 114, no. 2, pp. 1343–1370, 2014, doi: 10.1021/cr400392k.

[55] H. Furukawa, K. E. Cordova, M. O'Keeffe, and O. M. Yaghi, "The chemistry and applications of metal-organic frameworks," *Science (80-.).*, vol. 341, no. 6149, 2013, doi: 10.1126/science.1230444.

[56] M. O. F. Topologies, N. Stock, and S. Biswas, "Synthesis of Metal-Organic Frameworks (MOFs): Routes to Various," pp. 933–969, 2012.

[57] V. F. Yusuf, N. I. Malek, and S. K. Kailasa, "Review on Metal-Organic Framework Classification, Synthetic Approaches, and Influencing Factors: Applications in Energy, Drug Delivery, and Wastewater Treatment," *ACS Omega*, vol. 7, no. 49, pp. 44507–44531, 2022, doi: 10.1021/acsomega.2c05310.

[58] M. T. Luebbers, T. Wu, L. Shen, and R. I. Masel, "Trends in the adsorption of volatile organic compounds in a large-pore metal-organic framework, IRMOF-1," *Langmuir*, vol. 26, no. 13, pp. 11319–11329, Jul. 2010, doi: 10.1021/la100635r.

[59] D. Zhao, D. J. Timmons, D. Yuan, and H. C. Zhou, "Tuning the topology and functionality of metal-organic frameworks by ligand design," *Acc. Chem. Res.*, vol. 44, no. 2, pp. 123–133, 2011, doi: 10.1021/ar100112y.

[60] M. Fischer and R. G. Bell, "Interaction of hydrogen and carbon dioxide with sod-type zeolitic imidazolate frameworks: A periodic DFT-D study," *CrystEngComm*, vol. 16, no. 10, pp. 1934–1949, 2014, doi: 10.1039/c3ce42209g.

[61] Z. Wan *et al.*, "Separation selectivity of CH4 / CO2 gas mixtures in the ZIF-8 membrane explored by dynamic Monte Carlo simulations," *J. Chem. Inf. Model.*, 2020, doi: 10.1021/acs.jcim.0c00114.

[62] B. Chen, Z. Yang, Y. Zhu, and Y. Xia, “Zeolitic imidazolate framework materials: Recent progress in synthesis and applications,” *J. Mater. Chem. A*, vol. 2, no. 40, pp. 16811–16831, 2014, doi: 10.1039/c4ta02984d.

[63] R. Gaillac, P. Pullumbi, T. Bennett, and F. Coudert, “Nanoporous MOF for CO2 conversion CIF,” *ChemRxiv*, no. 2, 2020, doi: 10.26434/chemrxiv.12647006.v1.

[64] N. Behera, J. Duan, W. Jin, and S. Kitagawa, “The chemistry and applications of flexible porous coordination polymers,” *EnergyChem*, vol. 3, no. 6, p. 100067, 2021, doi: 10.1016/j.enchem.2021.100067.

[65] K. Kadota, N. T. Duong, Y. Nishiyama, E. Sivaniah, and S. Horike, “Synthesis of Porous Coordination Polymers using Carbon Dioxide as a Direct Source,” *Chem. Commun.*, 2019, doi: 10.1039/C9CC04771A.

[66] D. Wang, H. Yao, J. Ye, Y. Gao, H. Cong, and B. Yu, “Metal-Organic Frameworks (MOFs): Classification, Synthesis, Modification, and Biomedical Applications,” *Small*. John Wiley and Sons Inc, 2024. doi: 10.1002/smll.202404350.

[67] J. Duan, W. Jin, and R. Krishna, “Natural gas purification using a porous coordination polymer with water and chemical stability,” *Inorg. Chem.*, vol. 54, no. 9, pp. 4279–4284, May 2015, doi: 10.1021/ic5030058.

[68] M. Perfecto-Irigaray *et al.*, “[Zr6O4(OH)4(benzene-1,4-dicarboxylato)6]n: a hexagonal polymorph of UiO-66,” *Chem. Commun.*, vol. 55, no. 42, pp. 5954–5957, 2019, doi: 10.1039/c9cc00802k.

[69] C. Galicia, “Computational Insights into As (V) Removal from Water by UiO-66 Metal-,” no. V, 2020, doi: 10.1021/acs.jpcc.0c09465.

[70] I. Walton, C. Chen, J. M. Rimsza, T. M. Nenoff, and K. S. Walton, “Enhanced Sulfur

Dioxide Adsorption in UiO-66 Through Crystal Engineering and Chalcogen Bonding," *Cryst. Growth Des.*, 2020, doi: 10.1021/acs.cgd.0c00846.

[71] M. K. Matikolaei and E. Binaeian, "Boosting Ammonia Uptake within Metal − Organic Frameworks by Anion Modulating Strategy," *ACS Appl. Mater. Interfaces*, 2021.

[72] D. Jiang, C. Huang, J. Zhu, P. Wang, Z. Liu, and D. Fang, "Classification and role of modulators on crystal engineering of metal organic frameworks (MOFs)," *Coord. Chem. Rev.*, vol. 444, no. October, p. 214064, 2021, doi: 10.1016/j.ccr.2021.214064.

[73] R. Kitaura *et al.*, "Formation of a one-dimensional array of oxygen in a microporous metal-organic solid," *Science (80-.).*, vol. 298, no. 5602, pp. 2358–2361, Dec. 2002, doi: 10.1126/SCIENCE.1078481.

[74] S. Bhattacharjee, C. Chen, and W. S. Ahn, "Chromium terephthalate metal-organic framework MIL-101: Synthesis, functionalization, and applications for adsorption and catalysis," *RSC Adv.*, vol. 4, no. 94, pp. 52500–52525, Oct. 2014, doi: 10.1039/c4ra11259h.

[75] M. Y. Zorainy, M. Gar Alalm, S. Kaliaguine, and D. C. Boffito, "Revisiting the MIL-101 metal-organic framework: design, synthesis, modifications, advances, and recent applications," *Journal of Materials Chemistry A*, vol. 9, no. 39. Royal Society of Chemistry, pp. 22159–22217, Oct. 21, 2021. doi: 10.1039/d1ta06238g.

[76] M. Zou, M. Dong, and T. Zhao, "Advances in Metal-Organic Frameworks MIL-101(Cr)," *International Journal of Molecular Sciences*, vol. 23, no. 16. MDPI, Aug. 01, 2022. doi: 10.3390/ijms23169396.

[77] T. Steenhaut, Y. Filinchuk, and S. Hermans, "Aluminium-based MIL-100(Al) and

MIL-101(Al) metal-organic frameworks, derivative materials and composites: synthesis, structure, properties and applications," *J. Mater. Chem. A*, vol. 9, no. 38, pp. 21483–21509, 2021, doi: 10.1039/d1ta04444c.

[78] J. Canivet, J. Bonnefoy, C. Daniel, A. Legrand, B. Coasne, and D. Farrusseng, "Structure-property relationships of water adsorption in metal-organic frameworks," *New J. Chem.*, vol. 38, no. 7, pp. 3102–3111, 2014, doi: 10.1039/c4nj00076e.

[79] R. Grünker *et al.*, "A new metal-organic framework with ultra-high surface area," *Chem. Commun.*, vol. 50, no. 26, pp. 3450–3452, 2014, doi: 10.1039/c4cc00113c.

[80] Ü. Kökçam-Demir *et al.*, "Coordinatively unsaturated metal sites (open metal sites) in metal-organic frameworks: Design and applications," *Chem. Soc. Rev.*, vol. 49, no. 9, pp. 2751–2798, 2020, doi: 10.1039/c9cs00609e.

[81] Y. R. Lee, J. Kim, and W. S. Ahn, "Synthesis of metal-organic frameworks: A mini review," *Korean J. Chem. Eng.*, vol. 30, no. 9, pp. 1667–1680, 2013, doi: 10.1007/s11814-013-0140-6.

[82] I. G. Clayson, D. Hewitt, M. Hutereau, T. Pope, and B. Slater, "High Throughput Methods in the Synthesis, Characterization, and Optimization of Porous Materials," *Adv. Mater.*, vol. 32, no. 44, pp. 1–47, 2020, doi: 10.1002/adma.202002780.

[83] J. Klinowski, F. A. Almeida Paz, P. Silva, and J. Rocha, "Microwave-assisted synthesis of metal-organic frameworks," *Dalt. Trans.*, vol. 40, no. 2, pp. 321–330, 2011, doi: 10.1039/c0dt00708k.

[84] Z. X. Cai *et al.*, "General Synthesis of MOF Nanotubes via Hydrogen-Bonded Organic Frameworks toward Efficient Hydrogen Evolution Electrocatalysts," *ACS Nano*, vol. 16, no. 12, pp. 20851–20864, 2022, doi: 10.1021/acsnano.2c08245.

[85] R. January, R. D. Amato, F. Marmottini, M. J. Mcpherson, and M. Taddei, “A green , solvent-free route to functionalised metal-organic frameworks with UiO-66 topology,” no. 3, pp. 1–5, doi: 10.1039/x0xx00000x.

[86] B. Szczesniak, S. Borysiuk, J. Choma, and M. Jaroniec, “Mechanochemical synthesis of highly porous materials,” *Mater. Horizons*, vol. 7, no. 6, pp. 1457–1473, 2020, doi: 10.1039/d0mh00081g.

[87] H. Ren and T. Wei, “Electrochemical Synthesis Methods of Metal-Organic Frameworks and Their Environmental Analysis Applications: A Review,” *ChemElectroChem*, vol. 9, no. 13, 2022, doi: 10.1002/celc.202200196.

[88] M. P. Batten, M. Rubio-Martinez, T. Hadley, K. C. Carey, K. S. L. A. Polyzos, and M. R. Hill, “Continuous flow production of metal-organic frameworks,” *Curr. Opin. Chem. Eng.*, vol. 8, pp. 55–59, 2015, doi: 10.1016/j.coche.2015.02.001.

[89] D. Jiang, C. Huang, J. Zhu, P. Wang, Z. Liu, and D. Fang, “Classification and role of modulators on crystal engineering of metal organic frameworks (MOFs),” *Coord. Chem. Rev.*, vol. 444, p. 214064, 2021, doi: 10.1016/j.ccr.2021.214064.

[90] F. Bigdeli, M. N. A. Fetzer, B. Nis, A. Morsali, and C. Janiak, “Coordination modulation: a way to improve the properties of metal-organic frameworks,” *J. Mater. Chem. A*, vol. 11, no. 41, pp. 22105–22131, 2023, doi: 10.1039/d3ta03077f.

[91] Y. Liu *et al.*, “Design and Synthesis of a Zeolitic Organic Framework,” *Angew. Chemie Int. Ed.*, Mar. 2022, doi: 10.1002/anie.202203584.

[92] R. Q. Snurr, “It’s an Interesting MOF , but Is It Stable ?,” *Matter*, vol. 1, no. 1, pp. 26–27, 2019, doi: 10.1016/j.matt.2019.06.014.

[93] Y. An *et al.*, “The stability of MOFs in aqueous solutions—research progress and

prospects," *Green Chem. Eng.*, vol. 5, no. 2, pp. 187–204, 2024, doi: 10.1016/j.gce.2023.07.004.

[94] T. N. Ang, S. Baroutian, B. R. Young, M. M. Hyland, M. Taylor, and R. Burrell, "Adsorptive separation of volatile anaesthetics: A review of current developments," *Sep. Purif. Technol.*, vol. 211, no. June 2018, pp. 491–503, 2019, doi: 10.1016/j.seppur.2018.10.012.

[95] T. N. Ang *et al.*, "A techno-economic-societal assessment of recovery of waste volatile anaesthetics," *Sep. Purif. Technol.*, vol. 226, no. June, pp. 304–314, 2019, doi: 10.1016/j.seppur.2019.06.011.

[96] J. F. Butterworth, D. C. Mackey, J. D. Wasnick, G. E. Morgan, M. S. Mikhail, and G. E. Morgan, *Morgan and Mikhail's clinical anesthesiology*, 5th ed. New York: McGraw Hill Education Mecical, 2013.

[97] D. Bucher, C. Pasel, M. Luckas, J. Bentgens, and D. Bathen, "Adsorption of Inhalation Anesthetics (Fluranes and Ethers) on Activated Carbons and Zeolites at Trace Level Concentrations," *J. Chem. Eng. Data*, vol. 62, no. 6, pp. 1832–1841, 2017, doi: 10.1021/acs.jced.7b00079.

[98] G. Briggs and J. Maycock, "The anaesthetic machine," *Anaesth. Intensive Care Med.*, vol. 17, no. 3, pp. 115–119, 2016, doi: 10.1016/j.mpaic.2015.12.001.

[99] M. G. Martin and J. I. Siepmann, "Transferable potentials for phase equilibria. 1. United-atom description of n-alkanes," *J. Phys. Chem. B*, vol. 102, no. 14, pp. 2569–2577, 1998, doi: 10.1021/jp972543+.

[100] "Force Fields for MD simulations," 2005, [Online]. Available: http://www.ks.uiuc.edu/Training/Workshop/SanFrancisco/lectures/

[101] A. K. Rappé, C. J. Casewit, K. S. Colwell, W. A. Goddard, and W. M. Skiff, "UFF, a Full Periodic Table Force Field for Molecular Mechanics and Molecular Dynamics Simulations," *J. Am. Chem. Soc.*, vol. 114, no. 25, pp. 10024–10035, 1992, doi: 10.1021/ja00051a040.

[102] S. L. Mayo, B. D. Olafson, and W. A. Goddard, "DREIDING: A generic force field for molecular simulations," *J. Phys. Chem.*, vol. 94, no. 26, pp. 8897–8909, 1990, doi: 10.1021/j100389a010.

[103] E. A. Henle, N. Gantzler, P. K. Thallapally, X. Z. Fern, and C. M. Simon, "PoreMatMod.jl: Julia Package for in Silico Postsynthetic Modification of Crystal Structure Models", doi: 10.1021/acs.jcim.1c01219.

[104] P. Boone and C. E. Wilmer, "MOFUN: a Python package for molecular find and replace," *Digit. Discov.*, 2022, doi: 10.1039/d2dd00044j.

[105] Y. J. Colón, D. A. Gómez-Gualdrón, and R. Q. Snurr, "SI: Topologically-Guided , Automated Construction of MOFs and their Evaluation for Energy," *Cryst. Growth Des.*, vol. 17, pp. 5801–5810, 2017.

[106] A. Li, R. Bueno-Perez, and D. Fairen-Jimenez, "Identifying porous cage subsets in the Cambridge Structural Database using topological data analysis," *Chem. Sci.*, no. 3, 2022, doi: 10.1039/d2sc03171j.

[107] O. I. Lebedev, F. Millange, C. Serre, G. Van Tendeloo, and G. Férey, "First direct imaging of giant pores of the metal-organic framework MIL-101," *Chem. Mater.*, vol. 17, no. 26, pp. 6525–6527, 2005, doi: 10.1021/cm051870o.

[108] P. W. Hildebrand, A. S. Rose, and J. K. S. Tiemann, "Bringing Molecular Dynamics Simulation Data into View," *Trends Biochem. Sci.*, 2019, doi:

10.1016/j.tibs.2019.06.004.

[109] M. Haeri-nejad *et al.*, “A new vapor-liquid-equilibrium algorithm to improve accuracy of adsorption isotherm simulations”.

[110] M. N. Rosenbluth and A. W. Rosenbluth, “Monte Carlo simulations of the average extensios molecular chains,” *J. Chem. Phys.*, vol. 23, pp. 356–359, 1955.

[111] M. G. Martin and J. I. Siepmann, “Novel configurational-bias Monte Carlo method for branched molecules. Transferable potentials for phase equilibria. 2. United-atom description of branched alkanes,” *J. Phys. Chem. B*, vol. 103, no. 21, pp. 4508–4517, 1999, doi: 10.1021/jp984742e.

[112] J. Ilja Siepmann and D. Frenkel, “Conflgurational bias monte carlo: A new sampling scheme for flexible chains,” *Mol. Phys.*, vol. 75, no. 1, pp. 59–70, 1992, doi: 10.1080/00268979200100061.

[113] A. Poursaeidesfahani, R. Hens, A. Rahbari, M. Ramdin, D. Dubbeldam, and T. J. H. Vlugt, “Efficient Application of Continuous Fractional Component Monte Carlo in the Reaction Ensemble,” *J. Chem. Theory Comput.*, vol. 13, no. 9, pp. 4452–4466, 2017, doi: 10.1021/acs.jctc.7b00092.

[114] A. Torres-Knoop, S. P. Balaji, T. J. H. Vlugt, and D. Dubbeldam, “A comparison of advanced monte carlo methods for open systems: CFCMC vs CBMC,” *J. Chem. Theory Comput.*, vol. 10, no. 3, pp. 942–952, 2014, doi: 10.1021/ct4009766.

[115] A. Torres-Knoop *et al.*, “Optimization of particle transfers in the gibbs ensemble for systems with strong and directional interactions using CBMC, CFCMC, and CB/CFCMC,” *J. Phys. Chem. C*, vol. 120, no. 17, pp. 9148–9159, 2016, doi: 10.1021/acs.jpcc.5b11607.

[116] A. Rahbari, R. Hens, M. Ramdin, O. A. Moultos, D. Dubbeldam, and T. J. H. Vlugt, "Recent advances in the continuous fractional component Monte Carlo methodology," *Mol. Simul.*, vol. 47, no. 10–11, pp. 804–823, 2021, doi: 10.1080/08927022.2020.1828585.

[117] M. Munipalle, "A New Molecular Simulation Algorithm to Calculate Vapour-Liquid Equilibrium and its Applications," The University of Guelph, 2022.

[118] Q. Han, C. Deng, T. Gao, and Z. Jin, "Molecular Simulation on Competitive Adsorption Differences of Gas with Different Pore Sizes in Coal," pp. 0–11, 2022.

[119] F. M. S. Silva Fernandes and R. P. S. Fartaria, "Gibbs ensemble Monte Carlo," *Am. J. Phys.*, vol. 83, no. 9, pp. 809–816, Sep. 2015, doi: 10.1119/1.4921392.

[120] A. Sturluson *et al.*, "The role of molecular modelling and simulation in the discovery and deployment of metal-organic frameworks for gas storage and separation*," *Mol. Simul.*, vol. 45, no. 14–15, pp. 1082–1121, 2019, doi: 10.1080/08927022.2019.1648809.

[121] J. S. Lopez-Echeverry, S. Reif-Acherman, and E. Araujo-Lopez, "Peng-Robinson equation of state: 40 years through cubics," *Fluid Phase Equilib.*, vol. 447, pp. 39–71, 2017, doi: 10.1016/j.fluid.2017.05.007.

[122] N. Mayr, M. Haring, and T. Wallek, "Continuous fractional component Gibbs ensemble Monte Carlo," *Am. J. Phys.*, vol. 91, no. 3, pp. 235–246, Mar. 2023, doi: 10.1119/5.0135841.

[123] D. Dubbeldam, S. Calero, D. E. Ellis, and R. Q. Snurr, "RASPA: Molecular simulation software for adsorption and diffusion in flexible nanoporous materials," *Mol. Simul.*, vol. 42, no. 2, pp. 81–101, 2016, doi:

10.1080/08927022.2015.1010082.

[124] J. K. Shah *et al.*, “Cassandra: An open source monte carlo package for molecular simulation,” *J. Comput. Chem.*, vol. 38, no. 19, pp. 1727–1739, 2017, doi: 10.1002/jcc.24807.

[125] M. G. Martin, “MCCCS Towhee: A tool for monte carlo molecular simulation,” *Molecular Simulation*, vol. 39, no. 14–15. Taylor & Francis, pp. 1212–1222, 2013. doi: 10.1080/08927022.2013.828208.

[126] T. F. Willems, C. H. Rycroft, M. Kazi, J. C. Meza, and M. Haranczyk, “Algorithms and tools for high-throughput geometry-based analysis of crystalline porous materials,” *Microporous Mesoporous Mater.*, vol. 149, no. 1, pp. 134–141, 2012, doi: 10.1016/j.micromeso.2011.08.020.

[127] M. D. Hanwell, D. E. Curtis, D. C. Lonie, T. Vandermeersch, E. Zurek, and G. R. Hutchinson, “Avogadro: an advanced semantic chemical editor, visualization, and analysis platform,” *J. Cheminform.*, no. 4, pp. 1–17, 2012, doi: 10.1016/j.aim.2014.05.019.

[128] K. Momma and F. Izumi, “VESTA 3 for three-dimensional visualization of crystal, volumetric and morphology data,” *J. Appl. Crystallogr.*, vol. 44, no. 6, pp. 1272–1276, 2011, doi: 10.1107/S0021889811038970.

[129] D. Dubbeldam, S. Calero, and T. J. H. Vlugt, “iRASPA: GPU-accelerated visualization software for materials scientists,” *Mol. Simul.*, vol. 44, no. 8, pp. 653–676, 2018, doi: 10.1080/08927022.2018.1426855.

[130] D. F. Geerdink, “In silico screening of zeolites for application in high pressure hydrogen dehydration Daan Ferdinand Geerdink In silico screening of zeolites for

application in high pressure hydrogen dehydration by".

[131] N. Gargiulo, A. Peluso, P. Aprea, M. Eić, and D. Caputo, "An insight into clustering of halogenated anesthetics molecules in metal-organic frameworks: Evidence of adsorbate self-association in micropores," *J. Colloid Interface Sci.*, vol. 554, pp. 463–467, 2019, doi: 10.1016/j.jcis.2019.07.032.

[132] N. Gargiulo, A. Peluso, P. Aprea, M. Eić, and D. Caputo, "An insight into clustering of halogenated anesthetics molecules in metal-organic frameworks: Evidence of adsorbate self-association in micropores," *J. Colloid Interface Sci.*, vol. 554, pp. 463–467, Oct. 2019, doi: 10.1016/j.jcis.2019.07.032.

[133] G. Akiyama, R. Matsuda, H. Sato, A. Hori, M. Takata, and S. Kitagawa, "Effect of functional groups in MIL-101 on water sorption behavior," *Microporous Mesoporous Mater.*, vol. 157, pp. 89–93, 2012, doi: 10.1016/j.micromeso.2012.01.015.

[134] F. Zhang *et al.*, "Substituent-Induced Electron-Transfer Strategy for Selective Adsorption of N2 in MIL-101(Cr)-X Metal-Organic Frameworks," *ACS Appl. Mater. Interfaces*, vol. 14, no. 1, pp. 2146–2154, Jan. 2022, doi: 10.1021/acsami.1c22866.

[135] J. Gao, S. Fei, Y. L. Ho, R. Matsuda, H. Daiguji, and J. J. Delaunay, "Water Confined in MIL-101(Cr): Unique Sorption-Desorption Behaviors Revealed by Diffuse Reflectance Infrared Spectroscopy and Molecular Dynamics Simulation," *J. Phys. Chem. C*, vol. 125, no. 32, pp. 17786–17795, 2021, doi: 10.1021/acs.jpcc.1c03351.

[136] M. Haouas, C. Volkringer, T. Loiseau, G. Férey, and F. Taulelle, "Monitoring the

activation process of the giant pore MIL-100(Al) by solid state NMR," *J. Phys. Chem. C*, vol. 115, no. 36, pp. 17934–17944, 2011, doi: 10.1021/jp206513v.

[137] D. Saha and S. Deng, "Hydrogen Adsorption on Metal-Organic Framework MOF-177," *Tsinghua Sci. Technol.*, vol. 15, no. 4, pp. 363–376, Aug. 2010, doi: 10.1016/S1007-0214(10)70075-4.

[138] M. D'Amore, B. Civalleri, I. J. Bush, E. Albanese, and M. Ferrabone, "Elucidating the Interaction of CO2 in the Giant Metal-Organic Framework MIL-100 through Large-Scale Periodic Ab Initio Modeling," *J. Phys. Chem. C*, vol. 123, no. 47, pp. 28677–28687, Nov. 2019, doi: 10.1021/acs.jpcc.9b06533.

[139] M. J. Arcario, C. G. Mayne, and E. Tajkhorshid, "Atomistic models of general anesthetics for use in in silico biological studies," *J. Phys. Chem. B*, vol. 118, no. 42, pp. 12075–12086, 2014, doi: 10.1021/jp502716m.

[140] D. Ongari, P. G. Boyd, O. Kadioglu, A. K. MacE, S. Keskin, and B. Smit, "Evaluating Charge Equilibration Methods to Generate Electrostatic Fields in Nanoporous Materials," *J. Chem. Theory Comput.*, vol. 15, no. 1, pp. 382–401, 2019, doi: 10.1021/acs.jctc.8b00669.

[141] W. Shi and E. J. Maginn, "Continuous fractional component Monte Carlo: An adaptive biasing method for open system atomistic simulations," *J. Chem. Theory Comput.*, vol. 3, no. 4, pp. 1451–1463, 2007, doi: 10.1021/ct7000039.

[142] J. Skvara and W. R. Smith, "Personal Communication," 2022.

[143] B. Yeskendir, J. P. Dacquin, Y. Lorgouilloux, C. Courtois, S. Royer, and J. Dhainaut, "From metal-organic framework powders to shaped solids: Recent developments and challenges," *Materials Advances*, vol. 2, no. 22. Royal Society of

Chemistry, pp. 7139–7186, Nov. 21, 2021. doi: 10.1039/d1ma00630d.

[144] M. Lammert, S. Bernt, F. Vermoortele, D. E. De Vos, and N. Stock, "Single- and mixed-linker Cr-MIL-101 derivatives: A high-throughput investigation," *Inorg. Chem.*, vol. 52, no. 15, pp. 8521–8528, Aug. 2013, doi: 10.1021/ic4005328.

[145] D. Yuan, R. B. Getman, Z. Wei, R. Q. Snurr, and H. C. Zhou, "Stepwise adsorption in a mesoporous metal-organic framework: Experimental and computational analysis," *Chem. Commun.*, vol. 48, no. 27, pp. 3297–3299, 2012, doi: 10.1039/c2cc17168f.

[146] E. A. Berdonosova, K. A. Kovalenko, E. V. Polyakova, S. N. Klyamkin, and V. P. Fedin, "Influence of Anion Composition on Gas Sorption Features of Cr-MIL-101 Metal-Organic Framework," *J. Phys. Chem. C*, vol. 119, no. 23, pp. 13098–13104, 2015, doi: 10.1021/acs.jpcc.5b02861.

[147] M. Fischer, J. R. B. Gomes, and M. Jorge, "Computational approaches to study adsorption in MOFs with unsaturated metal sites," *Molecular Simulation*, vol. 40, no. 7–9. Taylor & Francis, pp. 537–556, 2014. doi: 10.1080/08927022.2013.829228.

[148] M. F. De Lange *et al.*, "Understanding adsorption of highly polar vapors on mesoporous MIL-100(Cr) and MIL-101(Cr): Experiments and molecular simulations," *J. Phys. Chem. C*, vol. 117, no. 15, pp. 7613–7622, 2013, doi: 10.1021/jp3128077.

[149] D. Saha and S. Deng, "Structural stability of metal organic framework MOF-177," *J. Phys. Chem. Lett.*, vol. 1, no. 1, pp. 73–78, Jan. 2010, doi: 10.1021/jz900028u.

[150] P. B. S. Rallapalli, M. C. Raj, S. Senthilkumar, R. S. Somani, and H. C. Bajaj, "HF-

Free Synthesis of MIL-101 (Cr) and Its Hydrogen Adsorption Studies," vol. 35, no. 2, pp. 461–468, 2016, doi: 10.1002/ep.

[151] K. C. Chong *et al.*, "Solvent-Free Synthesis of MIL-101(Cr) for CO2 Gas Adsorption: The Effect of Metal Precursor and Molar Ratio," *Sustain.*, vol. 14, no. 3, Feb. 2022, doi: 10.3390/su14031152.

[152] G. D. Degaga, R. Pandey, C. Gupta, and L. Bharadwaj, "Tailoring of the electronic property of Zn-BTC metal-organic framework: Via ligand functionalization: An ab initio investigation," *RSC Adv.*, vol. 9, no. 25, pp. 14260–14267, 2019, doi: 10.1039/c9ra00687g.

[153] S. Ali, A. Razavi, and A. Morsali, "Linker functionalized metal-organic frameworks," *Coord. Chem. Rev.*, vol. 399, p. 213023, 2019, doi: 10.1016/j.ccr.2019.213023.

[154] M. Asgari *et al.*, "Understanding How Ligand Functionalization Influences CO2 and N2 Adsorption in a Sodalite Metal-Organic Framework," *Chem. Mater.*, vol. 32, no. 4, pp. 1526–1536, 2020, doi: 10.1021/acs.chemmater.9b04631.

[155] M. Kalaj and S. M. Cohen, "Postsynthetic Modification : An Enabling Technology for the Advancement of Metal − Organic Frameworks," *ACS Cent. Sci.*, 2020, doi: 10.1021/acscentsci.0c00690.

[156] R. B. Getman, J. H. Miller, K. Wang, and R. Q. Snurr, "Metal alkoxide functionalization in metal-organic frameworks for enhanced ambient-temperature hydrogen storage," *J. Phys. Chem. C*, vol. 115, no. 5, pp. 2066–2075, 2011, doi: 10.1021/jp1094068.

[157] N. Ko *et al.*, "Tailoring the water adsorption properties of MIL-101 metal-organic

frameworks by partial functionalization," *J. Mater. Chem. A*, 2015, doi: 10.1039/c4ta04907a.

[158] M. Sedighi, M. Reza, H. Sabzyan, S. Aghamiri, and P. Chen, "Evaluating equilibrium and kinetics of CO 2 and N 2 adsorption into amine-functionalized metal-substituted MIL-101 frameworks using molecular simulation," vol. 308, no. July 2021, 2022.

[159] S. S. Mortazavi, A. Abbasi, M. Masteri-Farahani, and F. Farzaneh, "Sulfonic Acid Functionalized MIL-101(Cr) Metal-Organic Framework for Catalytic Production of Acetals," *ChemistrySelect*, vol. 4, no. 25, pp. 7495–7501, 2019, doi: 10.1002/slct.201901070.

[160] X. Han *et al.*, "Fine-tuning the pore structure of metal-organic frameworks by linker substitution for enhanced hydrogen storage and gas separation," *CrystEngComm*, vol. 23, no. 16, pp. 3026–3032, 2021, doi: 10.1039/d1ce00087j.

[161] Z. Yin, S. Wan, J. Yang, M. Kurmoo, and M. H. Zeng, "Recent advances in post-synthetic modification of metal–organic frameworks: New types and tandem reactions," *Coord. Chem. Rev.*, vol. 378, pp. 500–512, 2019, doi: 10.1016/j.ccr.2017.11.015.

[162] A. Vimont *et al.*, "Investigation of acid sites in a zeotypic giant pores chromium(III) carboxylate," *J. Am. Chem. Soc.*, vol. 128, no. 10, pp. 3218–3227, Mar. 2006, doi: 10.1021/ja056906s.

[163] S. Lacour, "Functionalization of open-metal sites in stable MOFs through the use of small post-functionalized anchor molecules," Université de catholique Louvain Prof., 2020.

[164] L. Wang *et al.*, “Separation and Puri fi cation Technology Ethylenediamine-functionalized metal organic frameworks MIL-100 (Cr) for e ffi cient CO 2 / N 2 O separation,” *Sep. Purif. Technol.*, vol. 235, no. October 2019, p. 116219, 2020, doi: 10.1016/j.seppur.2019.116219.

[165] R. Zhong, X. Yu, W. Meng, J. Liu, C. Zhi, and R. Zou, “Amine-Grafted MIL-101(Cr) via Double-Solvent Incorporation for Synergistic Enhancement of CO2 Uptake and Selectivity,” *ACS Sustain. Chem. Eng.*, vol. 6, no. 12, pp. 16493–16502, 2018, doi: 10.1021/acssuschemeng.8b03597.

[166] Y. Li, F. Zhang, L. Wang, J. Yang, L. Li, and J. Li, “Study on the capure of N2O by MIL-101-Cr-F/Cl,” *CIESC J.*, vol. 72, no. 9, pp. 4759–4767, 2021.

[167] M. Haeri-Nejad and M. Eic, “Use of molecular simulation to evaluate adsorption equilibrium for inhalation anesthetics on metal-organic frameworks,” *Can. J. Chem. Eng.*, 2023.

[168] E. A. Henle, N. Gantzler, P. K. Thallapally, X. Z. Fern, and C. M. Simon, “PoreMatMod.jl: Julia package for in silico post-synthetic modification of crystal structure models,” *ChemRxiv*, 2021.

[169] R. Anderson and D. A. Gómez-Gualdrón, “Increasing topological diversity during computational ‘synthesis’ of porous crystals: how and why,” *CrystEngComm*, vol. 21, no. 10, pp. 1653–1665, 2019, doi: 10.1039/c8ce01637b.

[170] M. Haeri-Nejad and M. Eic, “Use of molecular simulation for evaluating adsorption equilibrium of inhalation anaesthetic agents on metal–organic frameworks,” *Can. J. Chem. Eng.*, no. October, pp. 1–12, 2023, doi: 10.1002/cjce.25134.

[171] T. A. Young, R. Gheorghe, and F. Duarte, “cgbind : A Python Module and Web App

for Automated Metallocage Construction and Host- Guest Characterization," pp. 1–24.

[172] J. Y. Wang, E. Mangano, S. Brandani, and D. M. Ruthven, "A review of common practices in gravimetric and volumetric adsorption kinetic experiments," *Adsorption*, vol. 27, no. 3, pp. 295–318, 2021, doi: 10.1007/s10450-020-00276-7.

[173] P. Pullumbi, F. Brandani, and S. Brandani, "Gas separation by adsorption: technological drivers and opportunities for improvement," *Current Opinion in Chemical Engineering*. 2019. doi: 10.1016/j.coche.2019.04.008.

[174] M. Eic and D. M. Ruthven, "A new experimental technique for measurement of intracrystalline diffusivity," *Zeolites*, vol. 8, no. 1, pp. 40–45, 1988, doi: 10.1016/S0144-2449(88)80028-9.

[175] A. Malekian, H. Vinh-Thang, Q. Huang, M. Eić, and S. Kaliaguine, "Evaluation of the main diffusion path in novel micro-mesoporous zeolitic materials with the zero length column method," *Ind. Eng. Chem. Res.*, 2007, doi: 10.1021/ie061497+.

[176] B. Shirani, X. Han, and M. Eic, "Application of ZLC Technique for a Comprehensive Study of Hydrocarbons' Kinetics in Carbon Molecular Sieves and Zeolites," *Sep. Purif. Technol.*, p. 115831, 2019, doi: 10.1016/j.seppur.2019.115831.

[177] F. Brandani, D. Ruthven, and C. G. Coe, "Measurement of adsorption equilibrium by the zero length column (ZLC) technique part 1: Single-component systems," *Ind. Eng. Chem. Res.*, 2003, doi: 10.1021/ie020572n.

[178] F. Brandani and D. Ruthven, "Measurement of Adsorption Equilibria by the Zero Length Column (ZLC) Technique Part 2: Binary Systems," 2003, doi:

10.1021/ie020573f.

[179] X. Hu, S. Brandani, A. I. Benin, and R. R. Willis, “Testing the stability of novel adsorbents for carbon capture applications using the zero length column technique,” *Chem. Eng. Res. Des.*, vol. 131, pp. 406–413, 2018, doi: 10.1016/j.cherd.2018.01.023.

[180] A. Centineo and S. Brandani, “Measurement of water vapor adsorption isotherms in mesoporous materials using the zero length column technique,” *Chem. Eng. Sci. X*, vol. 214, p. 100046, 2019, doi: 10.1016/j.cesx.2019.100046.

[181] S. Brandani and E. Mangano, *The zero length column technique to measure adsorption equilibrium and kinetics: lessons learnt from 30 years of experience*, vol. 27, no. 3. Springer US, 2021. doi: 10.1007/s10450-020-00273-w.

[182] S. Brandani, M. A. Jama, and D. M. Ruthven, “ZLC measurements under non-linear conditions,” *Chem. Eng. Sci.*, 2000, doi: 10.1016/S0009-2509(99)00411-X.

[183] E. Mangano, S. Brandani, and D. M. Ruthven, “Analysis and interpretation of zero length column response curves,” *Chemie-Ingenieur-Technik*, 2013, doi: 10.1002/cite.201300083.

[184] D. R. Lide, Ed., *CRC handbook of chemistry and phyics*, vol. 85. CRC Press, 2004.

[185] C. Altintas and S. Keskin, “On the shoulders of high-throughput computational screening and machine learning: Design and discovery of MOFs for H2 storage and purification,” *Mater. Today Energy*, vol. 38, p. 101426, 2023, doi: 10.1016/j.mtener.2023.101426.

[186] N. Rampal *et al.*, “The development of a comprehensive toolbox based on multi-level, high-throughput screening of MOFs for CO/N2separations,” *Chem. Sci.*, vol.

12, no. 36, pp. 12068–12081, 2021, doi: 10.1039/d1sc01588e.

[187] J. Rogacka, A. Seremak, A. Luna-triguero, and F. Formalik, “High-throughput screening of metal – Organic frameworks for CO 2 and CH 4 separation in the presence of water,” *Chem. Eng. J.*, vol. 403, no. June 2020, 2021, doi: 10.1016/j.cej.2020.126392.

[188] A. Ahmed and D. J. Siegel, “Predicting Hydrogen Storage in MOFs via Machine Learning (in preparation).,” pp. 1–15.

[189] C. Altintas and S. Keskin, “Role of partial charge assignment methods in high-throughput screening of MOF adsorbents and membranes for CO2/CH4 separation,” *Mol. Syst. Des. Eng.*, vol. 5, no. 2, pp. 532–543, Feb. 2020, doi: 10.1039/c9me00163h.

[190] A. Discovery, M. Frameworks, F. Energy, and R. Applications, “Accelerated Discovery of Metal-Organic Frameworks (MOFs) For Energy Related Applications,” 2020.

[191] H. Daglar and S. Keskin, “Recent advances, opportunities, and challenges in high-throughput computational screening of MOFs for gas separations,” *Coord. Chem. Rev.*, vol. 422, p. 213470, 2020, doi: 10.1016/j.ccr.2020.213470.

[192] D. Angi and F. Cakicioglu-Ozkan, “Adsorption kinetics of methane reformer off-gases on aluminum based metal-organic framework,” *Int. J. Hydrogen Energy*, 2020, doi: 10.1016/j.ijhydene.2020.08.100.

[193] H. Wu, F. Salles, and J. Zajac, “A critical review of solid materials for low-temperature thermochemical storage of solar energy based on solid-vapour adsorption in view of space heating uses,” *Molecules*, vol. 24, no. 5, 2019, doi:

10.3390/molecules24050945.

[194] P. Rocío-Bautista, I. Taima-Mancera, J. Pasán, and V. Pino, “Metal-organic frameworks in green analytical chemistry,” *Separations*, vol. 6, no. 3, pp. 1–21, 2019, doi: 10.3390/separations6030033.

[195] H. Furukawa, M. A. Miller, and O. M. Yaghi, “Independent verification of the saturation hydrogen uptake in MOF-177 and establishment of a benchmark for hydrogen adsorption in metal-organic frameworks,” *J. Mater. Chem.*, vol. 17, no. 30, pp. 3197–3204, 2007, doi: 10.1039/b703608f.

[196] Y. Hua, “Study of Metal Hydride Anode Material in Li-based Batteries and Halogenated Anesthetic Adsorption,” University of New Brunswick, 2017. doi: 10.1016/j.bbapap.2013.06.007.

[197] C. Férey *et al.*, “Chemistry: A chromium terephthalate-based solid with unusually large pore volumes and surface area,” *Science (80-.).*, vol. 309, no. 5743, pp. 2040–2042, 2005, doi: 10.1126/science.1116275.

[198] J. Shadmehr, S. Zeinali, and M. Tohidi, “Synthesis of a chromium terephthalate metal organic framework and use as nanoporous adsorbent for removal of diazinon organophosphorus insecticide from aqueous media,” *J. Dispers. Sci. Technol.*, vol. 40, no. 10, pp. 1423–1440, Oct. 2019, doi: 10.1080/01932691.2018.1516149.

[199] A. Santiago-Portillo, S. Navalón, P. Concepción, M. Álvaro, and H. García, “Influence of Terephthalic Acid Substituents on the Catalytic Activity of MIL-101(Cr) in Three Lewis Acid Catalyzed Reactions,” *ChemCatChem*, vol. 9, no. 13, pp. 2506–2511, 2017, doi: 10.1002/cctc.201700236.

[200] S. M. Ryan and C. J. Nielsen, “Global warming potential of inhaled anesthetics:

Application to clinical use," *Anesth. Analg.*, vol. 111, no. 1, pp. 92–98, 2010, doi: 10.1213/ANE.0b013e3181e058d7.

[201] D. Bucher, C. Pasel, M. Luckas, J. Bentgens, and D. Bathen, "Adsorption of Inhalation Anesthetics (Fluranes and Ethers) on Activated Carbons and Zeolites at Trace Level Concentrations," *J. Chem. Eng. Data*, vol. 62, no. 6, pp. 1832–1841, Jun. 2017, doi: 10.1021/acs.jced.7b00079.

[202] K. Zhang, Y. Chen, A. Nalaparaju, and J. Jiang, "Functionalized metal-organic framework MIL-101 for CO2 capture: Multi-scale modeling from ab initio calculation and molecular simulation to breakthrough prediction," *CrystEngComm*, vol. 15, no. 47, pp. 10358–10366, Dec. 2013, doi: 10.1039/c3ce41737a.

[203] J. Burner *et al.*, "ARC-MOF: A Diverse Database of Metal-Organic Frameworks with DFT-Derived Partial Atomic Charges and Descriptors for Machine Learning".

Appendices

Appendix A. Supplementary Information from Chapter 2

Section I. Examples of some traditional adsorbents discussed in Chapter 2

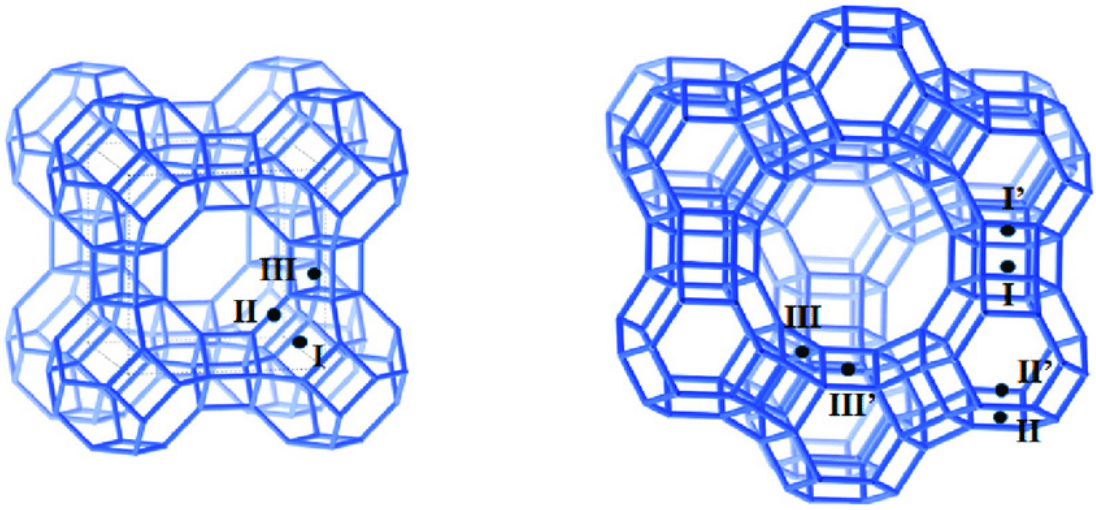

Figure 2.1S LTA and FAU zeolite structures with the locations of cations marked in roman numbers. With permission from [193]

Table 2.1S Comparison of the two main types of zeolites in common use for adsorption[19]

	Linde Type A (LTA)	**Linde Type X,Y (FAU*)**
Void fraction	0.2-0.5	0.2-0.5
Window size	4-membered oxygen rings	6-membered oxygen rings
Skeleton structure	Cages, windows	Cages, windows
Si/Al ratio	1	1-1.5 for X-type 1.5-3 for Y-type
SBU type	Truncated octahedron** and 4-membered prism	Truncated octahedron and 6-membered prism
Number of tetrahedra per unit cell	12 AlO_4 and 12 SiO_4	192 TO_4 (T=Al, Si): 77-96 AlO_4 for X type 48-76 AlO_4 for Y type
Maximum number of water molecules per unit cell	27 (located inside the central cage***)	27 (located inside the central cage)
Free diameter of the supercage (Å)	11.4	13.7
Aperture shapes of supercage (and number per unit cell)	8-member oxygen rings (12)	12-member oxygen rings (12)
Unobstructed diameter of supercage apertures (Å)	4.4	8.1
Negative charges per unit cell	12	Depending on # of Al atoms

*Also known as faujasite (a naturally occurring zeolite of the same structure)
**Also known as sodalite cage and β-cage
***Also known as supercage

Table 2.2S Cation distribution for different types of LTA [19]

Structure Name	3A	4A	5A
Cation type	K^+	Na^+	$Na^+/(Ca^{++})$
Type I	6	8	8
Type II	3	3	0
Type III	0	1	0
other	3		
Effective aperture size (Å)	3.0	3.8	5.3

Table 2.3S Cation distribution for different types of FAU [19]

Structure Name	10X	13X	13Y	LSX*
Cation type	Ca^{++}	Na^+	Na^+	Li^+
Type I	7.5	3.8	3	
Type I’	17.3	32.3	15	27.2
Type II	17.3	30.8	35	33.9
Type II’	9.0			
Type III		7.9		32.4
total	86	53	57	95.8
Effective aperture size (Å)	8	10	10	

*low-Si

Table 2.4S Steps for synthesis of activated carbon

	Temperature (°C)	**purpose**
Raw material preparation	ambient	pelletization
carbonization	400-500	Volatile matter elimination
Activation (gasification)	800-1000	Develop porosity and increase surface area

Section II. Instruments for textural characterization

Figure 2.2S SDT Q600 simultaneous TGA and DSC measurement instrument from TA Instruments, USA

.

Figure 2.3S Spectrum 100 FTIR spectroscope from Perkin-Elmer, UK

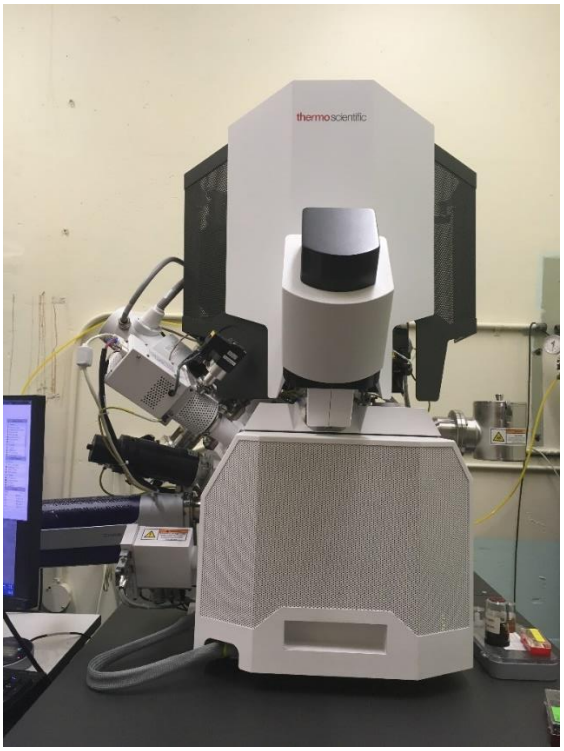

Figure 2.4S FE-SEM scanning electron microscopy from Thermoscientific, USA.

Appendix B. Supplementary Information from Chapter 3

Section I. Example of some common MOFs

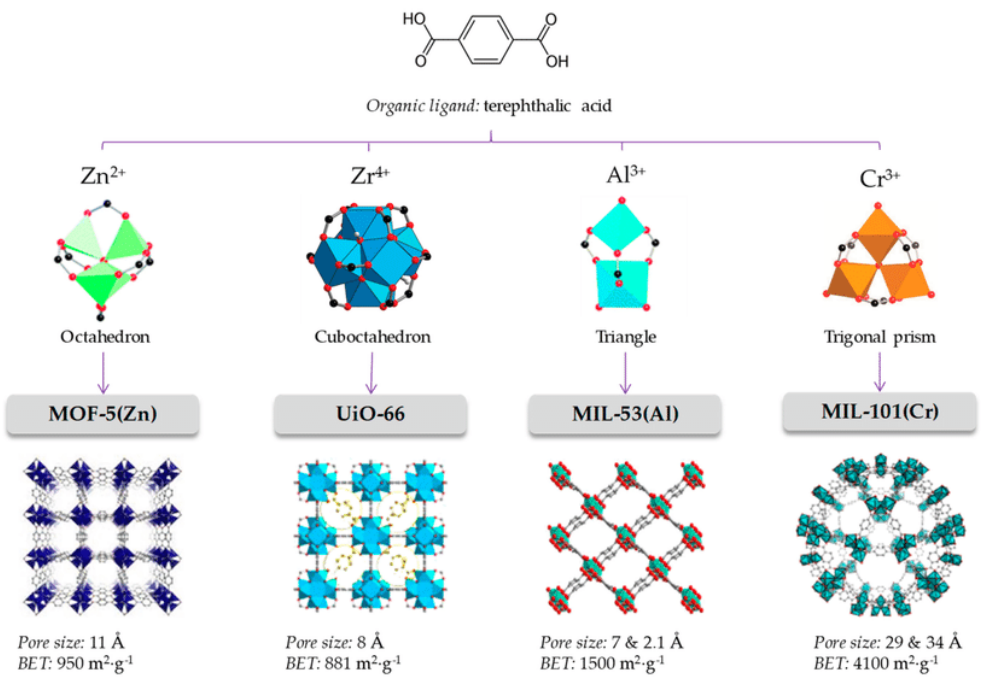

Figure 3.1S Examples of some common MOFs with their BET surface area and pore size(s) given. [194] Note how the metal-cluster geometry and the organic linker has affected the final topology and even the pore size of the resulting MOF.

Section II. Synthesis details of the MOFs discussed in this thesis

MIL-101-Cr (X=F, OH)

"4.00g of $Cr(NO_3)_3$•9H2O (Baker) was dissolved in 43.20g of ultra-purified water, which was produced by a TKA Smart2Pure device; 1.64g of terephthalic acid (Aldrich) and 5.0 mL of a 4 wt. % hydrofluoric acid solution, obtained by diluting a 37 wt. % pristine solution (Carlo Erba), were then added. These chemicals were mixed and kept in a stirrer for about 5 min. The resulting suspension was then transferred to a Teflon-lined autoclave bomb and kept in an oven at 493 K for 8 hours. After equilibration at ambient temperature, the large terephthalic acid crystals present in the batch were eliminated by filtration using a large pore fritted glass filter (no. 2); the water suspension of Cr-MOF powders which passed through the filter was then filtered again on Whatman ashless grade 42 filtration papers. The retained green product was finally dried at 333 K overnight."

MIL-100-Al

MIL-100-Al is the reaction product of $Al(NO_3)_3$ as metal precursor and the three-dentate trimesic acid as the linker ligand under strong acidic conditions (0.5<pH<0.7) . The sample used in this work was prepared using a new low-temperature method, leading to spherical agglomerates of nanocrystals [2]. Characterization data for this MOF is included in Section I of Supplementary Information .

MOF-177-Zn

Commercial MOF-177-Zn powder (Basolite® Z377) was purchased from Aldrich[132]. However, the most common recipe to its preparation is as follows: "N,N-Diethylformamide (DEF, BASF) is treated by addition of 0.5charcoal carbon into 1 L and stirred for 12 h at room temperature. The black suspension solution is filtered through a silica-gel column

(ca. 350 g, Silica gel 60, 230–400 mesh, EMD Chemicals) to remove carbon powder. Pure MOF-177 is prepared by dissolving 0.187 g of $Zn(NO_3)_2.6H_2O$ and 0.0395 g of 4,4',4''-benzene-1,3,5-triyl-tribenzoic acid (H3BTB), 10 mL of DEF in a 20 mL vial. The vial is capped tightly and placed in an oven at 85 °C for two days to yield clear block crystals. After cooling, the yellow solution is decanted, and the crystals are washed with 3 x 20 mL of N,N-dimethylformamide. The product is then immersed in 20 mL of chloroform for three days, during which time the activation solvent is decanted and freshly replenished three times. The crystals are transferred to a glass tube as a chloroform suspension by using a glass pipette to prevent exposure to air. The material is evacuated to 10^{-3} Torr at room temperature for 2 h, heated at a constant rate (1 °C /min) to 120 °C for 6 h, then cooled at a constant rate of 1 °C min^{-1} to room temperature. Powder X-ray diffraction patterns for as-synthesized and activated materials were coincident and in agreement with the simulated pattern, indicating the bulk purity of MOF-177 samples. Activated MOF-177 samples were handled using standard techniques to avoid exposure to air or moisture." [195]

NO_2-MIL-101-Cr (X=Cl^-)

The origin of the sample is a reaction approach containing freshly precipitated chromium hydroxide, 2-nitro-terphthalic acid, HCl and water at 180°C for 6 days. After this reaction, the solid was separated by centrifugation. The as-made product was suspended in hot DMF over night to remove remaining linker. The DMF was removed by extraction with ethanol for 24 hours before the sample was air-dried. The sample was dried in air at 150 °C. Full activation is done at 150-180 °C in vacuum. Characterization data for this MOF is included in Section I of Supplementary Information

NH_2-MIL-101-Cr (X=Cl^-)

One part of the NO_2-MIL-101-Cr ($X=Cl^-$) sample synthesized as described in 3 above was used in a reduction approach with $SnCl_2$ in ethanol to give NH_2-MIL-101-Cr ($X=Cl^-$). The remaining Sn residuals were washed out with concentrated HCl before the sample was washed with water again and dried once more. The sample was dried in air at 150 °C. Full activation is done at 150-180 °C in vacuum. Characterization data for this MOF is included in Section I of Supplementary Information.

MIL-101-Cr ($X=F^-$, OH^-)@NH_3

A portion of MIL-101-Cr ($X=F^-$, OH^-) (see 1 above) was first dried to remove coordinated water molecules of the saturated coordinated site (2 for MIL-101-Cr) followed by using an aqueous solution of ammonia to introduce NH_3 molecules as coordinated ligands to the CUS formed during drying. Comparison of elemental analysis for carbon and nitrogen for the initial and final samples showed that the substitution was successful at a rate of 1.5 coordinated NH_3 per trimeric metal cluster of the MOF. Subsequent PXRD data and SEM images confirmed preservation of the crystal structure of the resulting compound. Characterization data for this MOF is included in Section I of Supplementary Information

MIL-101-Cr ($X=Cl^-$, OH^-)

300 mg of MIL-101-Cr ($X=F^-$, OH^-) (see 1 above) was taken and exposed to perform anion exchange of the fluorine anions with chlorine anions using a 1N aqueous solution of NaCl. The mixture was stirred for 2 hours at room temperature. The solid was filtered off, washed by acetone, and finally dried over night at 80 °C. SEM images confirmed the preservation of the crystal structure and EDS mapping confirmed the presence of chlorine in the new structure. See Section I in Supplementary Information.

Appendix C. Supplementary Information from Chapter 6

Section I. Characterization results comparing Cr-MOF-1 and Cr-MOF-2

1. PXRD pattern for Cr-MOF-2

The PXRD pattern of Cr-MOF-2 is shown in Figure 6.1S.

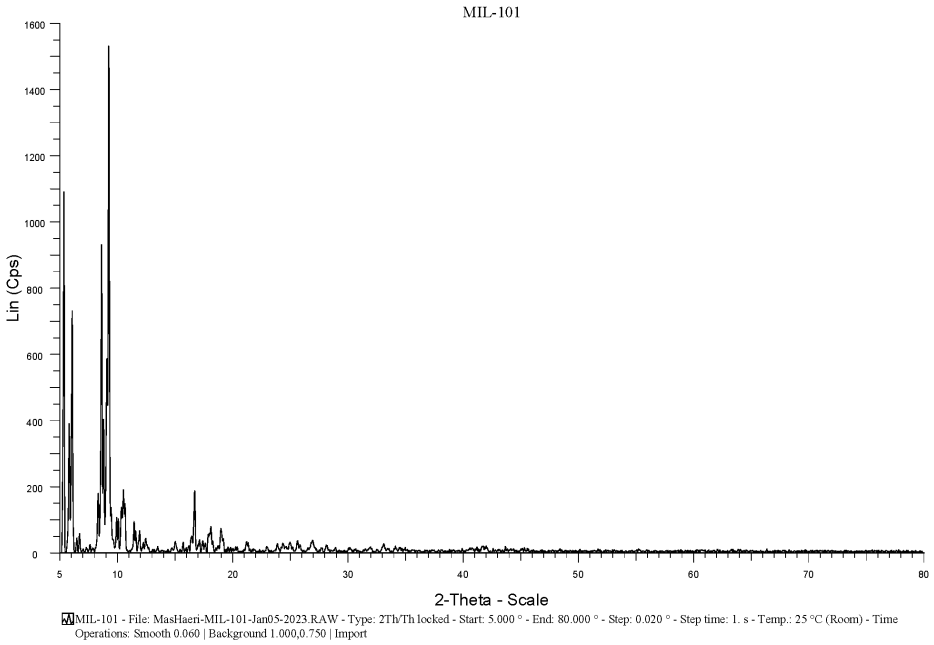

Figure 6.1S PXRD of Cr-MOF-2

The results are quite similar to the earlier reported patterns for Cr-MOF-1 (MIL-101-Cr) [196].

2. SEM Image of Cr-MOF-2

The SEM images for Cr-MOF-2 are shown in Figure 6.2S. The crystals have an average size of 1.25 micrometers. In addition, the elemental analysis using EDAX confirms the presence of chromium but no fluorine.

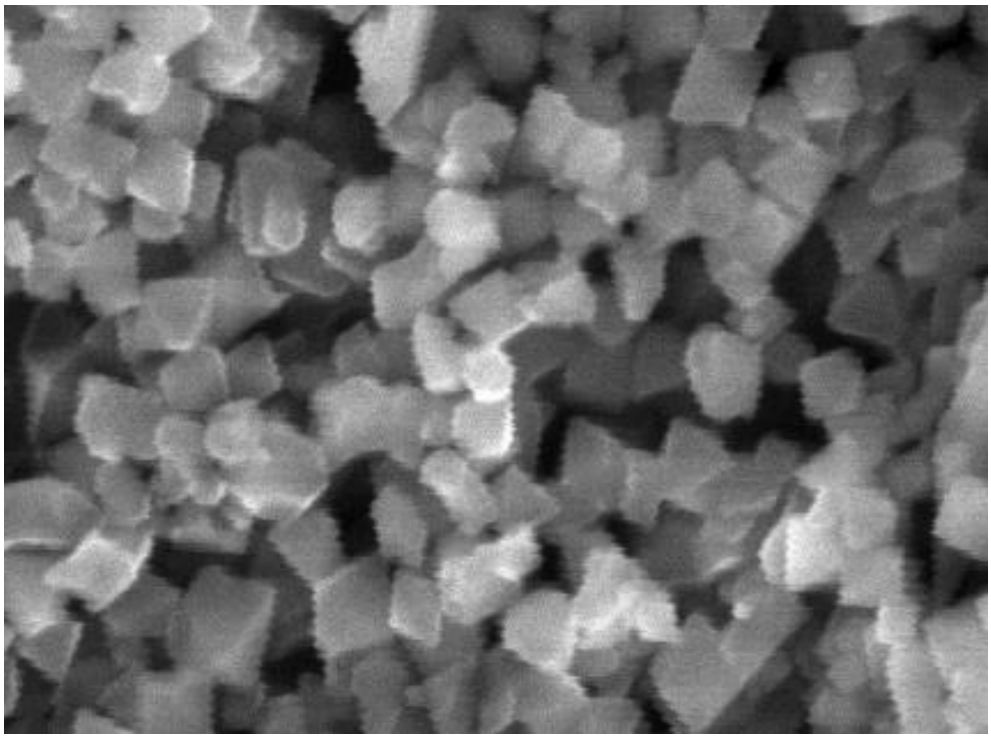

Figure 6.2S SEM image of Cr-MOF-2

3. TGA/DSC of Cr-MOF-1 and Cr-MOF-2

TGA/DSC results for the samples are summarized in Figures 6.3S and 6.4S.

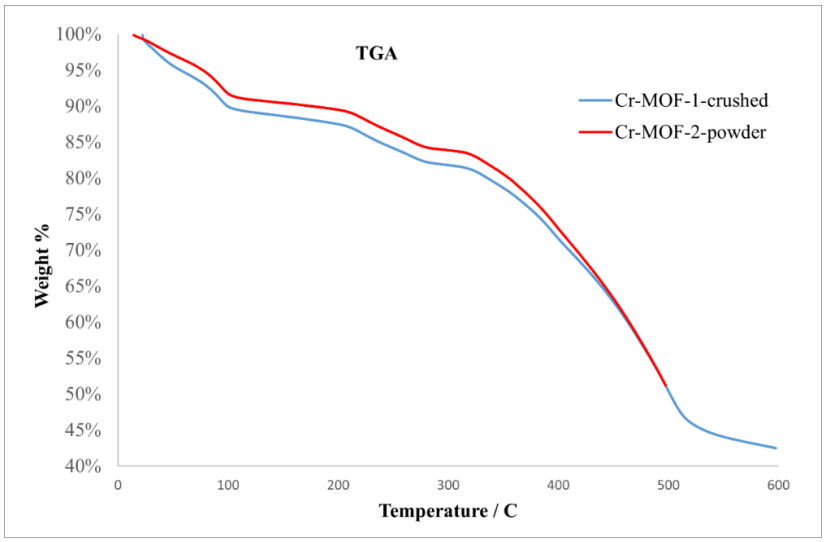

Figure 6.3S TGA of Cr-MOF-1-crushed and Cr-MOF-2-powder

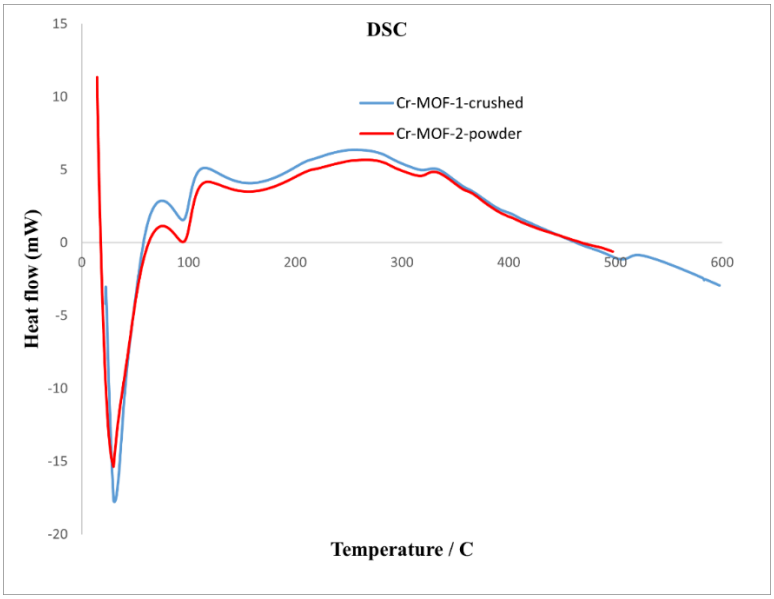

Figure 6.4S DSC of Cr-MOF-1-crushed and Cr-MOF-2-powder

As the MIL-101-Cr has two types of mesopores (29 Å and 34Å in diameter), there are two peaks/ steps expected at temperature ranges of below 100°C and 100-200°C corresponding to the larger pore and smaller pore, respectively. At the temperature range of 200-240°C coordinated water leaves the chromium and 240-300 °C corresponds to X ligands (here X= F, OH) leaving the structure. This latter phenomenon leads to formation of coordinated unsaturated sites (CUS) as evidenced by in-situ FT-IR spectroscopy[162] . At the range of 377- 500°C corresponding to melting point of the terephthalate ligand, the decomposition of the MOF structure occurs. The residual substance is chromium oxide and amorphous carbon[146]. These phenomena are also deducible from the DSC curves. It is also noteworthy that TGA and DSC are sensitive to the ramp rate of the purging gas (Figure 6.5S and 6.6S). As can be seen below, slower gas flow can cause greater weight loss due to the larger pore desorption and corresponding higher heat flow.

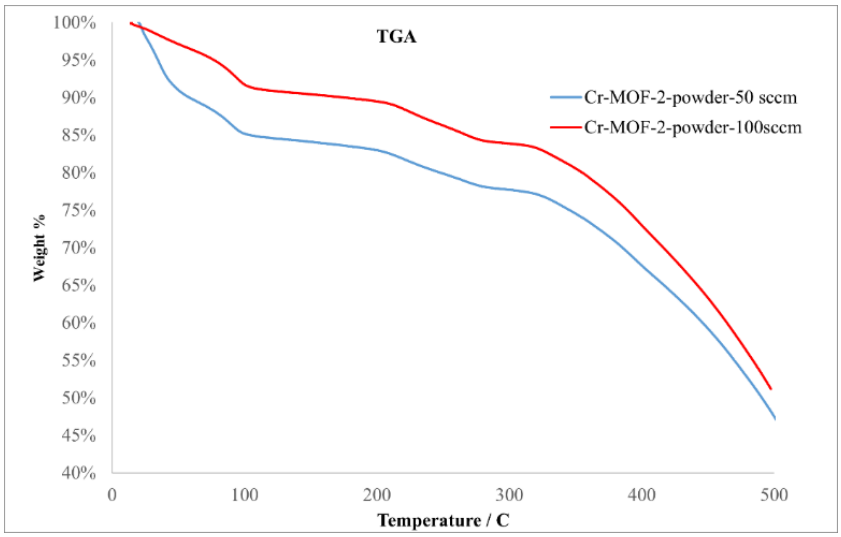

Figure 6.5S Flow rate effect on TGA for Cr-MOF-2

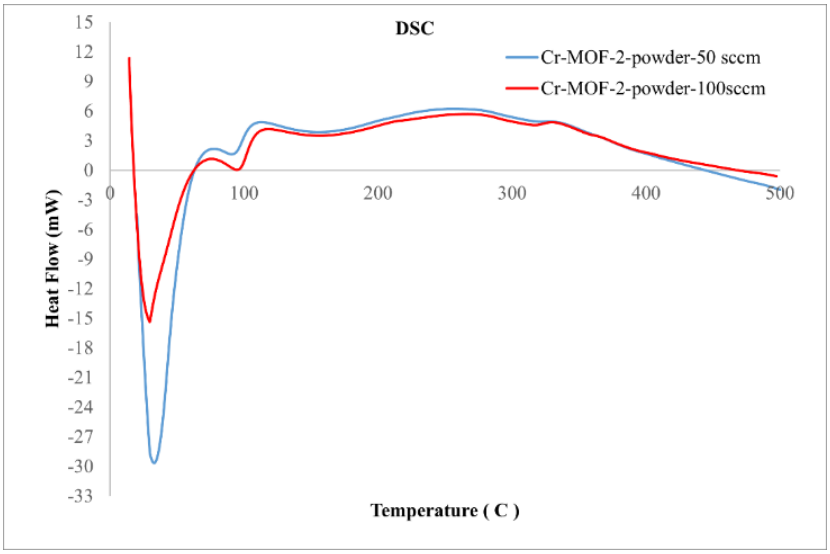

Figure 6.6S Flow rate effect on DSC for Cr-MOF-2

4. DRIFT-IR

Infra-red spectroscopy is often used in MOF characterization to find IR-active fractions. The results of the FTIR spectra for the two Cr-MOF samples are summarized in Figure 6.7S. It can be seen that the two samples have almost identical spectra. Moreover, the spectra match the published data for MIL-101-Cr[198] . The 1512 cm^{-1} and 1629 cm^{-1} peaks are due to COO^- and C-C in the linker. However, a shift can be observed from the reported 1515 cm^{-1} and 1640 cm^{-1} in the literature[199]. This could be due to some disconnected linkers in the MOF structure.

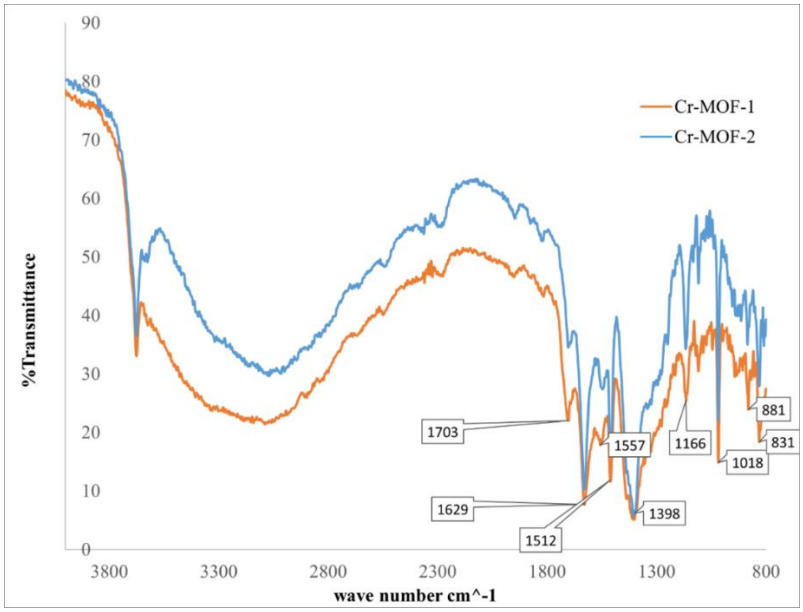

Figure 6.7S DRIFT-IR spectra of Cr-MOF-1 and Cr-MOF-2 The results match published data [198]

The results from TGA/DSC, FTIR, and Raman adequately confirm that Cr-MOF1 and Cr-MOF-2 are indeed MIL-101-Cr samples.

Section II. Characterization results of MIL-100(Al)

The sample was synthesized At Materials Center TU Dresden using a new low temperature method, leading to spherical agglomerates of nanocrystals. The sample was then activated at 180°C at 10^{-3} mbar. The analytical data (XPRD, Nitrogen physisorption and SEM) are provided by TU Dresden as below. Coordinated water can be removed once the sample is heated to 220°C where the open metal sites will be exposed.

1. PSD

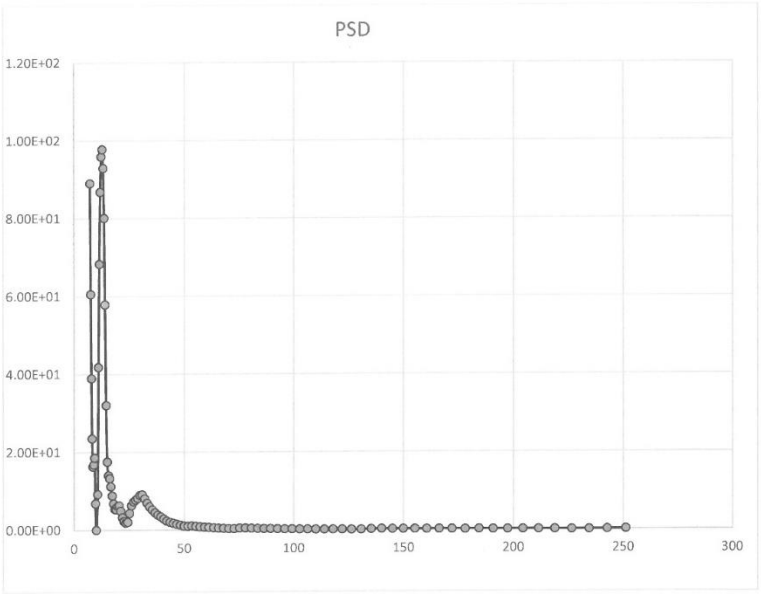

Figure 6.8S Pore Size Distribution of MIL-100-Al [1]

2. XPRD

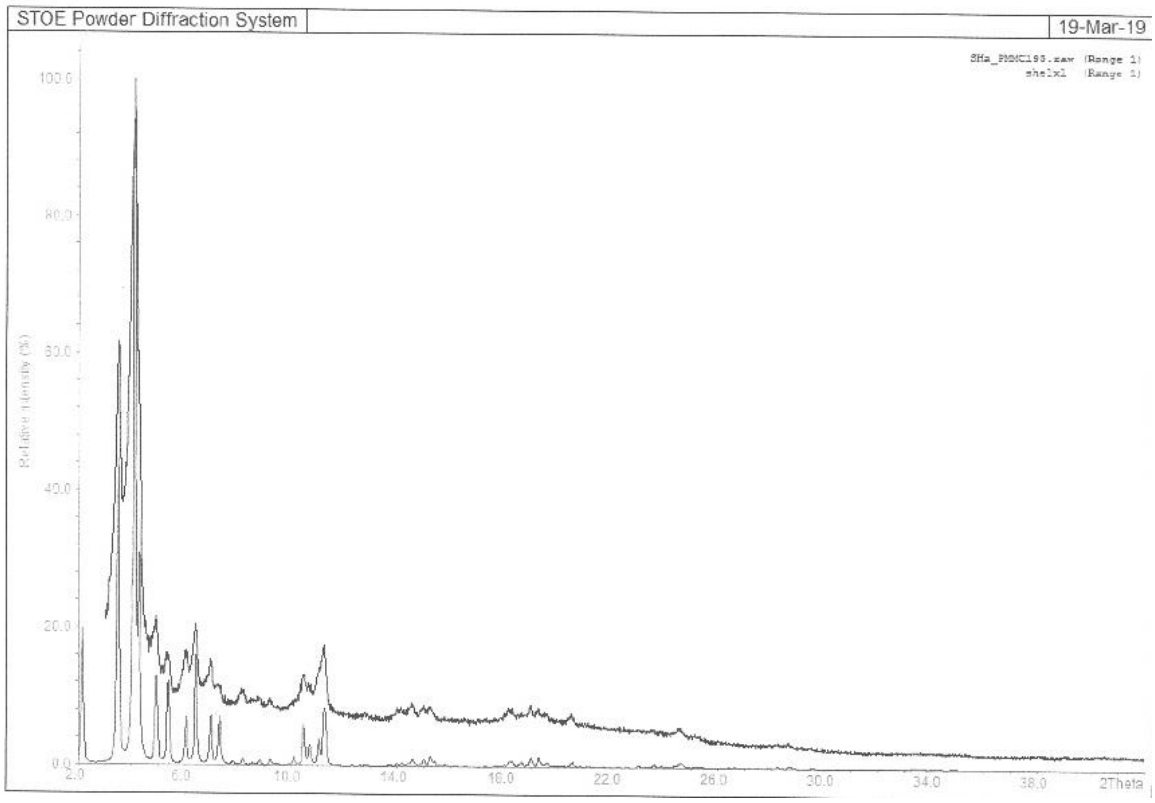

Figure 6.9S XPRD of MIL-100-Al [1]

3. SEM

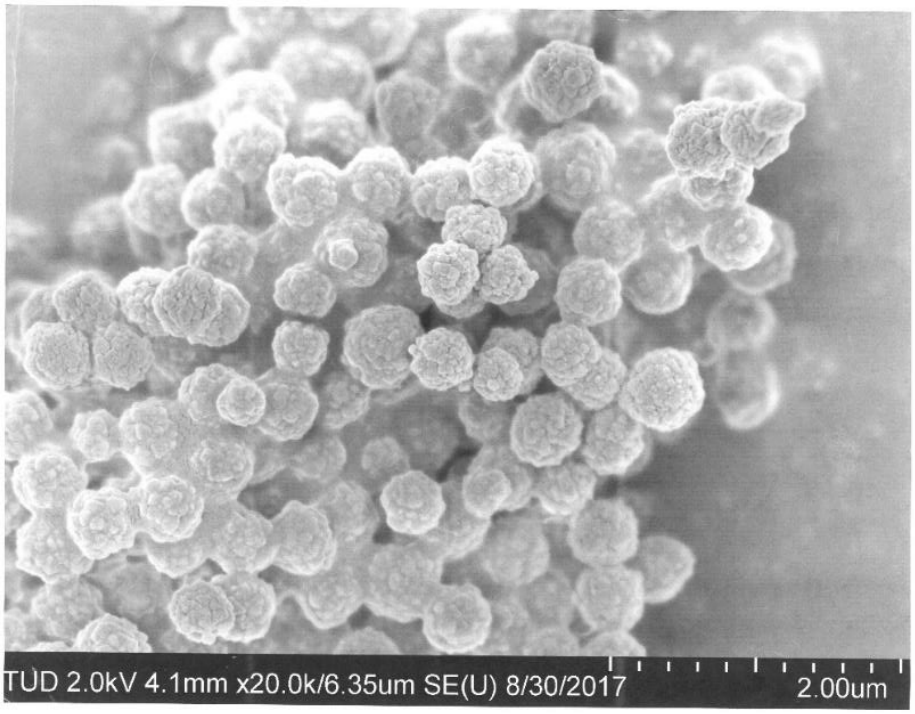

Figure 6.10S Scanning Electron Micrograph of MIL-100-Al [1]

Section III. Experimental Isotherms reported in this work

1. Sevoflurane on MIL-101-Cr

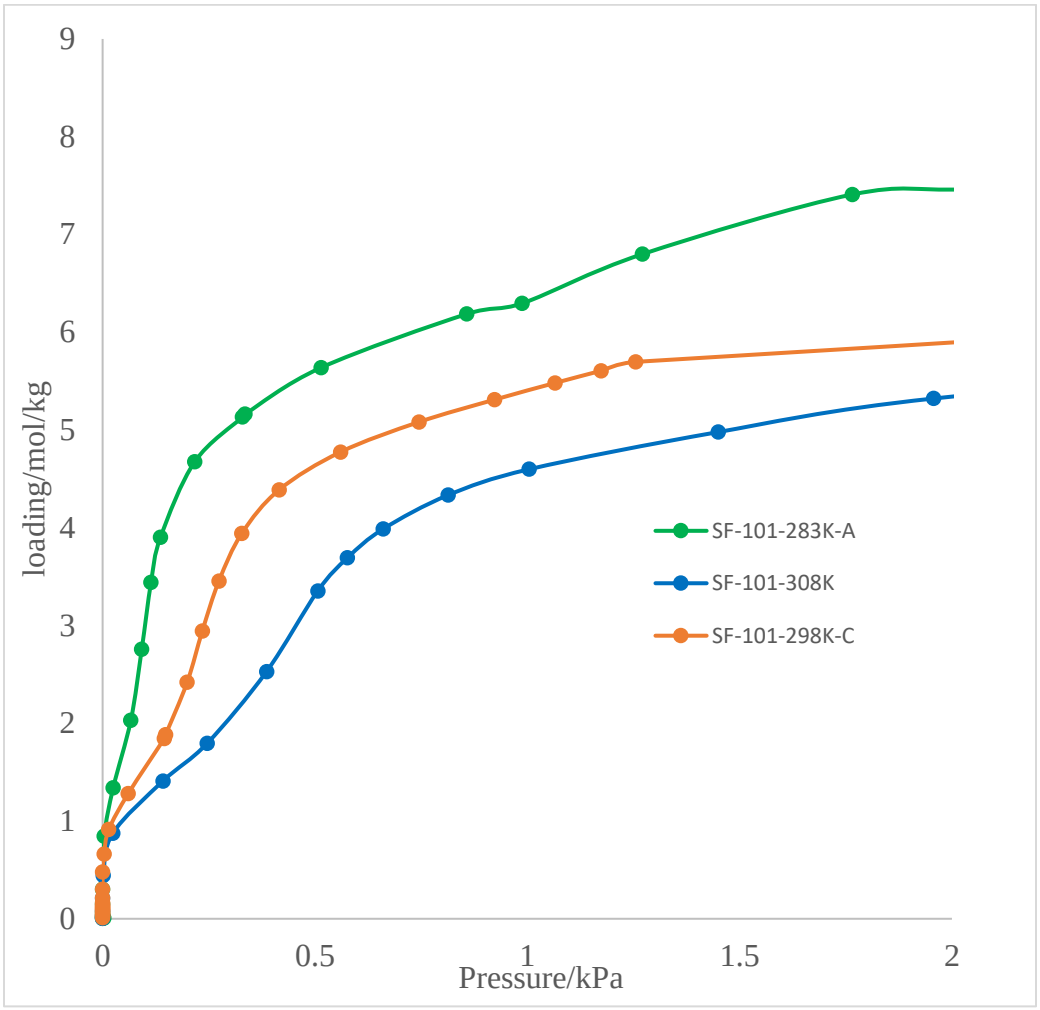

Figure 6.11S Adsorption isotherms for sevoflurane on MIL-101-Cr at three different temperatures using BELSORP

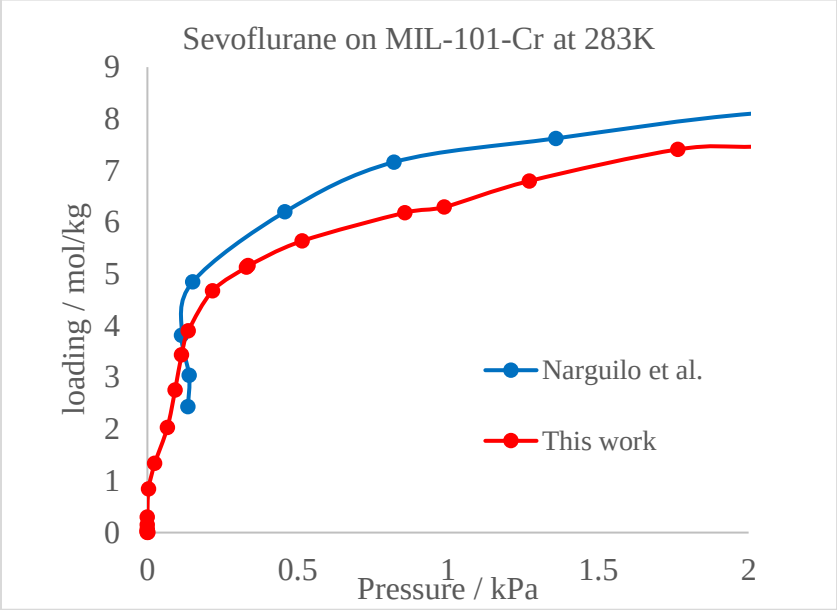

Figure 6.12aS Effect of degassing conditions on adsorption isotherms for sevoflurane on MIL-101-Cr at 283K

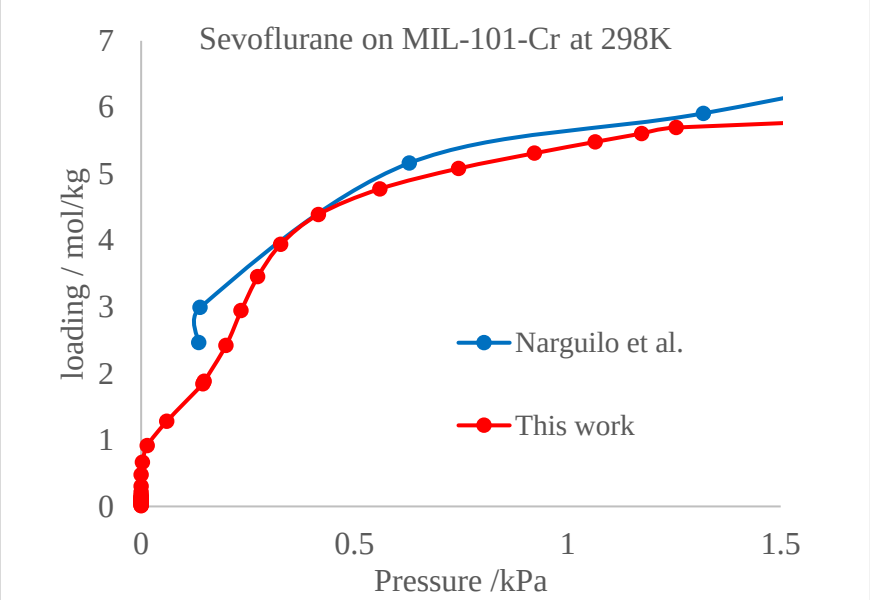

Figure 6.12bS Effect of degassing conditions on adsorption isotherms for sevoflurane on MIL-101-Cr at 298K

2. Desflurane on MIL-101-Cr

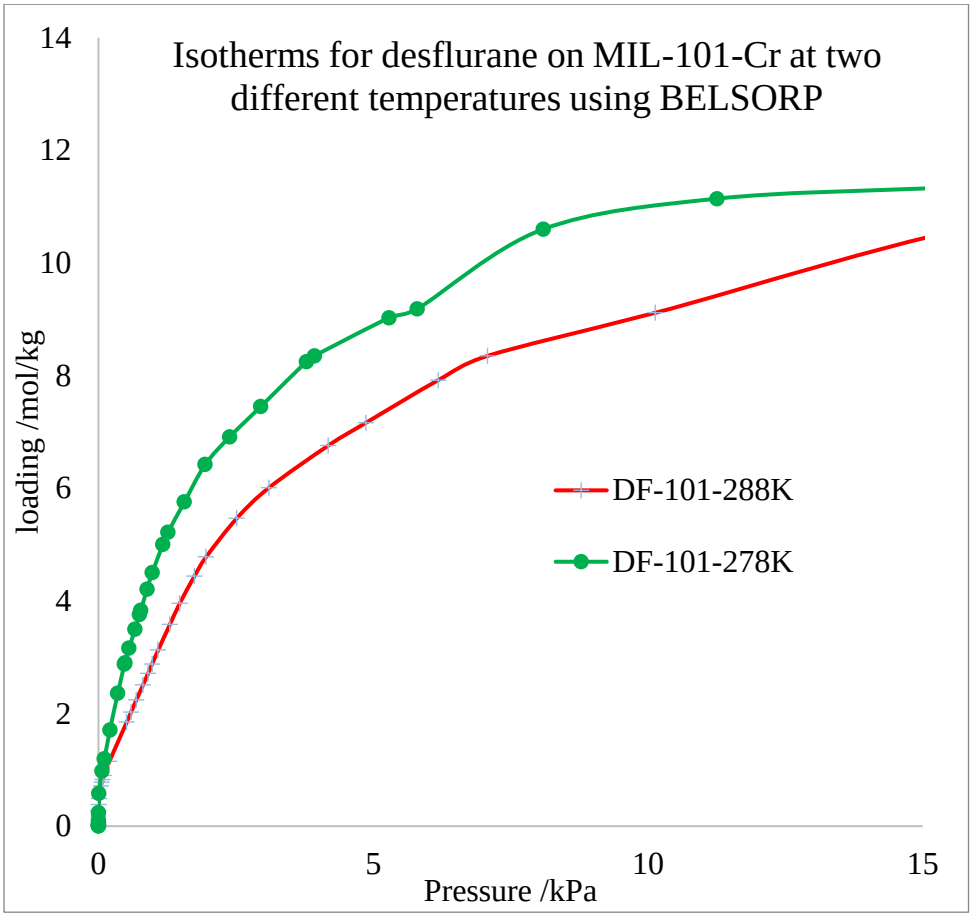

Figure 6.13S Adsorption isotherms for desflurane on MIL-101-Cr at 2 temperatures using BELSORP

3. Sevoflurane on MIl-100-Al

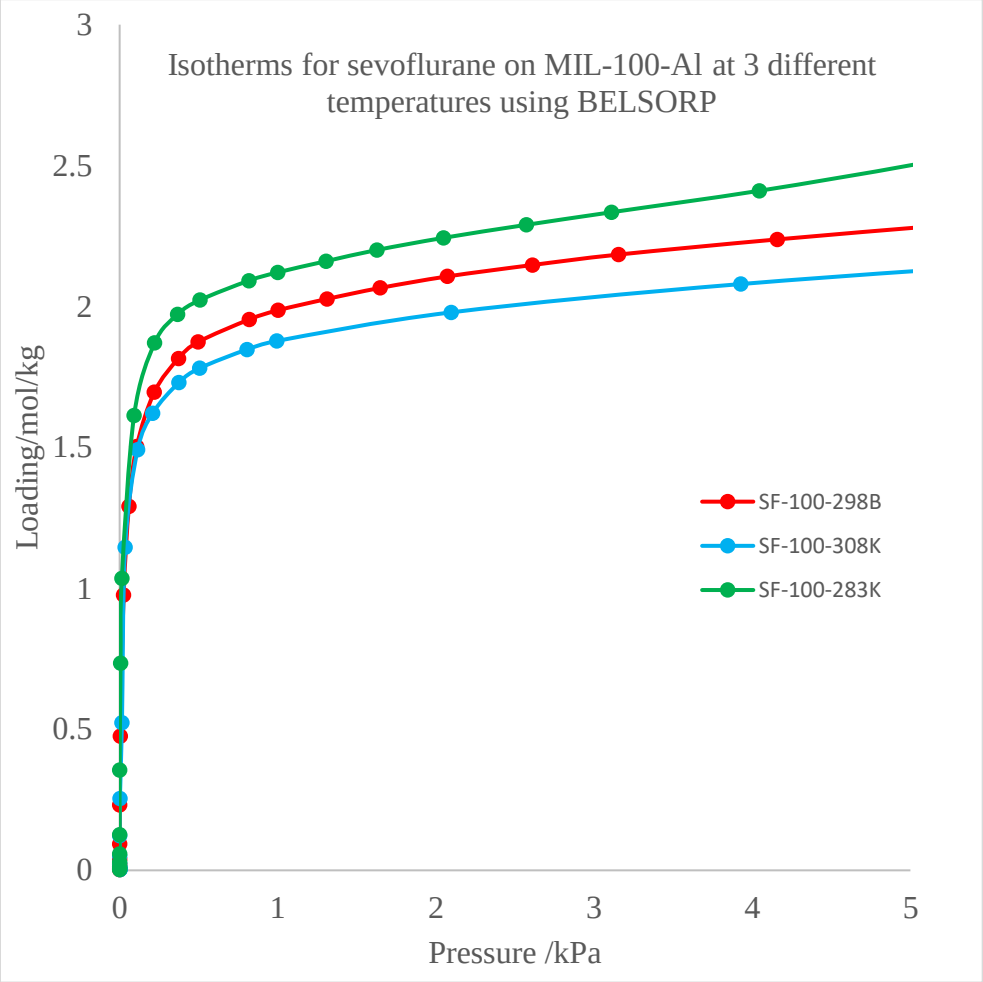

Figure 6.14S Adsorption isotherms for sevoflurane on MIL-100-Al at 3 temperatures using BELSORP

4. Desflurane on MIL-100-Al

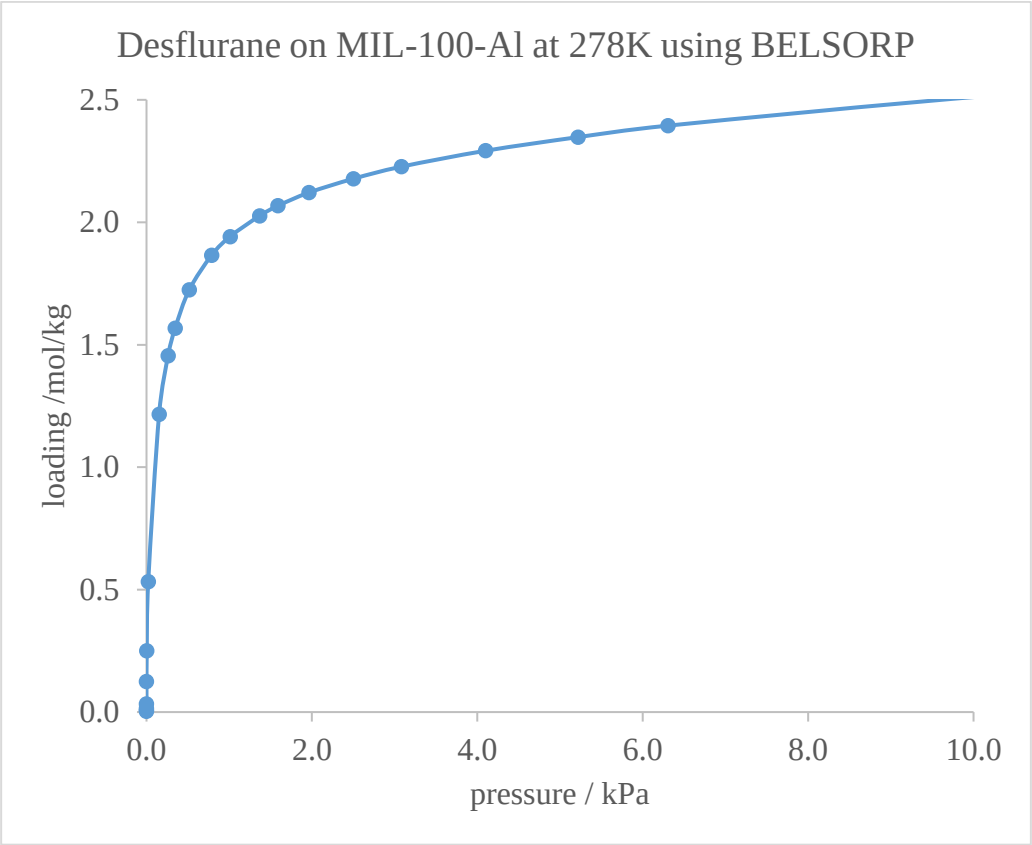

Figure 6.15S Adsorption isotherms for desflurane on MIL-100-Al at 278K using BELSORP

5. Sevoflurane on MOF-177-Zn

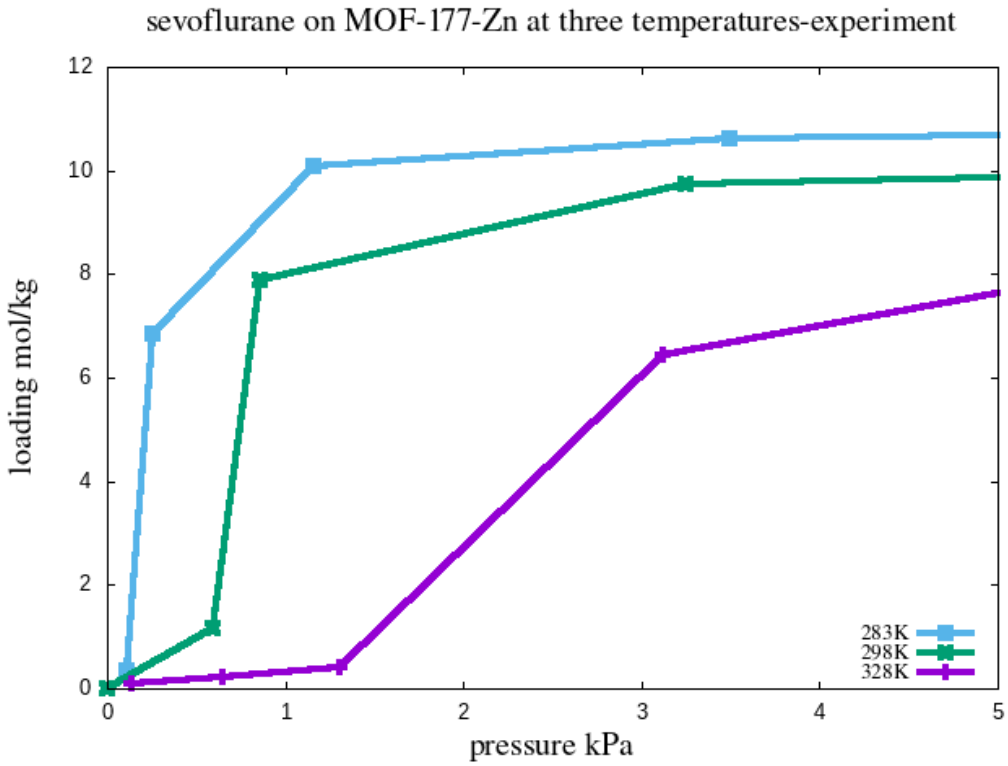

Figure 6.16S Experimental data for adsorption of sevoflurane on MOF-177-Zn at three distinct temperatures , courtesy of [132]

Section IV. Inhalation Anesthetic Agents

Table 6.1S Clinical data for IAA

	Sevoflurane	**Desflurane**
Administration concentration (induction) vol%	1-2	3-11
Administration concentration (maintenance) vol%	1-3.5	Adults: 2.5-8.5 Children: 5.2-10
Percentage metabolized	5	0.02
blood/gas partition coefficient*	0.65	0.42
MAC**	2	6-7.25
GWP (20)*** [200]	349	3714
Maximum allowable concentration [201]	UK:20 ppmv EU:50 ppmv US: 2 ppmv	UK:20 ppmv EU:50 ppmv US: 2 ppmv
Polarizability volume, 10^{-24} cm^3	9.3	7.4

*Global-warming potential

** Minimum alveolar concentration, a measure of partial pressure of the anesthetic inside the lung alveoli in equilibrium with its partial pressure in the blood. A lower MAC indicates reduced amount of anesthetic agent needed to induce anesthesia.

*** For 44 ± 7 age group in 100% O_2 atmosphere

Section V. Simulation Data

Table 6.2S Lennard-Jones parameters for studied MOF structures

Atom	σ/Å	(ε/κ_B)/K
Cr	2.69	7.55
C	3.473	47.856
O	3.033	48.158
H	2.846	7.649
F	3.093	36.483
Al	3.91105	155.998

Table 6.3S Lennard-Jones parameters and partial charges for sevoflurane used in this work[139]

Atom	σ/Å	(ε/κ_B)/K	Charge /e
F1C	2.90	67.93	-0.202
F3C	2.85	48.81	-0.048
C1F	3.38	30.19	+0.001
C3F	4.09	10.06	+0.002
CDFM	3.56	16.10	+0.003
HCF1	2.35	14.09	+0.134
HCFT	2.39	22.64	+0.300
OEF	2.94	50.32	-0.086

Table 6.4S Lennard-Jones parameters and partial charges for desflurane used in this work.[139]

Atom	σ/Å	(ε/κ_B)/K	Charge /e
C1F	3.385	30.1934	0.036
C2F	3.652	21.135	0.004
C3F	4.098	10.0644	0.008
F1C	2.904	67.93	-0.096
F2C	2.904	52.838	-0.0078
HCF1	2.351	14.09	0.211
HCF2	2.316	15.097	0.212
OEH	2.939	50.32	-0.056

$5*10^4$ equilibration cycles were followed by $1*10^6$ production cycles. A 1-1-1-unit cell was used. Translation, Rotation, Regrowth and CFSwapLambda probabilities were defined at 1:1:1:7 ratio. Ewald and cut off was 12 Å and potentials were shifted without tail correction. We used Lorentz-Berthelot mixing rule for Lennard-Jones interactions.

Table 6.5S Saturation vapor pressures for the inhalation anesthetic agents

SVP/kPa	Experimental		Molecular simulation	
Temperature/K	Sevoflurane	Desflurane	Sevoflurane	Desflurane
278.15	10.37	53.70	-	11.87
283.15	12.59	-	4.85	-
288.15	16.67	78.14	-	20.14
298.15	26.29	NA	11.16	NA
308.15	40.37	NA	20.15	NA
328.15	49.26	NA	31.5	NA

Table 6.6S The density (g cm^{-3}), surface area (m^2 g^{-1}), free volume (cm^3 g^{-1}) and porosity of the studied MOF structures [202]

Property	MIL-101(Cr)	MIL-100(Al)	MOF-177(Zn)
CSD-refcode	OCUNAK	CIGXIA	BABRII
S_{BET} (m^2/g)	3399.2	1687.790	3948
Total pore volume (cm^3/g)	1.874	0.875	1.59
Porosity	0.815	0.7233	0.8498

Table 6.7S Comparison of affinity based on isosteric heat of adsorption (kJ/mol)

	MIL-101-Cr	MIL-100-Al	MOF-177-Zn
Sevoflurane (SF)*	52	34	45
Desflurane (DF)**	50	30	N/A

*298K
**288K

Table 6.8S Comparison of uptake based on isotherm loading (mmol/g) at 2 kPa

	MIL-101-Cr	MIL-100-Al	MOF-177-Zn
Sevoflurane (SF)*	5.5	2.0	9.5
Desflurane (DF)**	6.0	2.0	N/A

*298K
**278K

Table 11.9S input file in RASPA for simulation of sevoflurane adsorption on MIL-101-Cr at 23.1 Pa and 298K

SimulationType	MonteCarlo
NumberOfEquilibrationCycles	50000
NumberOfCycles	1000000
PrintEvery	10
RestartFile	no
ContinueAfterCrash	yes
WriteBinaryRestartFileEvery	10
WriteEnergyEvery	10
ChargeMethod	Ewald
CutOff	12.0
RandomSeed	1
Forcefield	local
EwaldPrecision	1e-5
UseChargesFromCIFFile	yes
Framework 0	
FrameworkName	MIL-101-primitive
UnitCells	1 1 1
HeliumVoidFraction	0.815306
ExternalTemperature	298.15
ExternalPressure	23.1
#ComputeMolecularPressure	yes
Movies	yes
Component 0 MoleculeName	sevoflurane
MoleculeDefinition	local
BlockPockets	yes
BlockPocketsFileName	Framework_0_initial
IdealGasRosenbluthWeight	4.30563e-09
TranslationProbability	0.1
RotationProbability	0.1
RegrowProbability	0.1
CFSwapLambdaProbability	0.7
CreateNumberOfMolecules	0

Section VI. Codes

A. MATLAB subroutines for generation of a set of simulation points

1. MAIN code

```
clear all
clc
load pp
temp =transpose(278.15);
pres = 1000*transpose(pp);
imax = size(temp,1);
jmax = size(pres,2);
format long g
for i = 1:imax
for j = 1:jmax
input = [temp(i); pres(i,j)];
Tchar = num2str(temp(i));
Pchar = num2str(pres(i,j));
Tunit = 'K';
Punit = 'Pa';
foldername = strcat('GCMC-Des-',Tchar,Tunit,Pchar,Punit,'.sml');
mkdir(foldername)
texteditormethane(Tchar,Pchar)
copyfile('simulation.input',foldername)
copyfile('desflurane.def',foldername)
copyfile('pseudo_atoms.def',foldername)
copyfile('force_field_mixing_rules.def',foldername)
copyfile('submit',foldername)
%copyfile('MIL-101-Cr.block',foldername)
end
fclose('all')
end
```

2. PARSING

1. plot-prog

set xlabel "simulation progress" font "Times-Roman,15"

set ylabel "loading (mol/kg)" font "Times-Roman,15"

unset key

set title " simulation progress for adsorption of sevoflurane on MIL-101-Cr" font "Times-Roman,15"

plot [] [0:] '1.data' using ($0*10):1 w li ,\

'2.data' using ($0*10):1 w li ,\

…..

'49.data' using ($0*10):1 w li ,

set term png

set output "progress-298K.emf"

replot

set term x11

pause-1 "Hit return to continue

2. ls.sh

#!/bin/bash

awk '{print $3/46.48}' 'MCNPT-Sevo-298.15K00023.1Pa.sml.data' > 1.data

….

awk '{print $3/46.48}' 'MCNPT-Sevo-298.15K12554.6Pa.sml.data' > 42.data

ppp01

```
#!/bin/bash

for file in *.sml.data

do

tail -n 1 $file; done > plend.data

grep 'avg.' plend.data > plend.avg.data

awk '{print $9}' plend.avg.data > plend.avg.molkg.data

paste p plend.avg.molkg.data > sim.avg.data

sed -i 's/)//g' sim.avg.data
```

3. **ppp01-plot**

```
set xlabel "Pressure/ kPa" font "Times-Roman,15"

set ylabel "loading mol/kg" font "Times-Roman,15"

set title "sevoflurane on MIL-101-Cr at 298K" font "Times-Roman,15"

set style data linespoints

set key font ",15"

set key right center

set tics font ",20"

plot [0:2][0:] 'sim.data' us ($1*0.001*26.30/11.16):2 lw 4 lt 3 title "
RASPA",\

'setpoint-SF-101-298.data' us 1:2 lw 4 lt 4 title "BELSORP",

set term png

set output "isotherm-SF-MIL-101-Cr-298K.emf"
```

```
replot

set term x11

pause -1 "Hit return to continue
```

Section VII. molecular modelling of Inhalation anesthetic agents

1. sevoflurane.def

critical constants: Temperature [T], Pressure [Pa], and Acentric factor [-]

497.12

3593000

0.5119

Number Of Atoms

15

Number Of Groups

1

Alkane-group

flexible

Number Of Atoms

15

atomic positions

0 F1C	4 OEF	8 F3C	12 F3C
1 C1F	5 CDFM	9 F3C	13 F3C
2 HCF1	6 HCFT	10 F3C	14 F3C
3 HCF1	7 C3F	11 C3F	

Chiral centers Bond BondDipoles Bend UrayBradley InvBend Torsion Imp. Torsion Bond/Bond Stretch/Bend Bend/Bend Stretch/Torsion Bend/Torsion IntraVDW IntraCoulomb

0 14 0 25 0 0 24 0 0 0 0 0 0 66

66

Bond stretch: atom n1-n2, type, parameters

7 5 HARMONIC_BOND 275083.63730132232 1.539

11 5 HARMONIC_BOND 275083.63730132232 1.539

7 8 HARMONIC_BOND 399055.65861548394 1.341

7 9 HARMONIC_BOND 399055.65861548394 1.341

7 10 HARMONIC_BOND 399055.65861548394 1.341

11 12 HARMONIC_BOND 399055.65861548394 1.341

11 13 HARMONIC_BOND 399055.65861548394 1.341

11 14 HARMONIC_BOND 399055.65861548394 1.341

5 4 HARMONIC_BOND 365723.4398047164 1.408

5 6 HARMONIC_BOND 350775.82797701041 1.093

4 1 HARMONIC_BOND 367611.52121160188 1.392

1 0 HARMONIC_BOND 337168.78233422313 1.387

1 2 HARMONIC_BOND 356724.87681617407 1.089

1 3 HARMONIC_BOND 356724.87681617407 1.089

Bond bending: atom n1-n2-n3, type, parameters

7 5 6 HARMONIC_BEND 9670.862082375 106.895

11 5 6 HARMONIC_BEND 9670.862082375 106.895

7 5 4 HARMONIC_BEND 21941.353341436 108.434

11 5 4 HARMONIC_BEND 21941.353341436 108.434

7 5 11 HARMONIC_BEND 37732.364484372 113.899

5 4 1	HARMONIC_BEND	78927.881890531	116.138
5 7 8	HARMONIC_BEND	54895.150527742	110.930
5 7 9	HARMONIC_BEND	54895.150527742	110.930
5 7 10	HARMONIC_BEND	54895.150527742	110.930
5 11 12	HARMONIC_BEND	54895.150527742	110.930
5 11 13	HARMONIC_BEND	54895.150527742	110.930
5 11 1	HARMONIC_BEND	54895.150527742	110.930
4 1 2	HARMONIC_BEND	42546.157110035	109.268
4 1 3	HARMONIC_BEND	42546.157110035	109.268
4 1 0	HARMONIC_BEND	66448.051541748	110.447
4 5 6	HARMONIC_BEND	7161.812319511	112.341
0 1 2	HARMONIC_BEND	29853.968357737	107.651
0 1 3	HARMONIC_BEND	29853.968357737	107.651
2 1 3	HARMONIC_BEND	21730.001375852	112.532
8 7 9	HARMONIC_BEND	36110.992976961	107.959
8 7 10	HARMONIC_BEND	36110.992976961	107.959
9 7 10	HARMONIC_BEND	36110.992976961	107.959
12 11 13	HARMONIC_BEND	36110.992976961	107.959
12 11 14	HARMONIC_BEND	36110.992976961	107.959
13 11 14	HARMONIC_BEND	36110.992976961	107.959

Torsion: atom n1-n2-n3-n4, type, parameters

0	1	4	5	CVFF_DIHEDRAL	606.37885364	3.0	0.0
1	4	5	6	CVFF_DIHEDRAL	201.79080523	3.0	0.0

1 4 5 7 CVFF_DIHEDRAL 79.508596577 3.0 180.0

1 4 5 11 CVFF_DIHEDRAL 79.508596577 3.0 180.0

2 1 4 5 CVFF_DIHEDRAL 230.47428628 1.0 180.0

3 1 4 5 CVFF_DIHEDRAL 230.47428628 1.0 180.0

4 5 7 8 CVFF_DIHEDRAL 685.887450217 3.0 0.0

4 5 7 9 CVFF_DIHEDRAL 685.887450217 3.0 0.0

4 5 7 10 CVFF_DIHEDRAL 685.887450217 3.0 0.0

4 5 11 12 CVFF_DIHEDRAL 685.887450217 3.0 0.0

4 5 11 13 CVFF_DIHEDRAL 685.887450217 3.0 0.0

4 5 11 14 CVFF_DIHEDRAL 685.887450217 3.0 0.0

6 5 7 8 CVFF_DIHEDRAL 58.876618984 1.0 180.0

6 5 7 9 CVFF_DIHEDRAL 58.876618984 1.0 180.0

6 5 7 10 CVFF_DIHEDRAL 58.876618984 1.0 180.0

6 5 11 12 CVFF_DIHEDRAL 58.876618984 1.0 180.0

6 5 11 13 CVFF_DIHEDRAL 58.876618984 1.0 180.0

6 5 11 14 CVFF_DIHEDRAL 58.876618984 1.0 180.0

7 5 11 12 CVFF_DIHEDRAL 616.94645192 3.0 180.0

7 5 11 13 CVFF_DIHEDRAL 616.94645192 3.0 180.0

7 5 11 14 CVFF_DIHEDRAL 616.94645192 3.0 180.0

8 7 5 11 CVFF_DIHEDRAL 616.94645192 3.0 180.0

9 7 5 11 CVFF_DIHEDRAL 616.94645192 3.0 180.0

10 7 5 11 CVFF_DIHEDRAL 616.94645192 3.0 180.0

Intra VDW: atom n1-n2

0 5
0 6
0 7
0 8
0 9
0 10
0 11
0 12
0 13
0 14
1 6
1 7
1 8
1 9
1 10
1 11
1 12
1 13
1 14
2 5
2 6
2 7
2 8
2 9
2 10
2 11
2 12
2 13
2 14
3 5
3 6
3 7
3 8
3 9
3 10
3 11
3 12
3 13
3 14
4 8
4 9
4 10
4 12
4 13
4 14
6 8
6 9
6 10
6 12
6 13
6 14
7 12
7 13
7 14
8 11
8 12
8 13
8 14
9 11
9 12
9 13
9 14
10 11
10 12
10 13
10 14
Intra Charge:
atom n1-n2
0 5

0 6
0 7
0 8
0 9
0 10
0 11
0 12
0 13
0 14
1 6
1 7
1 8
1 9
1 10
1 11
1 12
1 13
1 14
2 5
2 6
2 7
2 8
2 9
2 10
2 11
2 12
2 13
2 14
3 5
3 6
3 7
3 8
3 9
3 10
3 11
3 12
3 13
3 14
4 8
4 9
4 10
4 12
4 13
4 14
6 8
6 9
6 10
6 12
6 13
6 14
7 12
7 13
7 14
8 11
8 12
8 13
8 14
9 11
9 12
9 13
9 14
10 11
10 12
10 13
10 14
Number of config moves
5
fragment

5 1 0 2 3 5 5 4 6 7 11 5 11 5 12 13

4 5 7 5 8 9

3 4 1 5 10

2.desflurane.def

critical constants: Temperature [T], Pressure [Pa], and Acentric factor [-]

496.63

3688000

0.5

Number Of Atoms

12

Number Of groups

1

des-group

flexible

number of atoms

12

atomic positions

0 H_CF2d	4 O_EHd	8 C_3Fd
1 C_2Fd	5 C_1Fd	9 F_3Cd
2 F_2Cd	6 F_1Cd	10 F_3Cd
3 F_2Cd	7 H_CF1d	11 F_3Cd

Chiral centers

Bond BondDipoles Bend UrayBradley InvBend Torsion Imp.Torsion Bond/Bond Stretch/Bend Bend/Bend Stretch/Torsion Bend/Torsion IntraVDW IntraCoulomb

0 11 0 19 0 0 16 0 0 0 0 0 0 36 36

Bond stretch: atom n1-n2, type, parameters

0 1 HARMONIC_BOND 349153.02 1.093

1 2 HARMONIC_BOND 394009.28 1.347

1 3 HARMONIC_BOND 394009.28 1.347

1 4 HARMONIC_BOND 369725.77 1.382

4 5 HARMONIC_BOND 386173.10 1.381

5 6 HARMONIC_BOND 344903.81 1.095

5 7 HARMONIC_BOND 365809.69 1.371

5 8 HARMONIC_BOND 281905.36 1.537

8 9 HARMONIC_BOND 406766.99 1.338

8 10 HARMONIC_BOND 406766.99 1.338

8 11 HARMONIC_BOND 406766.99 1.338

Bond bending: atom n1-n2-n3, type, parameters

0 1 2 HARMONIC_BEND 31405.12 109.347

0 1 3 HARMONIC_BEND 31405.12 109.347

0 1 4 HARMONIC_BEND 43599.21 112.769

1 4 5 HARMONIC_BEND 75915.17 116.527

2 1 3 HARMONIC_BEND 48486.51 107.878

2 1 4 HARMONIC_BEND 69516.19 108.691

3 1 4 HARMONIC_BEND 69516.19 108.691

4 5 6 HARMONIC_BEND 17734.57 112.451

4 5 7 HARMONIC_BEND 24809.89 111.31

4 5 8 HARMONIC_BEND 49315.82 107.727

5 8 9 HARMONIC_BEND 53348.65 110.352

5 8 10 HARMONIC_BEND 53348.65 110.352

5 8 11 HARMONIC_BEND 53348.65 110.352

6 5 7 HARMONIC_BEND 10620.01 107.836

6 5 8 HARMONIC_BEND 21258.14 109.222

7 5 8 HARMONIC_BEND 31621.51 108.203

9 8 10 HARMONIC_BEND 34953.85 108.567

9 8 11 HARMONIC_BEND 34953.85 108.567

10 8 11 HARMONIC_BEND 34953.85 108.567

#Torsion: atom n1-n2-n3-n4, type, parameters

0 1 4 5 CVFF_DIHEDRAL 1136.78 1 0

1 4 5 6 CVFF_DIHEDRAL 746.279 1 180

1 4 5 6 CVFF_DIHEDRAL 233.495 4 0

1 4 5 7 CVFF_DIHEDRAL 141.406 3 180

1 4 5 8 CVFF_DIHEDRAL 1251.01 1 0

2 1 4 5 CVFF_DIHEDRAL 1334.55 1 0

3 1 4 5 CVFF_DIHEDRAL 1334.55 1 0

4 5 8 9 CVFF_DIHEDRAL 848.433 2 180

4 5 8 10 CVFF_DIHEDRAL 848.433 2 180

4 5 8 11 CVFF_DIHEDRAL 848.433 2 180

6 5 8 9 CVFF_DIHEDRAL 110.206 3 0

6 5 8 10 CVFF_DIHEDRAL 110.206 3 0

6 5 8 11 CVFF_DIHEDRAL 110.206 3 0

7 5 8 9 CVFF_DIHEDRAL 12.5806 3 180

7 5 8 10 CVFF_DIHEDRAL 12.5806 3 180

7 5 8 11 CVFF_DIHEDRAL 12.5806 3 180

#Intra VDW:

atom n1-n2

0 5

0 6

0 7

0 8

0 9

0 10

0 11

1 6

1 7

1 8

1 9

1 10

1 11

2 5

2 6

2 7

2 8

2 9

2 10

2 11

3 5

3 6

3 7

3 8

3 9

3 10

3 11

4 9

4 10

4 11

6 9

6 10

6 11

7 9

7 10

7 11

#Intra Coulomb:

atom n1-n2

0 5

0 6

0 7

0 8

0 9

0 10

0 11

1 6

1 7

1 8

1 9

1 10

1 11

2 5

2 6

2 7

2 8

2 9

2 10

2 11

5

3 6

3 7

3 8

3 9

3 10

3 11

4 9

4 10

4 11

6 9

6 10

6 11

7 9

7 10

7 11

#Number of config moves

4

#fragments

5 1 2 0 3 4

3 4 1 5

5 5 4 6 7 8

5 8 5 9 10

Appendix D. Supplementary Information from Chapter 7

Section I. Protocols for modification of the CIF files

A large number of CIFs for synthesized/hypothetical MOFs are stored in databases such as COREMOF2019[37], and ARC-MOF[12]. However, things become complicated if a new CIF file for a proposed modification is needed. That is because CIFs are usually deduced from experimental Single Crystal Xray Diffraction (SCXRD) which is different from Powder XRD. For SCXRD, the crystal size should be large enough. Now, if the idea is to predict a structure prior to actual synthesis as the case with molecular simulation of a given proposed structure, a different approach is needed. The subsections below show the measures taken for obtaining the CIFs used in Chapters 7 and 8.

1. Organic linker modification

For the case of functionalization of the benzene rings of the organic linkers in MIL-101-Cr with NO_2 and NH_2 functional groups respectively, the recently developed MOFUN[104] and/or POREMATMODE [78]were used. The basic algorithm of both methods is based on replacing a given fraction of the linker with a desired fraction containing NO_2 or NH_2 in the case of this study. Once the new CIF was created, the CIF was geometrically optimized using software such as $DMOL^3$ as part of BOVIA Materials Studio[76].Partial charges were determined using ChEq tool in RASPA.

2. Metal-cluster node modification

For the case of metal-cluster node modification, as in the case of NH_3 grafting, a different approach was adopted. In the node database of ToBaCCo[147] software , the node corresponding to the node of MIL-101-Cr was found and then it modified using the

Avogadro software. Next, ToBaCCo was run. The generated CIF was cubic P1. In order to reduce this new MOF to the irreducible primitive CIF an option in Materials studio was used. The remaining procedure regarding geometric optimization and partial charge assignment was the same as described in subsection 1 above.

Appendix E. Supplementary Information from Chapter 8

Section I. Characterization results

1. PXRD pattern

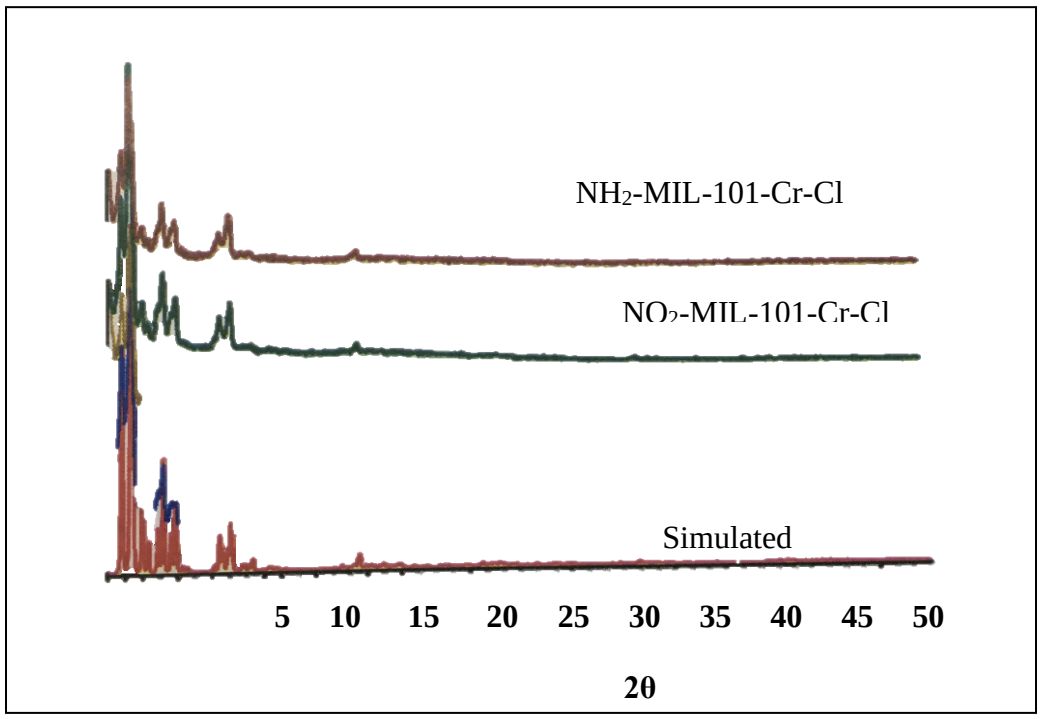

Figure 8.1S PXRD of Cr-MOF-2 and its derivatives

2. SEM Images of Cr-MOF-2

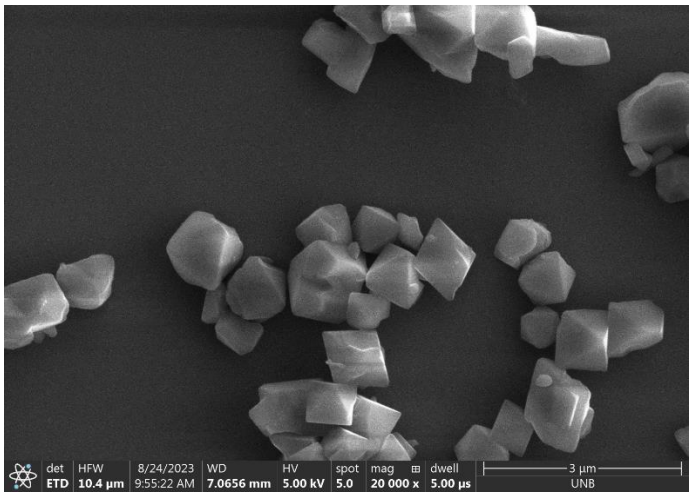

Figure 8.2aS SEM of Cr-MOF-2

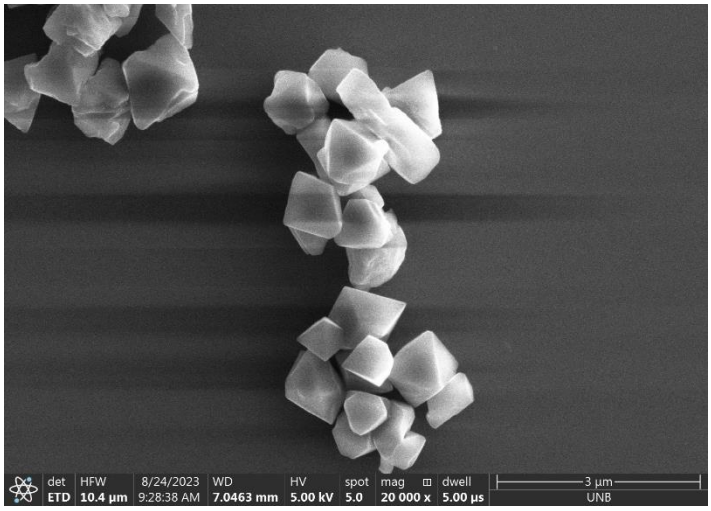

Figure 8.2bS SEM of Cr-MOF-2@NH3

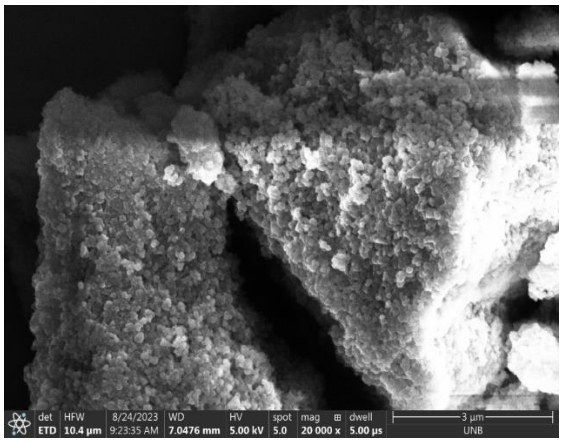

Figure 8.2cS SEM of NO_2-MIL-101-Cr-Cl

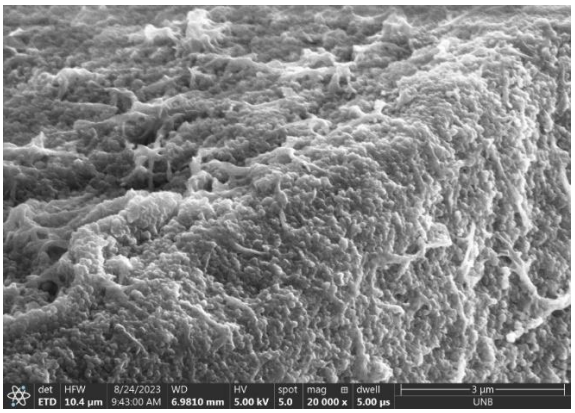

Figure 8.2dS SEM of NH_2-MIL-101-Cr-Cl

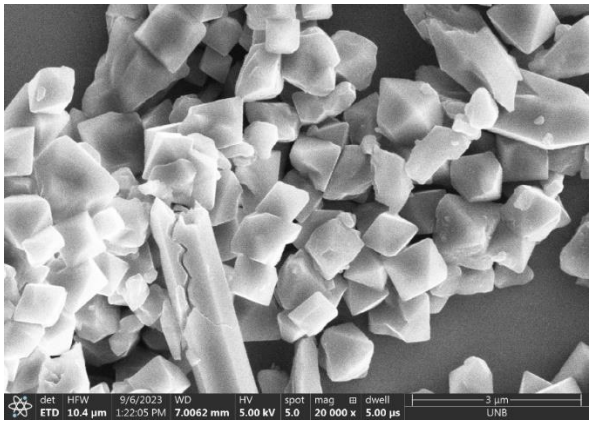

Figure 8.2eS SEM of Cr-MOF-2-Cl

3.TGA

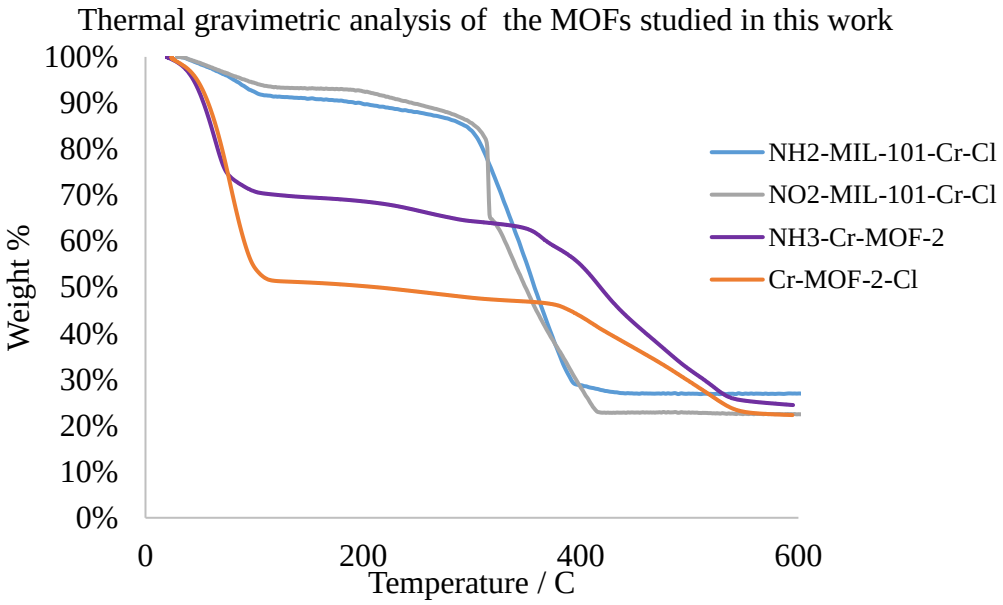

Figure 8.3S TGA of the MOFs studied in this work

4.DRIFT-IR

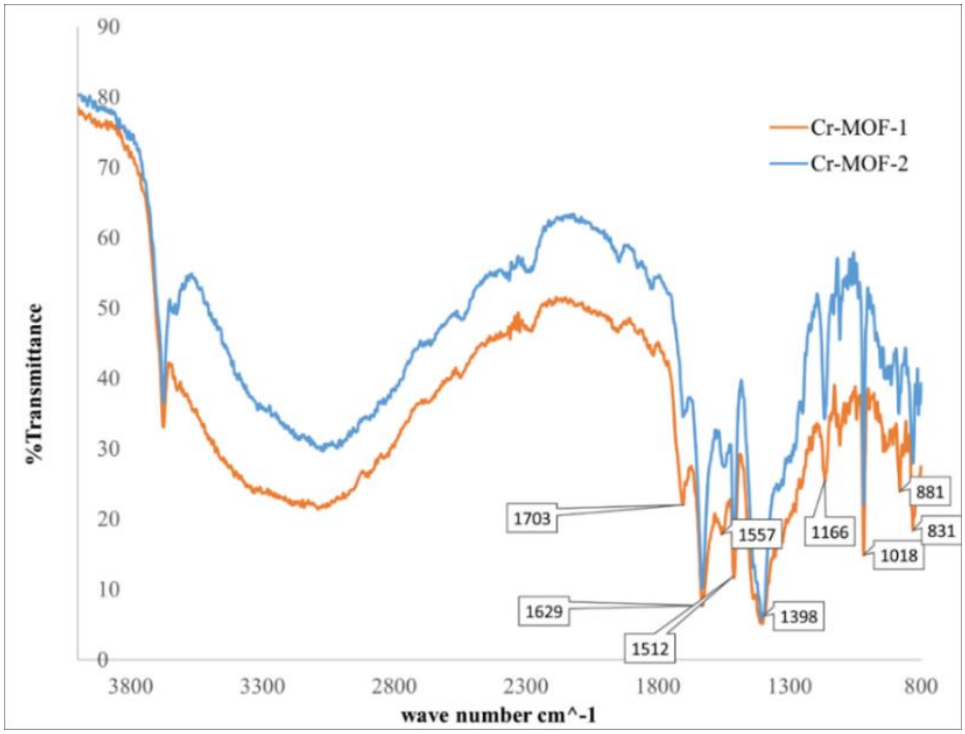

Figure 8.4aS DRIFT-IR spectra of Cr-MOF-1 and Cr-MOF-2 The results match published data

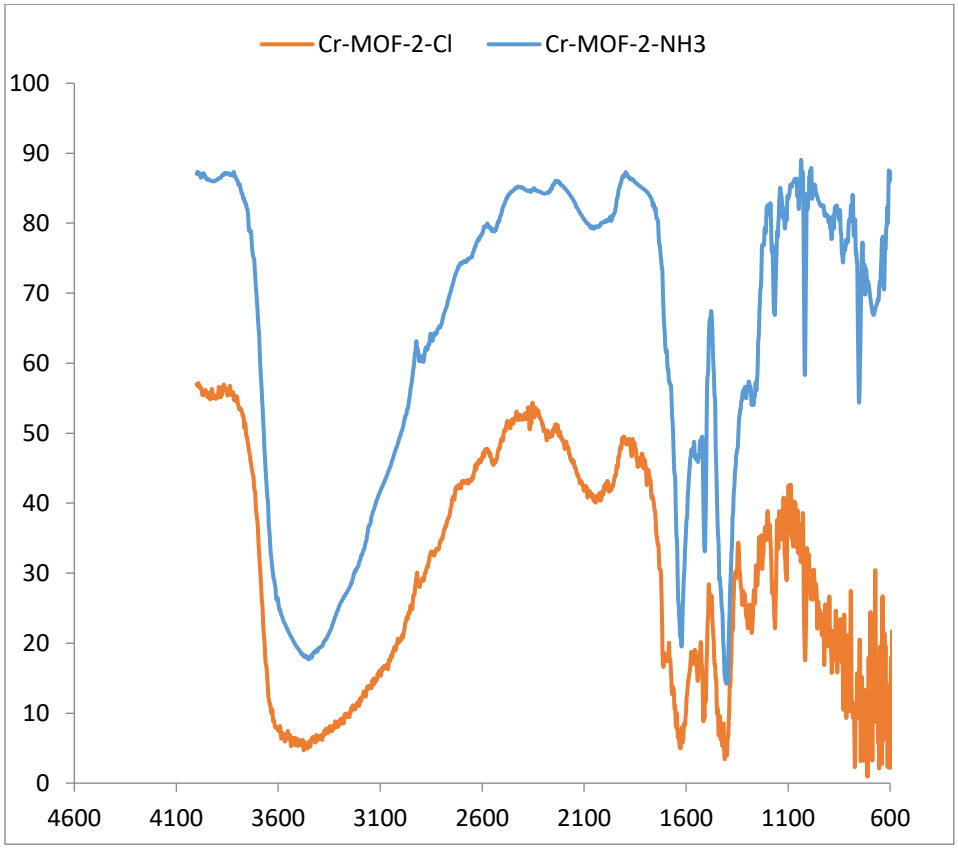

Figure 8.4bS DRIFT-IR spectra of Cr-MOF-2-Cl vs Cr-MOF-2@NH_3

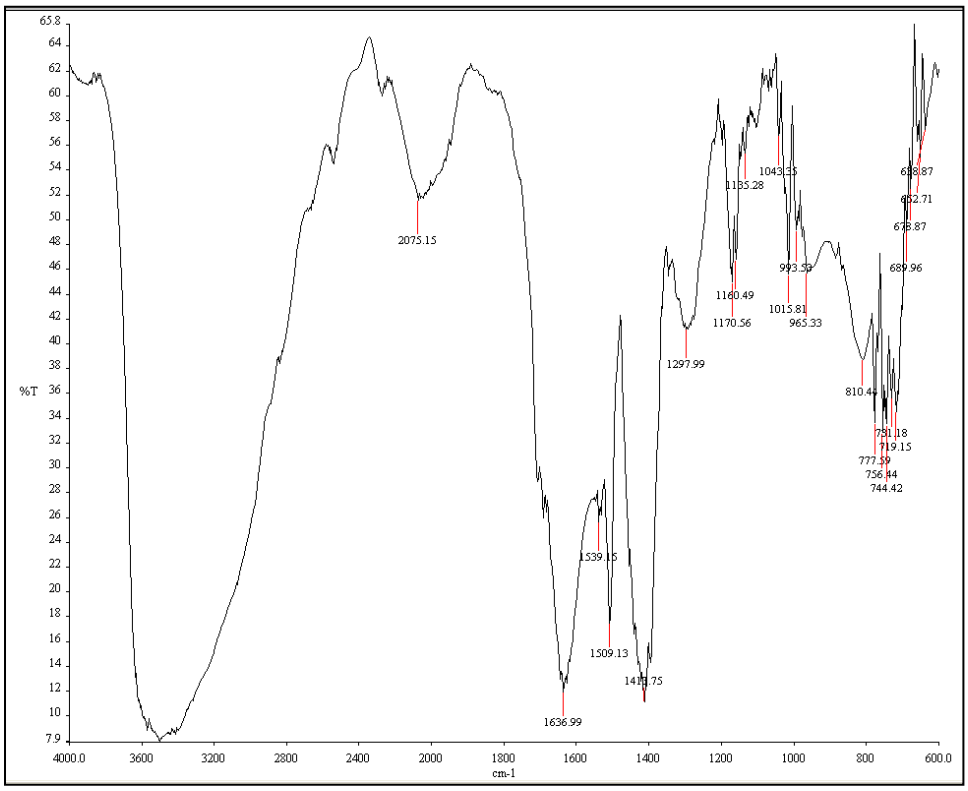

Figure 8.4cS DRIFT-IR spectra of Cr-MOF-2-Cl

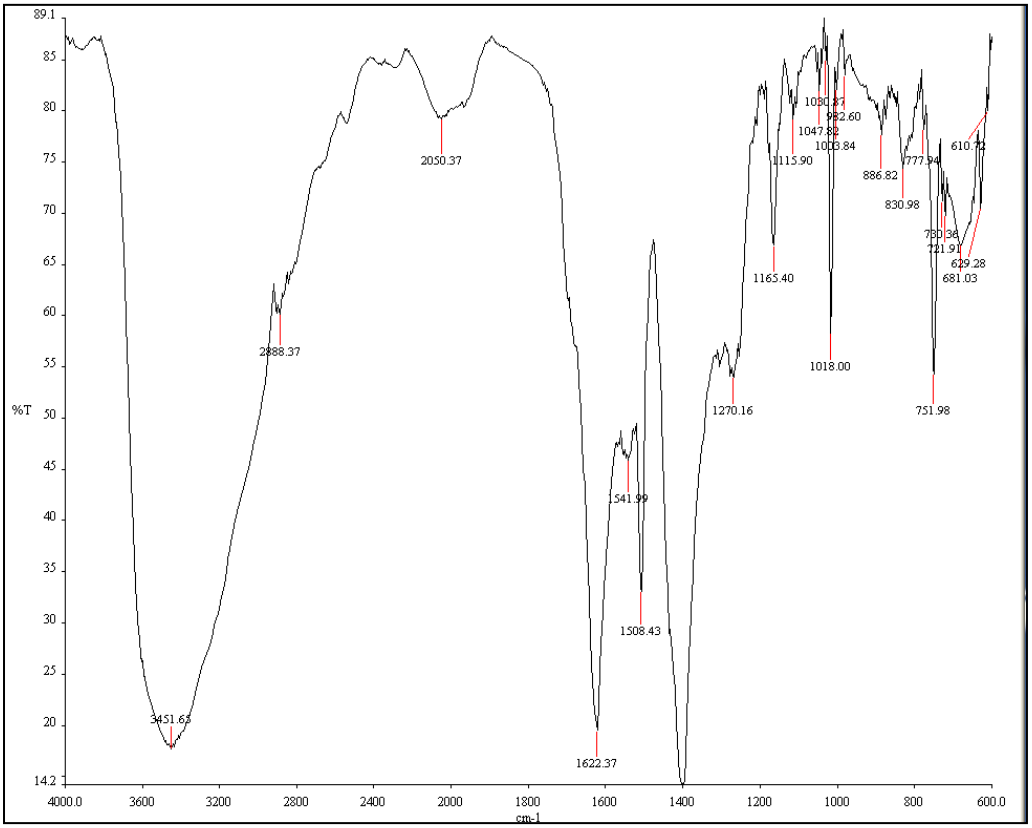

Figure 8.4dS DRIFT-IR spectra of Cr-MOF-2@NH_3

5. Specific surface area and total pore volume

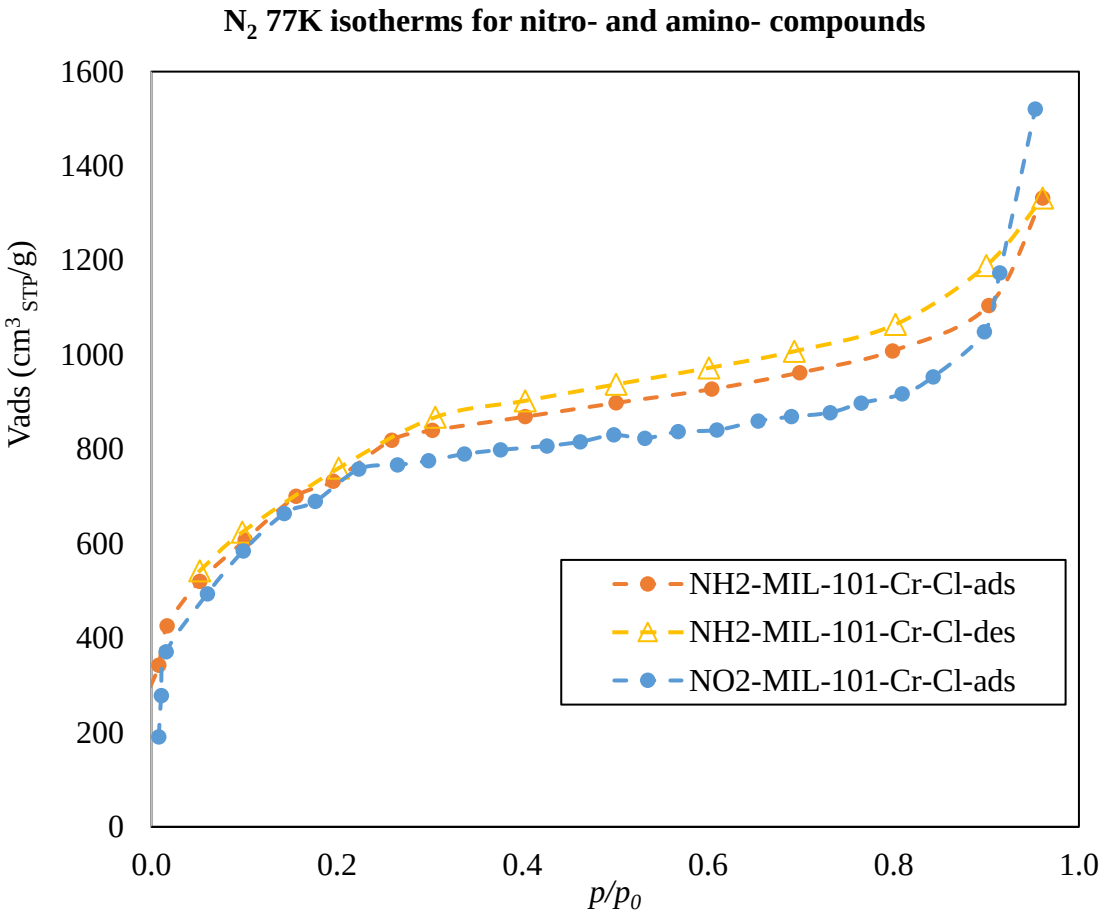

Figure 8.5aS Comparison of N_2 77K isotherms for amino- and nitro-substituted MIL-101-Cr-Cl (Source: TU Dresden)

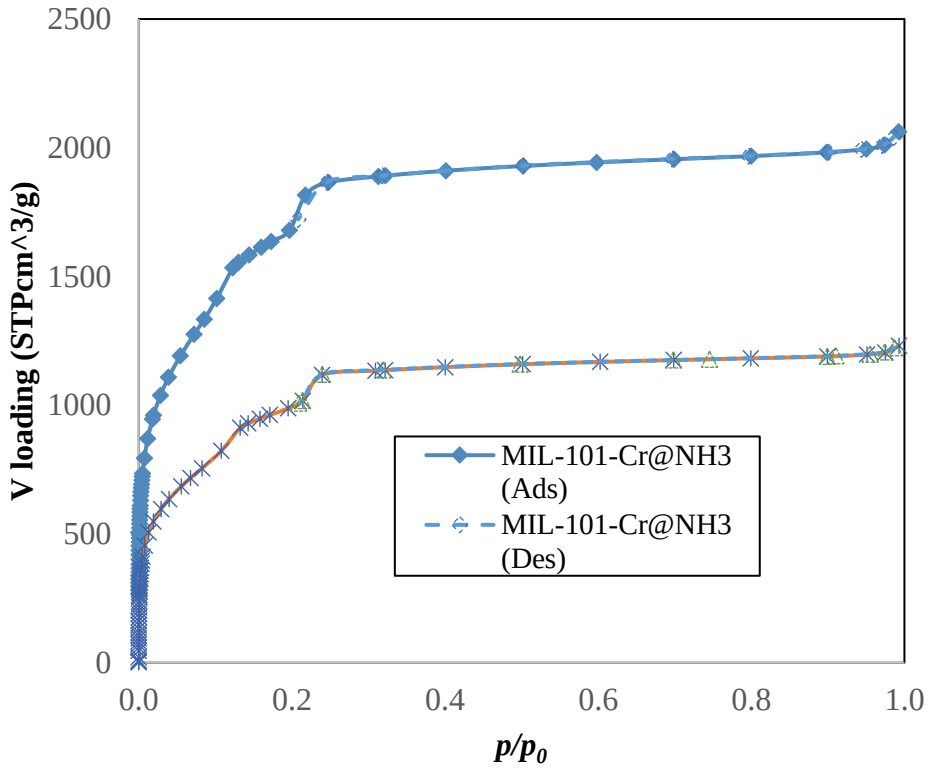

Figure 8.5bS Comparison of N_2 77K isotherm for MIL-101-Cr@Cl and MIL-101-Cr@NH_3

Table 8.1S Surface area ($m^2\ g^{-1}$), pore volume ($cm^3\ g^{-1}$) and porosity of the studied MOF structures

MOF	S_{BET} (m^2/g)	Total pore volume (cm^3/g)
MIL-101-Cr-F	3670	1.89
NH_2-MIL-101-Cl	1998	1.61
NO_2-MIL-101-Cl	1684	1.45
MIL-101-Cr -Cl	1760	1.07
MIL-101-Cr @NH_3	6345	2.00

Section II. Simulation Data

Table 8.2S Lennard-Jones parameters for studied MOF structures

Atom	σ/Å	(ε/κ_B)/K
Cr	2.69	7.55
C	3.473	47.856
O	3.033	48.158
H	2.846	7.649
F	3.093	36.483
Cl	142.562	3.51932
N-NO_2	38.949	3.262
N-NH_2	38.949	3.262
N-NH_3	38.949	3.262

Table8.3S Lennard-Jones parameters and partial charges for sevoflurane used in this work.

Atom	σ/Å	(ε/κ_B)/K	Charge /e
F1C	2.90	67.93	-0.202
F3C	2.85	48.81	-0.048
C1F	3.38	30.19	+0.001
C3F	4.09	10.06	+0.002
CDFM	3.56	16.10	+0.003
HCF1	2.35	14.09	+0.134
HCFT	2.39	22.64	+0.300
OEF	2.94	50.32	-0.086

Table 8.4S Lennard-Jones parameters and partial charges for desflurane used in this work.[139]

Atom	σ/Å	(ε/κ_B)/K	Charge /e
C1F	3.385	30.1934	0.036
C2F	3.652	21.135	0.004
C3F	4.098	10.0644	0.008
F1C	2.904	67.93	-0.096
F2C	2.904	52.838	-0.0078
HCF1	2.351	14.09	0.211
HCF2	2.316	15.097	0.212
OEH	2.939	50.32	-0.056

Table 8.5S Saturation vapor pressures for the inhalation anesthetic agents

SVP/kPa	**Experimental**		**Molecular simulation**	
Temperature/K	**Sevoflurane**	**Desflurane**	**Sevoflurane**	**Desflurane**
278.15	10.37	53.70	-	11.87
283.15	12.59	-	4.85	-
288.15	16.67	78.14	-	20.14
298.15	26.29	NA	11.16	NA
308.15	40.37	NA	20.15	NA
328.15	49.26	NA	31.5	NA

Table 8.6S Comparison of uptake based on isotherm loading (mmol/g) at 1 kPa

MOF	**Sevoflurane (SF)***	**Desflurane (DF)****
MIL-101-Cr-F	4.0	3.3
NH_2-MIL-101-Cl	6.8	6.1
NO_2-MIL-101-Cl	5.3	4.4
MIL-101-Cr-Cl	3.7	5.9
MIL-101-Cr@NH_3	7.1	5.7

*298K
**278K

Section III: Synthesis procedures

A. Synthesis of NO_2-MIL-101-Cr-Cl

A reaction approach containing freshly precipitated chromium hydroxide, nitro-terephthalic acid, HCl and water at 180 °C for 6 days. Then, the solid was separated by centrifugation. The as-made product was suspended in hot water overnight to remove remaining linker. The DMF was removed by extraction with ethanol for 24 h before the sample was air-dried at 150 °C. Full activation shall be done at 150-180 °C in vacuum.

B. Synthesis of NH_2-MIL-101-Cr-Cl

One part of the NO_2-MIL-101-Cr-Cl sample synthesized above used in reduction approach $SnCl_2$ in ethanol to give the desired product. The remaining Sn residuals were washed out with concentrated HCl before the sample was water and ethanol again and dried once more at 150 °C. Full activation shall be done at 150-180 °C in vacuum.

C. Synthesis of Cr-MOF-2-Cl

One part of Cr-MOF-2 was added to a 1M NaCl solution. The mixture was stirred for 2h at room temperature, the solid was filtered off, washed by acetone and finally dried overnight at 80 °C.

D. Synthesis of Cr-MOF-2@NH_3

One part of Cr-MOF-2 was dried at 150 °C to remove the free and coordinated water inside the structure. Then NH_3 was produced by the reaction of NaOH and NH_4Cl and introduced into the jar containing the dissolved Cr-MOF-2 sample.

Section IV: Volumetric adsorption setup

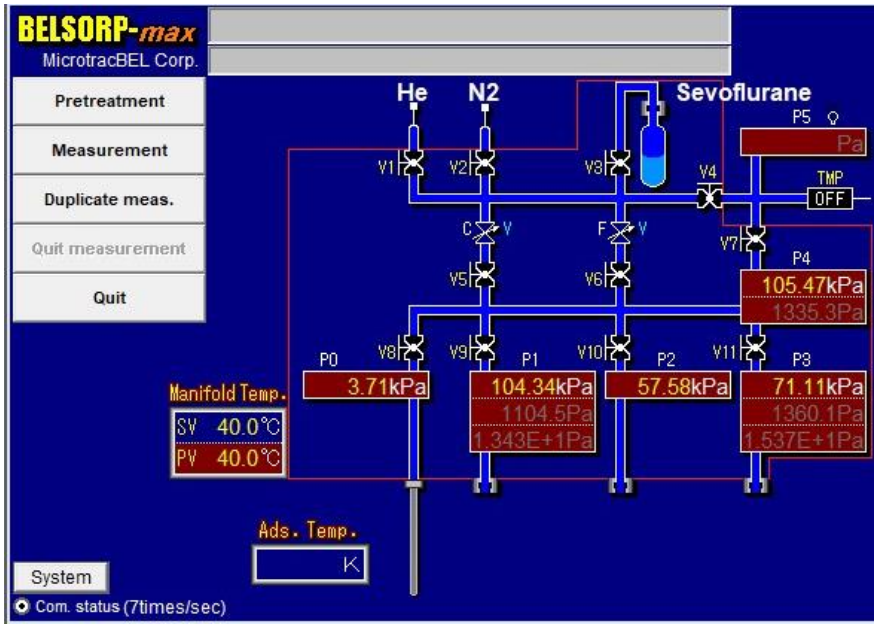

Figure 8.6S Experimental Adsorption set up as shown in BELSORP-Max measurement software screen

Appendix F. Supplementary Information from Chapter 9

Section I. Data analysis for ZLC isotherm generation

The raw data from the mass spectrometer is processed as follows. A semi-log graph of $\mathbf{c/c_0}$ vs Ft should be prepared where $\mathbf{c/c_0} = \frac{\sigma_t - \sigma_{min}}{\sigma_{max} - \sigma_{min}}$, where $\boldsymbol{\sigma_t}, \boldsymbol{\sigma_{min}}$ and $\boldsymbol{\sigma_{max}}$ refer to the detector signal at time t, minimum and maximum , respectively. The graphs from two different flow rates are chosen. This graph should overlap. If so, the higher flow will be chosen. Otherwise, the test was repeated at a lower flow rate. It is preferred to run the tests at the threshold flow rate where the maximum possible flow rate can be used to ensure sufficient accuracy of the concentration values and the detector signal to noise ratio. Once the desired linear desorption adsorption is found, Equation 9.3, and a numerical method such as trapezoid integration rule was used to calculate the complete adsorption isotherm.

Section II. ZLC response curves and adsorption isotherms for selected permanent gases on zeolites

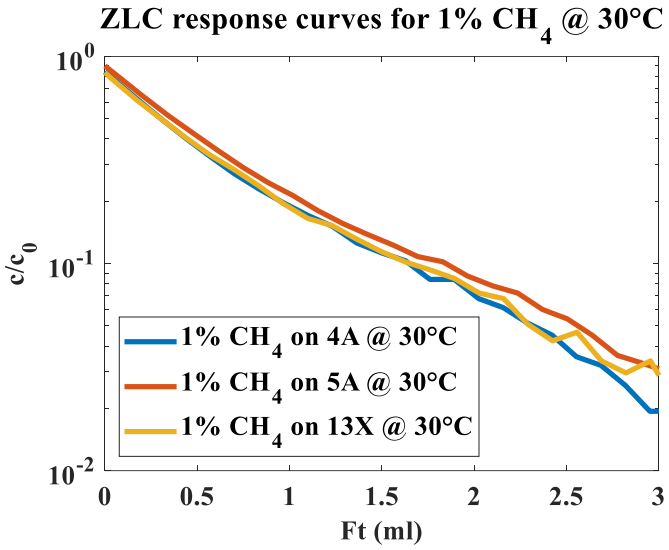

Figure 11.1S ZLC response curve for 1% CH_4 at 30°C for zeolites 4A, 5A and 13X

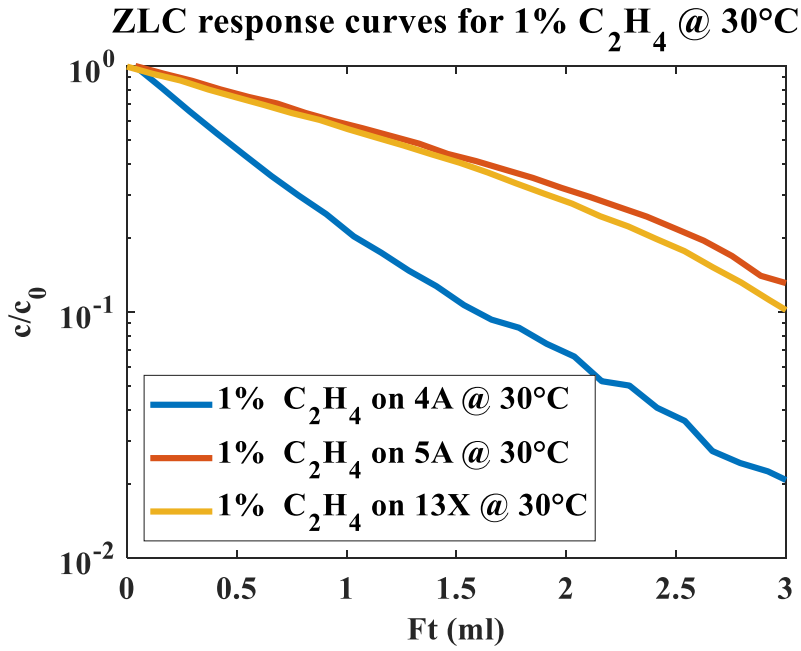

Figure 9.2S ZLC reponse curve for 1% C_2H_4 at 30°C for zeolites 4A, 5A and 13X

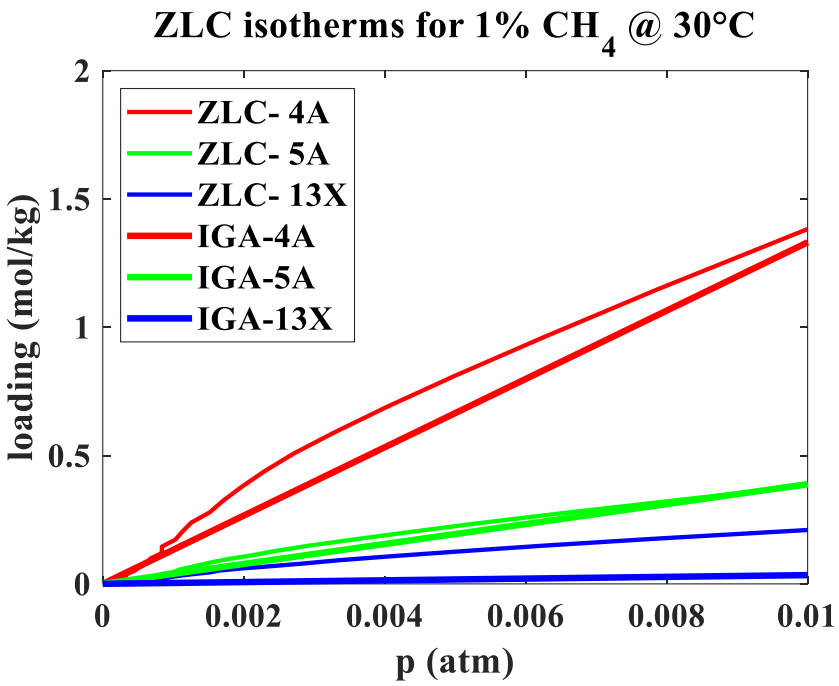

Figure 11.3S ZLC adsorption isotherms for 1% CH_4 at 30°C for zeolites 4A, 5A and 13X in comparison to IGA gravimetric results

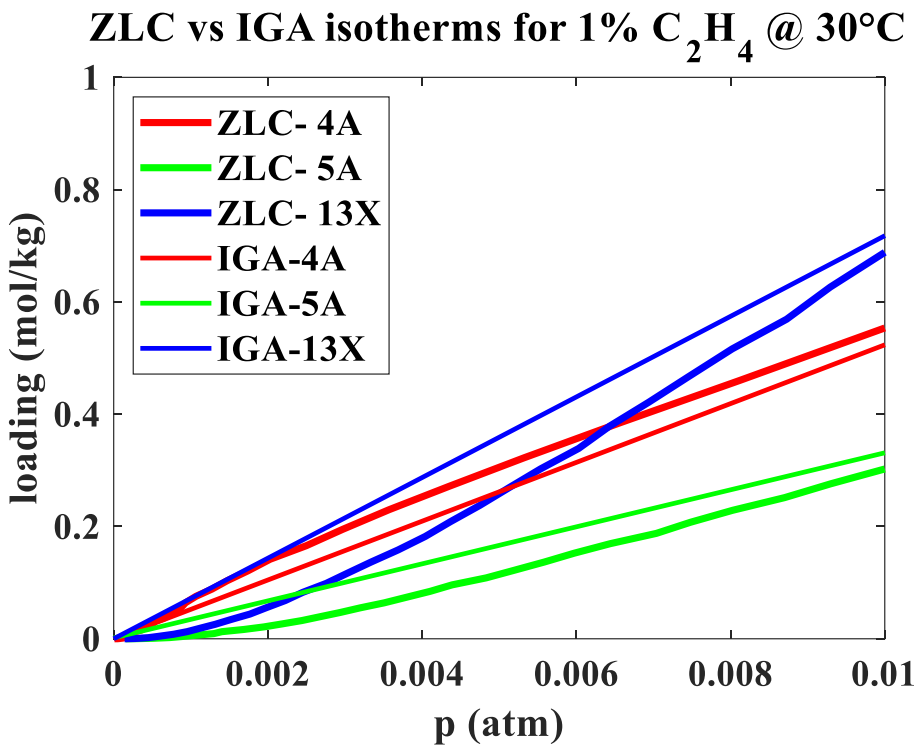

Figure 11.4S ZLC adsorption isotherms for 1% C_2H_4 at 30°C for zeolites 4A, 5A and 13X in comparison to IGA gravimetric results

Curriculum Vitae

Candidate's full name: Masoud Haeri Nejad

Universities attended:

MSc in Chemical Engineering KTH, Stockholm, Sweden, June 2012

PhD in Chemical Engineering UNB, Fredericton, Canada, May 2025

Publications:

1. Masoud Haeri Nejad, Rolando Mendieta, Apolinar Picado, " Determination of suitable thin-layer drying models for brewer's yeast (Saccharomyces cerevisiae)" *Nexo*, December 2015, pp. 58-66
2. Masoud Haeri-Nejad, Mladen Eić "Use of molecular simulation for evaluating adsorption equilibrium of inhalation anaesthetic agents on metal – organic frameworks," *Can. J. Chem. Eng.*, 2024;102: 1646-1657
3. Masoud Haeri-Nejad, Mladen Eić "Use of molecular simulation to design modification of a chromium-based MOF for adsorptive removal of inhalation anesthetic agents", *Can. J. Chem. Eng.*, 2024; DOI: 10.1002/cjce.25454

Conference Oral Presentations:

1. Masoud Haeri Nejad, Jiri Škvára**,** William Smith, Mladen Eić " Prediction of Vapor-Liquid Equilibria of Inhalation Anesthetics using Molecular Simulation" CCEC 2020 Toronto, ON, Canada
2. Masoud Haeri Nejad, Mladen Eić "Developing as fast screening technique to find the optimum adsorbent " CCEC 2021 Montreal, QC, Canada

3. Masoud Haeri Nejad, Jiri Škvára**,** William Smith, Mladen Eić " On-the Fly Molecular Simulation Approximation to the Second Virial Coefficient and Application to Low-Pressure Vapor-Liquid Equilibrium Simulation " CCEC 2021, Montreal, QC, Canada
4. Masoud Haeri Nejad, Jiri Škvára**,** Meghna Munipalle, Leann Tran, Javad Noroozi, Mladen Eić, William Smith, "A New Molecular-Based Vapor-Liquid Algorithm and Its Applications" CCEC 2022, Vancouver, BC, Canada

Conference Poster Presentations:

1. Masoud Haeri Nejad, Mladen Eić "Developing a fast-screening technique to find the optimum adsorbent " CCEC 2022, Vancouver, BC, Canada

Distinctions:

1. CJCE Editor-In-Chief's choice as featured article in the April 2024 Issue Highlights of Masoud Haeri-Nejad, Mladen Eić "Use of molecular simulation for evaluating adsorption equilibrium of inhalation anaesthetic agents on metal – organic frameworks," *Can. J. Chem. Eng.*, October 2023, pp. 1–12
2. Arvind Varma Chemical Engineering Graduate Student Prize for 2024